Dipl.-Phys. Martin Bothe

Shape Memory and Actuation Behavior of Semicrystalline Polymer Networks

BAM-Dissertationsreihe • Band 121
Berlin 2014

Die vorliegende Arbeit entstand an der BAM Bundesanstalt für Materialforschung und -prüfung.

Impressum

**Shape Memory and Actuation Behavior
of Semicrystalline Polymer Networks**

2014

Herausgeber:
BAM Bundesanstalt für Materialforschung und -prüfung
Unter den Eichen 87
12205 Berlin
Telefon: +49 30 8104-0
Telefax: +49 30 8112029
E-Mail: info@bam.de
Internet: www.bam.de

Layout: BAM-Referat Z.8

ISSN 1613-4249
ISBN 978-3-9816668-1-6

Shape Memory and Actuation Behavior of Semicrystalline Polymer Networks

vorgelegt von
Dipl.-Phys.
Martin Bothe
aus Tübingen

von der Fakultät II – Mathematik und Naturwissenschaften
der Technischen Universität Berlin
zur Erlangung des akademischen Grades

Doktor der Naturwissenschaften
– Dr. rer. nat. –

genehmigte Dissertation

Promotionsausschuss:

Vorsitzender:	Prof. Dr.-Ing. Matthias Bickermann
Gutachter:	Prof. Dr. rer. nat. Michael Gradzielski
Gutachter:	Prof. Dr. rer. nat. Michael Maskos

Tag der wissenschaftlichen Aussprache: 16.07.2014

Berlin 2014
D 83

Für meine Familie

Abstract

Shape memory polymers (SMPs) can change their shape on application of a suitable stimulus. To enable such behavior, a ‘programming’ procedure fixes a deformation, yielding a stable temporary shape. In thermoresponsive SMPs, subsequent heating triggers entropy-elastic recovery of the initial shape. An additional shape change on cooling, *i.e.* thermoreversible two-way actuation, can be stimulated by a crystallization phenomenon.

In this thesis, cyclic thermomechanical measurements systematically determined (1) the shape memory and (2) the actuation behavior under constant load as well as under stress-free conditions. Chemically cross-linked, star-shaped polyhedral oligomeric silsesquioxane polyurethane (SPOSS-PU) hybrid polymer networks and physically cross-linked poly(ester urethane) (PEU) block copolymers were investigated around the melting and crystallization temperatures of their polyester soft segments.

(1) The SPOSS-PUs showed excellent shape fixities and recoverabilities of almost 100% at high cross-linking density, while PEUs exhibited pronounced shape memory properties at increased soft segment content. Furthermore, two-fold programmed SPOSS-PU specimens were able to recover their initial shape in two thermally separated events. Even a neck, which formed during deformation of SPOSS-PUs with high soft segment content, was reversed.

(2) In PEUs, globally oriented crystallization on cooling drove expansion of the sample, in particular at high soft segment content and after application of a strong deformation. Melting reversed that orientation; the PEU sample contracted and thereby completed the thermoreversible actuation cycle. Under load, multiple polymorphic phase transitions enabled two successive expansion and contraction steps, while under stress-free conditions various geometric shape changes, including the increase and decrease of PEU sample length and thickness as well as twisting and untwisting could be experimentally witnessed. Such actuation technology allows for entirely new applications, enabling mimicry of reversible, bidirectional and repeated organic movements.

Zusammenfassung

Formgedächtnispolymere (FGPe) können unter Einwirkung eines geeigneten Stimulus ihre Form verändern. Um dieses Verhalten zu ermöglichen, wird eine Deformation mittels 'Programmierungs'-Verfahren fixiert, wobei das FGP eine stabile, temporäre Form einnimmt. In thermoresponsiven FGPen löst anschließendes Erwärmen entropieelastische Rückstellung in die ursprüngliche Form aus. Um thermoreversible Zweiwege-Aktuation zu realisieren, kann eine zusätzliche Formänderung beim Abkühlen durch ein Kristallisationsphänomen hervorgerufen werden.

Mittels zyklischer thermomechanischer Messungen wurden (1) die Formgedächtniseigenschaften (FGEen) und (2) das thermoreversible Aktuationsverhalten sowohl unter konstanter Auflast als auch unter spannungsfreien Bedingungen quantifiziert. Sternförmige Hybridpolymernetzwerke, chemisch quervernetzt durch polyedrisches oligomeres Silsesquioxan und Polyurethan (SPOSS-PU) und physikalisch quervernetzte Poly(ester urethan)-Blockcopolymere (PEUe) wurden im Bereich der Schmelz- und Kristallisationstemperaturen ihrer Polyesterweichsegmente untersucht.

(1) Insbesondere die SPOSS-PUs mit hoher Quervernetzungsdichte zeigten Formfixier- und Formrückstellbarkeiten von nahezu 100%, während PEUs ausgeprägte FGEen bei hohem Weichsegmentanteil aufwiesen. In zweifach programmierten SPOSS-PUs ließen sich darüber hinaus zwei thermisch separierte Rückstellungen induzieren. Selbst eine Einschnürung, die sich während der Verformung von SPOSS-PUs mit hohem Weichsegmentanteil gebildet hatte, war reversibel.

(2) Global orientierte Kristallisation führte bei Abkühlung zur Expansion der PEU-Proben, vor allem bei hohem Weichsegmentanteil und nach dem Aufbringen einer starken Deformation. Schmelzen revidierte die Orientierung; die PEU-Probe kontrahierte und komplettierte damit den thermoreversiblen Aktuationszyklus. Unter Auflast konnten multiple Phasenübergänge im polymorphen Weichsegment zwei aufeinander folgende Expansions- und Kontraktionsschritte auslösen, während spannungsfrei verschiedene Formänderungen, z.B. die Zu- und Abnahme von Probenlänge und -dicke sowie Ver- und Entdrehen einer Probe experimentell belegt werden konnten. Die vorgestellte Aktuatortechnologie ermöglicht völlig neue Anwendungen, die bidirektionale, organische Bewegungen nachahmen und wiederholen können.

Acknowledgements

First of all, I would like to thank my supervisor, Dr. Thorsten Pretsch, for the interesting topic, his never-ending help and invaluable feedback, with which he continuously supported my ideas. This work would not have been possible without his dedication and guidance over the past four years. I am also grateful to him for arranging the possibility to spend three months at the *Institute of Materials Research and Engineering* (IMRE) in Singapore.

I would like to express my deep gratitude to Prof. Dr. Michael Gradzielski, my supervisor at the Technical University Berlin, and Prof. Dr. Michael Maskos, my external supervisor (Johannes-Gutenberg University Mainz), who took – without hesitating – the academic responsibility for this thesis. The generous support I experienced in general and regarding my stay at the IMRE in particular allowed for some great experiences, for which I want to thank Prof. Dr. Michael Maskos.

I would also like to thank Dr. Wolfgang Stark, Dr. Matthias Jaunich and Petra Fengler for the DMA expertise, discussions about the viscoelastic properties of polymers, in particular crystallization behavior and entropy elasticity. Furthermore, I wish to thank Markus Schildhauer, Melanie Ecker and Nikolaus Fritzsche for the lively chats on SMPs in general, visions and ideas as well as research outcome and – as simple as that – their company. I want to acknowledge Dietmar Neubert, who provided me with lots of helpful DSC and TMA measurements and Carsten Vogt for the swelling experiments.

Next, I want to thank Dr. Franziska Emmerling for SAXS and WAXS, coffee, the friendly encouragement, and her support in analysing the WAXS diffractograms and Dr. Ralf Bienert and Simone Rolf for the great and meaningful *in situ* WAXS measurements at BESSY, conducted in the middle of the night. I also want to thank Andreas Wöhlecke for the help provided with tensile tests, talk on thermoplastics, polyurethanes and polymer research in general.

I wish to acknowledge the help provided by Maria Jürgens and Sophie Bigaillon, their endurance to conduct and monitor many, sometimes lengthy CTMs. Bernd Krafft is acknowledged for punching an endless series of specimens from various materials.

A big thanks goes to Dr. Khine Yi May and her Team at the IMRE in Singapore: for the great time, her guidance regarding synthesis and the patience in explaining chemistry to a physicist. For the actual support in the chemistry laboratories, the continuous SPOSS-PU supply and the NMR measurements I want to particularly thank Chee Chuan Yeo and Esther Marie Jie Lin.

Finally, Bayer MaterialScience is acknowledged for providing the valuable supply with PEU.

I would also like to thank my family and friends: my parents Werner and Regis for the extended support, their wisdom and advice in any situation. I want to thank Peter for the right tip just in time. Thanks go to all of my friends who supported and encouraged me, in particular Philipp, Caro, and Johannes.

Last but not least, I would like to thank my daughter Marlene for her smile, the effective distractions, when further work on the manuscript was pointless anyway, and the lively environment as well as my wife Silke for her love, silent patience, support, and continuous encouragement.

Contents

1. Motivation

Shape memory materials (SMMs) – including alloys,[1–4] ceramics[5,6] and polymers[7–10] – belong to the class of *smart materials*, which are able to respond to an external stimulus by a controlled, macroscopically observable reaction. With "intrinsic sensing, actuating, controlling or information-processing capabilities in their microstructure",[11] smart materials have the potential to strongly influence future products and designs, their inherent capability and the way they interact with their environment. Consequently, materials should no longer be perceived as static, structural parts of a device, but may become dynamic, active components.

Actuators from SMMs can mimic organic shape changes,[12] such as plant[13] and animal movement.[14] Accordingly, shape memory technology may help to achieve better performance and efficiency in fields like robotics or transportation and realize entirely new applications. For instance, the biomedical sector, which is always in search for sophisticated materials, demands for the development of SMMs with tailor-made thermomechanical properties to further develop devices and implants for minimally invasive procedures in surgery and operation.[15–18]

Shape memory polymers (SMPs) belong to the class of SMMs and can be biocompatible, biodegradable and nontoxic. Scalable synthesis, corresponding low costs, processability and workability allow for good availability of SMP devices; SMPs can be lightweight, dyeable and corrosion resistive. Most strikingly, SMPs exhibit extensive shape changes and recover from elongations of up to ten times their original shape.[19] In addition, SMPs have been successfully tested in tensile, compressive as well as torsional mode[20] and should hence be able to conduct almost arbitrarily complex shape changes. Basically, SMPs consist in cross-linked, long-chain molecules forming highly elastic, thermoresponsive networks. Variation of temperature around suitable phase transitions of the SMPs thermoresponsive segments gives control over their mechanical properties, including their elasticity and stiffness.

An important family of SMPs are physically cross-linked, phase-segregated polyurethanes (PUs),[10] which are promising due to their flexible molecular design and network structure.[21] By systematic modification of the PU composition, the thermal and mechanical properties can be adjusted to meet the requirements of a broad variety of applications, *e.g.* the shape recovery temperature can be set within an interval of -30 and 70 °C.[22] So far, physically cross-linked shape memory polyurethanes (SMPUs) have been studied with emphasis on their one-way dual-,[22–26] triple-shape memory[27,28] and actuation behavior.[29]

However, limitations of phase-segregated SMPUs are their moisture sensitivity, lower thermal stability and – most important – decreased mechanical resistance compared to elastomers.[30] In particular, high rubber resilience and low irreversible deformation are key factors for pronounced shape recoverabilities. To enhance these mechanical properties, polyhedral oligomeric silsesquioxane (POSS) can be incorporated into PUs.[30–32] In a common approach, POSS-diol is introduced into telechelic polymer chains.[33] The resulting SMPUs show shape memory properties, but require broad temperature intervals and high recovery temperatures to achieve almost complete shape recoveries.[33,34] Well-defined nanostructured polymer networks supply unique thermal and mechanical properties and outperform those of their linear counterparts.[35] The grafting of up to eight identical polymer arms from polylactides (PLAs) and aliphatic diisocyanates around the cubic geometry of POSS enables excellent shape memory properties, when shape fixing and recovery are conducted around the PLA glass transition temperature.[36]

In the scope of this thesis, similarly structured organic-inorganic polymer networks with a poly(ε-caprolactone) (PCL) soft segment were designed. PCL is considered a promising material due to its thermoplastic behavior, high elasticity and melting temperatures ranging from 45 to 67 °C.[37] PU networks were synthesized by the core-first method around the rigid inorganic POSS, with PCL chains of various lengths attached to each of its eight corners. Synthesis was finalized by cross-linking these macromolecules using hexamethylene diisocyanate (HDMI) to form three-dimensional SPOSS-PU networks. Phase transitions of the PCL soft segment suitable for shape memory behavior were identified in differential scanning calorimetry (DSC) and dynamic mechanical analysis (DMA).

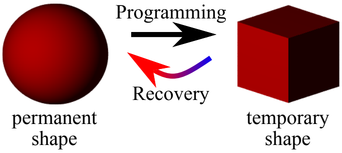

Scheme 1.1: The one-way shape memory effect.

As a model system for chemically cross-linked polymer networks, the shape memory properties of these SPOSS-PU networks were investigated in cyclic thermomechanical measurements (CTMs). Dual-shape measurements quantified the ability of the SPOSS-PUs to fix a tensile deformation strain of 100% by cooling below the PCL crystallization transition (temporary shape) and recover its initial shape on subsequent heating (permanent shape, Scheme 1.1). In addition, the stress response after deformation and shape fixing was studied with the specimens' length kept constant. Focus was put on the influence of the PCL chain length on the shape fixity, strain (shape) and stress recoverability and onset recovery temperatures.

To extend the thermomechanical repertoire of SPOSS-PUs, the capability to conduct two thermally separated shape changes on heating – triple-shape memory properties – was examined. Therefore, the above described CTM was modified. An additional deformation to a strain of 200% was fixed by cooling below the PCL glass transition temperature. Subsequently, the specimens' thermoresponsiveness to stepwise heating above the PCL glass and melting transition temperatures was investigated for the various SPOSS-PU compositions.

As a model system for physically cross-linked SMPs, a commercially available poly(ester urethane) (PEU) block copolymer (Desmopan® DP 2795A SMP) and a series of similar PEUs from the Bayer MaterialScience AG were selected. PU hard segment domains cross-linked the PEU networks, while a poly(1,4-butylene adipate) (PBA) soft segment was employed as either rubbery or stiff, semicrystalline soft segment. Various compositions of different hard to soft segment contents were characterized using DSC, DMA, wide-angle X-ray scattering (WAXS) and tensile tests.

The shape memory behavior of the series of physically cross-linked, thermoplastic PEUs was characterized around the PBA soft segment crystallization and melting temperatures. Comparison of the shape memory parameters with those of the SPOSS-PUs allowed deducing – to some extent – the influences of the polymer network structure. To investigate the effect of two various polymorphic crystal phases on the shape memory behavior, the crystallization and storage conditions during and after shape fixing were modified for an exemplarily chosen PEU (of high PBA content) and the shape memory behavior was monitored.

As a second objective of this thesis, the PEUs were investigated for their thermoreversible actuation behavior (also known as the two-way shape memory effect, 2W-SME, Scheme 1.2). This effect has been observed for a number of semicrystalline SMPs.[8,29,33,38–40] Accordingly, the

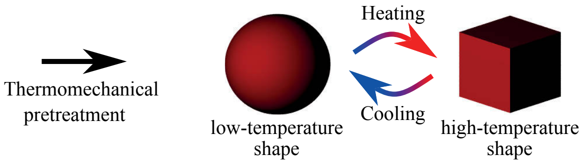

Scheme 1.2: The two-way shape memory effect.

specimen shows opposing shape changes on cooling and heating under isotonic (constant external load)[41] conditions, *i.e.* expansion and contraction under tensile load. While melting-induced contraction (MIC) results from entropy elasticity, which is a well-understood thermodynamic effect,[42] crystallization-induced elongation (CIE) on cooling is a comparably newly discovered phenomenon and of vital interest for the realization of pronounced actuation behavior in semicrystalline SMPs.[38] Although it has been widely accepted that CIE is driven by crystallization and that the associated microstructural orientation is an important criterion for macroscopic shape changes, an explicit investigation and quantification of the orientation during actuation has not yet been conducted. Moreover, research on SMP actuation still lacks knowledge of the influence of complex crystallization processes on the observed actuation behavior, *i.e.* the effect of polymorphic crystallization on the expansion process has not been regarded so far. Finally, CIE has only been observed in the presence of a constant load, which strongly restricts its applicability and the realizable geometry of shape changes. In recently reported approaches, free-standing actuation was achieved by incorporating the isotonic conditions into an actuator device of composite structures, consisting in an SMP – capable of conducting two-way shape changes under constant load – and a flexible component, such as an elastomer.[43–45] However, those approaches are constraint to relatively simple movements like bending and straightening due to their initially defined composite geometry.

To overcome the outlined limitations, the actuation behavior of the PEU series was investigated in various specifically arranged CTM procedures. Isotonic conditions were applied to the PEU series in a thermomechanical pretreatment, which mainly consisted in a deformation at a temperature above the PBA melting transition. The accordingly pretreated specimens – kept under constant stress – were exposed to cooling-heating cycles. PBA crystallization and melting triggered CIE and MIC.

To gain a more profound understanding of CIE and MIC, the effect of various initial deformations and accordingly selected isotonic conditions on the actuation behavior of a single PEU was investigated. In addition, PEU specimens were withdrawn from CTMs during thermal cycling after CIE and studied by WAXS and DSC to obtain a clear picture of the crystallization processes during actuation.

Fully stress-free, bidirectional shape changes of PEU on cooling and heating were approached by modification of the above described thermomechanical pretreatment to obtain a ‘training’ procedure, basically consisting in an extensive deformation and complete stress release at a temperature above the PBA melting transition. In subsequent thermal cycles inducing PBA crystallization and melting, the PEU specimens were tested for their actuation behavior. *In situ* WAXS measurements monitored the microstructural evolution during cooling-heating cycles and thereby gave the opportunity to conduct an in-depth investigation of CIE.

2. Introduction

The following chapter gives a broad overview of the historic development of rubbers and SMMs, SMPs, polymer network architectures, the thermal and mechanical properties of polymer networks, their characterization and state-of-the-art shape memory technology; current and potential applications are listed. Finally, a strategy to approach remaining challenges is given.

2.1. History of Shape Memory Research

In 1805, John Gough[46] reported on his extraordinary findings regarding the thermomechanical properties of indian rubber (*caoutchouc* from an indigenous language of Amazonian Peru or Equador). Firstly, he noted that as opposed to common materials a rubber band released heat when quickly stretched. Secondly, the rubber band had a negative thermal expansion coefficient when kept under load, thus reversibly contracted on heating and expanded on cooling. After the invention of vulcanized rubber[a] by Charles Goodyear,[48] which offered considerably enhanced mechanical properties over natural rubber, James Joule[49] was able to reproduce and quantify Gough's discovery. The phenomenon termed Gouth-Joule effect is connected to the long-chain network structure of rubbers and emphasizes its thermoelastic nature, which is a key to the understanding of rubbery behavior.

Investigations on the fundamental statistical, thermal and thermoelastic properties of polymeric materials proceeded, including the thermodynamic description of elasticity in rubber,[50,51] correlation of the microscopic and macroscopic states in deformed rubbers,[50] the relationship between swelling capacity and elastic properties of polymer networks[52,53] and the experimental verification of the theory of rubber elasticity.[41,54]

In parallel, a patent by Vernon and Vernon[55] granted in 1941 is often mentioned as the first description of the shape memory effect ('elastic memory') in a thermoplastic synthetic resin.[56] About 10 years later, Paul Cook at Raychem® developed an even nowadays widely used application of shape memory in radiation cross-linked polyethylene - heat-shrinkable tubings for electrical insulation.[57] Most prominently, the parallel development and application of shape memory alloys

---

[a] radiocarbon dating indicates, that the ancient Mesoamerican population already used latex rubbers cross-linked by organic compounds 1600 b. c.[47]

(SMAs) was perceived. Firstly, Chang and Read[1] described thermoelastic properties of gold-cadmium alloys in 1951. At that time unknown, closely related changes in acoustic damping, surface structure and indentation recovery on heating in the temperature range of 100 to 200 °C[58] in equiatomic nickel-titanium (Nitinol) alloys were discovered by Buehler *et al.*,[2] followed by greatly enhanced interest toward actual shape memory functionality. The term *shape-memory effect* was originally coined by de Lange and Zijderveld,[3] who gave a detailed description of the connection between superelasticity and the corresponding martensitic-austenitic phase-transition in Nitinol alloys, which can be described similarly to rubber elasticity in polymers.[59]

As discovered in the 1970s, even glass-ceramics containing mica as the principal crystalline phase were able to exhibit the shape memory effect; deformations of about 0.5% could be recovered[5] due to phase transitions similar to those in SMAs.

2.2. Polymer Network Architectures

Fundamentally, polymers are chemical compounds build up from a repeated structural subunit – the monomer. As such, a polymer consists of long-chain molecules, which can be cross-linked in various ways to form a solid body. The network architecture of cross-linked polymer chains determines the thermal and mechanical properties[60] and can yield highly elastic, yet thermoresponsive networks. Along with the incorporated monomeric species, structural factors influencing the polymer network behavior include

- the length of the network chains between two neighboring cross-links,[22,40,61]
- the cross-link density,[42]
- the number of chains attached to a single netpoint[62,63] and
- the nature of cross-links.[56]

For example, adaptation of the mean polymer chain length effects the phase transition temperatures, degree of crystallinity and thereby the polymer stiffness. Additionally, incorporation of (nano)materials can strongly alter diverse polymeric properties, among them their electric conductivity and magnetic permeability,[64] adaptation of the thermal conductivity[65] and mechanical reinforcement.[66]

The last point of the itemization gives a broad distinction of network structures. Basically, polymer chains are either chemically or physically cross-linked, forming on the one hand thermosets or elastomers (which structurally differ by the degree of cross-linking) and on the other hand thermoplastic polymers. These ways of cross-linking have implications on the thermomechanical properties, *i.e.* chemical cross-links supply higher strength at increased temperature.[67]

In addition, the network structures are handled differently during fabrication, processing and recycling and are employed in different fields of application. In the following, the polymer network architectures of relevance for this theses are presented.

Chemical cross-linking – the introduction of covalent bonds – is the traditional way to obtain elastomeric polymer networks from gummy materials (Scheme 2.1).[42,68] The classical example of a cured elastomer is natural rubber, which is a linear polymer of isoprene $(\mathrm{CH_2\,C\,(CH_3)\,CH\,CH_2})$ units. Addition of sulphur or other reagents to the raw *caoutchouc* and the process of vulcanization, usually conducted by heating or compression of the material, initiates the formation of disulfide covalent bonds (R—S—S—R') at the isoprene's methyl $(\mathrm{—CH_3})$ side groups. From a structural point of view, the covalent bonds irreversibly cross-links the rubber in its permanent shape. Once chemically cross-linked, the polymer cannot be brought into a new permanent shape and is accordingly not recyclable.

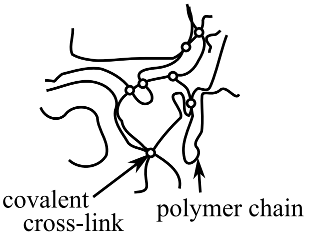

Scheme 2.1: Elastomer with covalently cross-linked chains.

However, vulcanized rubbers are known for their extensive deformability and rubber resilience,[42] and supply pronounced shape memory properties.[19] Chemically cross-linked SMPs include polyurethanes prepared from star-shaped hydroxy-telechelic cooligoesters,[69] PCL cross-linked by dicumyl peroxide (DCP),[63] poly(vinyl alcohol) cross-linked with different contents of glutaraldehyde[70] and polycyclooctene cross-linked by DCP.[71]

Other than chemically cross-linked elastomers, thermoplastic polymers are characterized by thermoreversible, physical cross-links. These result either from crystalline or glassy domains,[72,73] Hydrogen bonding,[67,74] chain entanglements[75] or phase separation of linearly aligned polymer chains.[73] Above their associated phase transition temperature, the thermoplastics can be molded or remolded into their permanent shape.[76] Below that transition, physical cross-links form and supply the polymer network with stable mechanical properties, *i.e.* the thermoplastics can be stiff, ductile or rubbery. Rubbery thermoplastics are known as thermoplastic elastomers (TPEs), which combine the properties of thermoplastic and elastomeric polymers. The advantages of thermoplastic elastomers are mainly their ease of processibility, reusablity and fast production.[77]

An important class of TPEs are phase-segregated block copolymers such as PEUs.[72,73,78] Block copolymers possess two or more alternating segments. When these are thermodynamically incompatible, phase separation results in the formation of two or more domains below a so-called order-disorder transition (Scheme 2.2).[26,79] For example, PEUs with alternating polyurethane hard segments and a polyester soft segment supply a microstructure of spatially separated domains.[73,80] The rigid PU hard segment domains reinforce the PEU matrix and act as physical cross-links. The polyester soft segment domains comprise a semicrystalline or rubbery matrix and supply the thermoresponsiveness.

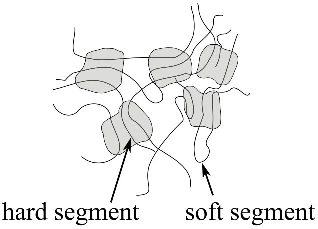

Scheme 2.2: Block copolymer with hard and soft segment domains.

Shape memory testing of PEUs is consistently conducted at temperatures considerably below the melting transition of the PU hard segment ($T_{m,PU}\sim$ 190 °C).[73] The polyester phase transitions are employed for shape memory testing. Examples of physically cross-linked SMPs include PUs with soft segments from PCL,[22] poly(tetramethylene glycol),[81] trans-polyisoprene[82] and PBA[27,83] soft segments. The latter block copolymer, the commercially available Desmopan® DP 2795A SMP and a series of related PEUs is investigated in this thesis.

Nanostructured organic-inorganic hybrid polymers can be obtained from building block synthesis, allowing for highly reproducible, well-defined elastomers.[35,84] These may be of completely different properties than a bulk material of the same composition[85] and are said to outperform the properties of their linear counterparts.[35] The herein investigated hybrid polymer networks consist of a polymeric matrix material and an incorporated nanocomponent.

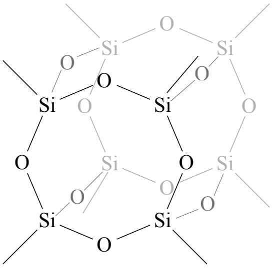

Scheme 2.3: POSS cage with eight vertices.

A particularly interesting nanomaterial is polyhedral oligomeric silsesquioxane (POSS), which is an organic / inorganic hybrid material build up from silicon and oxygen atoms, precisely defined by its general composition $(SiO_{1.5})_8$ (Scheme 2.3). Geometrically, POSS forms an eight-cornered cage of about 0.45 nm in diameter,[86] with each corner supplying a reactive site to attach a polymer chain.

Current literature describes nanohybrid composites with elastomeric properties incorporating POSS in combination with various polymer matrix materials. Hybrid polymers from POSS and polyethylene have been observed to exhibit enhanced mechanical and chemical properties, including dimensional stability, surface hardening, increased strength[87] and oxidative resistance.[88] In polyurethane elastomers, crystalline regions of POSS particles within the hard segments acted as a nanoscale reinforcement.[89] Similarly, the incorporation of POSS[89] and silica[90] into polymeric matrices from polyurethanes with soft segments from polytetramethylene glycol strongly enhanced strength and tensile modulus.

Shape memory properties have been observed in hybrid nanocomposites incorporating silica[90] as well as in SMPUs incorporating POSS: SMPUs from biodegradable poly(lactide-*co*-glycolide)[34] or poly($_{\text{D,L}}$-lactide)[91] with POSS diol provided excellent elasticity at temperatures above the glass transition temperature of a lactide-based soft block and pronounced shape memory properties. Moreover, hybrid polymers from POSS and PCL[33] featured a ‘double network’ from superposition of a covalent with a percolative physical network, the latter resulting from a crystalline POSS phase. These POSS-PCL polymers showed shape memory as well as actuation behavior, the latter under isotonic conditions.

2.3. Properties of Polymer Networks

Phase transitions and the generic property of entropy (rubber) elasticity supply the fundamental mechanisms for shape fixing, deformation and shape recovery. These properties are found in most (if not all) polymers. Hence, the capability to exhibit the shape memory effect should thus be an intrinsic phenomenon.[92] Here, a brief introduction to the thermal and mechanical properties relevant for the realization of shape memory and actuation behavior is given.

2.3.1. Polymer states of matter

The term ‘transition’ refers to a change in state of matter of the polymer or one of its constituents. Phase transitions can be either induced by changes in temperature or pressure, in cross-linked polymers also by deformation in tension or shear.[68,93] The two most relevant phase transitions of semicrystalline polymers are drafted here. Melting is characterized by structural changes. It is defined as the transition from crystalline to amorphous state. As a first order transition (eminent by a discontinuity of the polymer’s specific volume over temperature) it correlates to the solid-liquid transition in low-molecular substances.[94] In contrast, the glass transition is a second-order transition in amorphous polymers.[95] Here, the volume-temperature dependence is continuous, but not its temperature-derivative. Most importantly, the glass transition is not connected to structural changes.[42] In any case, the glass transition temperature is lower than the melting temperature of a polymer. Consequently, a polymer may incorporate spatially separated domains having three different states:

- Below the glass transition temperature, or more definite, glass-liquid or glass-rubber transition, amorphous domains are hard and brittle. A fully amorphous, glassy polymer forms an organic glass. The glassy state is a non-classical state of matter, characterized by the absence of collective, long-range molecular motions. Accordingly, the spatial arrangement (conformation) of a polymer chain is frozen.

- Semicrystalline domains exist below the melting transition temperature. These are characterized by polymer chain alignment, with the polymer chains adapting a regular, anisotropic conformation. However, long polymer chains make crystallization imperfect, such that polymers crystallize incompletely. Thus, the resulting semicrystalline bulk polymers contain crystalline and amorphous domains. Many polymers, including aliphatic polyesters,[96] crystallize in various structural modifications.[93] These crystalline polymorphs may either differ in chain conformation or packing mode and are predetermined by the present crystallization conditions. On a mesoscopic scale, more complex structures evolve, among them granular crystallites and lamellae,[97] spherulites,[98] and row-nucleated structures (‘Shish-kebab’ structures).[99]
- Rubbery, amorphous domains above the glass transition temperature give elastomers their unique rubbery or elastomeric properties. In this state, the amorphous polymer chains are highly mobile. The atoms within the polymer chain continuously rotate around the axis formed by the next two neighboring atoms. Thereby, the polymer chain can adapt a virtually unlimited number of conformations. Such conformational freedom permits viscous flow as well as elastic behavior, while the cross-links define and maintain the permanent shape.

2.3.2. Mechanical properties

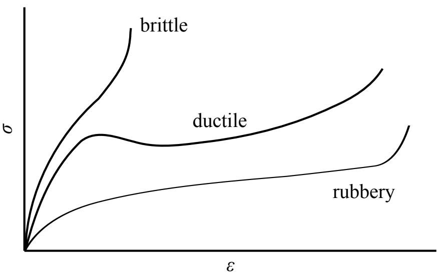

Scheme 2.4: Characteristic tensile stress σ *vs.* strain ε diagram for a polymer under various conditions.

The way a polymer responds to an applied deformation is characterized by internal (such as the network structure described above) and external factors, including the deformation rate, temperature and time-scale of the deformation.[100]

Characteristic responses to deformation are given in the stress-strain(σ-ε)-diagram in Scheme 2.4. Owing to the low molecular mobility of the polymer chains, the glassy polymer is stiff and brittle, hence breaks at small elongations. Semicrystalline polymers contain crystalline and amorphous, either glassy or rubbery domains. The crystalline domains act as physical cross-links, reinforcing the polymers stiffness, such that semicrystalline polymers often exhibit ductile stress-strain curves.[101] In a purely molten, rubbery polymer, high molecular mobility of the polymer chains permits the polymer to sustain extensive deformations. Final stress increase of the stress-strain curve indicates hardening of the polymeric specimen originating from deformation-induced crystallization.

In general, polymers combine the mechanical properties of fluids and solids, exhibiting viscoelastic behavior.[100] The viscoelastic response of a polymeric material to an applied load is composed of a time-independent contribution from elasticity and a time-dependent contribution from viscous flow. Microscopically, viscous processes can be understood as irreversible movement of chains slipping past each other. Macroscopically, viscosity either manifests as an increasing strain under persisting mechanical load conditions known as creep, or as the phenomenon of stress relaxation. Stress relaxation describes a time-dependent stress decrease under isometric (constant length) conditions, with the stress $\sigma(t)$ described by the exponential function

$$\sigma(t) = \sigma_0 \cdot \exp\left(-\frac{t}{\tau}\right), \tag{2.1}$$

where σ_0 is the initial stress after deformation, t the time and τ the specific relaxation time.[102]

In turn, the elastic materials response is achieved almost instantaneously. For polymer networks above the melting transition, it is described by entropy-elastic behavior. This contrasts the behavior of most materials, including glassy polymers, which are energy-elastic. In this case, deformation shifts the atoms in the interatomic potential of their neighboring atoms, resulting in a net increase of inner energy. In contrast, the highly mobile polymer chains inside of a cross-linked polymer network (above its glass transition temperature) adapt their conformation to follow the deformation direction. Thereby, the conformational entropy of the polymer chain is reduced.

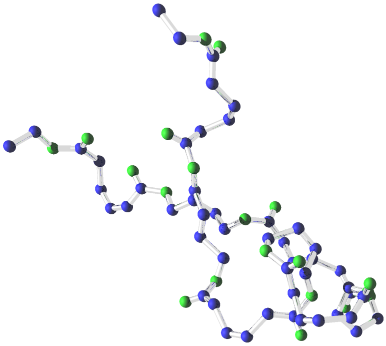

Scheme 2.5: Rendering of a random conformation of a PBA chain consisting in 5 monomers.

That way, deformation induces an ordering process, which is connected to a decreasing entropy of the entire polymer network. In equivalence to a compressed ideal gas expanding in volume and in line with the second law of thermodynamics, the polymer chains tend to recover their state of highest entropy. Consequently, the bulk polymer reverses the deformation and recovers its initial shape.[103]

Statistically, entropy elasticity is driven by deformation-induced changes of the polymer chain end-to-end distance.[42] In this process, the random-coiled chains (Scheme 2.5) are stretched and thereby transferred from their state of highest probability into an extended, less probable conformation. Under the assumption, that the statistical distribution of the end-to-end distances for polymer chains is described by a Gaussian profile, the stress due to entropy elasticity on deformation from an initial length L_0 to L ($\lambda = {}^{L}\!/_{L_0}$) can be described by[68]

$$\sigma = NRT(\lambda - \lambda^{-2}), \tag{2.2}$$

where N is the number of network chains per unit volume, R the gas constant and T the temperature. To sum up, entropy elasticity implies two major points:

- The strong deformation-induced conformational changes allow for high extensibility (orders of magnitudes greater than those found in most known materials), yet supplu the ability to recover the initial shape.
- The arising stress is a linear function of the temperature and increases at higher temperatures.[104]

In result, entropy elasticity enables SMPs to conduct shape changes with magnitudes exceeding those in SMAs or shape memory ceramics. By controlling the temperature, the ability of the SMP to entropy-elastically contract can be either promoted or inhibited. Accordingly, under a constant load, even simple variation of the temperature provides a basis for elastomeric actuation under constant load.

2.4. Characterization of Polymer Networks

Several classical techniques can be employed to investigate and characterize the polymer network structure, its morphology as well as the associated thermal and mechanical properties.[105] Phase transition temperatures can be determined by differential scanning calorimetry (DSC) and dynamic mechanical analysis (DMA). The cross-link density and in turn the molecular weight of polymer chains between two neighboring netpoints can be studied using swelling experiments. Mechanical tests provide an additional estimate of these parameters. At a smaller length scale, scattering methods like WAXS allow to investigate the crystalline structure. Most importantly, the shape memory properties are determined in cyclic thermomechanical measurements (CTMs).

2.4.1. Swelling experiments

When exposed to a solvent, polymer networks tend to swell. By the volumetric degree of swelling and knowledge of the polymer-solvent interaction, the effective polymer network structure can be determined. It is a measure of the cross-link density and inversely of the polymer chain length between neighboring cross-links.[105]

After swelling, the fraction of the mass of the swollen sample m_{sw} and dry sample m_d can be used to determine the gel content G according

$$G = \frac{m_d}{m_{sw}}. \tag{2.3}$$

In addition, the degree of swelling Q is calculated by means of

$$Q = 1 + \frac{\rho}{\rho_1}(\frac{m_{sw}}{m_d} - 1), \tag{2.4}$$

in which ρ is the specific density of the tested SMP and ρ_1 the solvent density. From the *Flory-Rhener theory*, which applies to polymers with three-dimensional network structures, the molecular weight M_W of swollen, cross-linked polymer chains and the cross-link density ν_c can be determined according to[53]

$$\nu_c = \frac{ln(1-\phi_2) + \phi_2 + \phi_2^2\chi_{12}}{V_1(\frac{\phi_2}{2} - \phi_2^{1/3})} = \frac{\rho}{M_w}. \tag{2.5}$$

Herein, ϕ_2 is the volume fraction of the polymer in the swollen system. It is defined by the ratio of dry volume (V_d) and swollen volume (V_{sw}). Beyond that, V_1 is the molar solvent volume. The constant χ_{12} is the Flory polymer-solvent interaction parameter.

2.4.2. Differential scanning calorimetry (DSC)

The heat flow and accordingly the amount of heat a sample absorbs or releases during cooling and heating is monitored in DSC. Therefore, the power required to heat the sample to a given temperature or inversely the change in sample temperature when heated by a given power is compared to a reference. From the monitored quantity, the heat flow is calculated. Signals in the heat flow can be ascribed to physical or chemical transitions.[106] The integrated heat flow of the respective signals represents the enthalpy of the considered transition.

DSC is particularly sensitive to crystallization and melting transitions. To fit complex melting processes, overlapping endotherms in DSC can be deconvolved by an exponentially modified

Gaussian (EMG) distribution as proposed by Elsabee and Prankerd.[107] Therefore, a least-squares fit of the superposition

$$\Phi(T) = E_1(T) + E_2(T) + c \tag{2.6}$$

with a constant offset c and the exponentially modified Gaussian distributions $E_y(T)$ as defined according

$$E_y(T) = \frac{A}{2\beta} \cdot \exp\left(\frac{\alpha^2}{2\beta^2} + \frac{T_m - T}{\beta}\right) \cdot \left[\operatorname{erf}\left(\frac{T_{max} - T}{\sqrt{2}\alpha} - \frac{\alpha}{\sqrt{2}\beta}\right) + \frac{\beta}{|\beta|}\right], \tag{2.7}$$

was conducted. Here, T is the temperature, A the area below the distribution, T_{max} the temperature of the peak maximum, α the peak width at the inversion point, β the peak distortion and erf the error function.

2.4.3. Mechanical characterization

DMA quantifies changes of the viscoelastic properties for a given temperature interval. A weak, periodic loading with a frequency ω is applied to the polymeric samples within the materials Hookean region.[106] In parallel, the temperature- and time-resolved mechanical response of the material is monitored.[108] The moduli resolve first and secondary order phase transitions and are particularly sensitive to the glass transition temperature. In greater detail, a periodic, *e.g.* sinusoidal, deformation

$$\varepsilon(t) = \varepsilon_0 \sin(\omega t) \tag{2.8}$$

is applied with the amplitude ε_0 and results in a periodic stress

$$\sigma(t) = \sigma_0 \sin(\omega t + \delta), \tag{2.9}$$

with the amplitude σ_0 shifted by a phase shift δ.

From these quantities, the storage modulus E' and the loss modulus E'' (in case of periodic tensile deformation) can be calculated according

$$E' = \frac{\sigma_0}{\varepsilon_0} \cos(\delta) \tag{2.10}$$

and

$$E'' = \frac{\sigma_0}{\varepsilon_0} \sin(\delta). \tag{2.11}$$

The complex elastic modulus E is obtained from its real part E' and its imaginary part E'' by

$$E = E' + iE'' \tag{2.12}$$

In the complex plane, the applied deformation strain precedes the resulting stress vector by the phase shift δ. The $\tan(\delta)$ is the loss factor.

$$\tan(\delta) = \frac{E''}{E'} \tag{2.13}$$

It represents the ratio of loss and storage modulus. The shear moduli G, G' and G'' can be determined accordingly. Conversion of tensile and shear moduli can be performed according

$$G = \frac{1}{2(1+\nu)} \cdot E. \tag{2.14}$$

For non-auxetics with a Poisson's ratio $0 < \nu \leq 0.5$, the shear modulus can be estimated to be

$$\frac{1}{3}E < G \leq \frac{1}{2}E. \tag{2.15}$$

Uniaxial tensile testing is a fundamental type of a mechanical test, which allows to observe the mechanical response of a specimen subjected to tension. From the stress-strain profile of a material, basic mechanical properties can be determined, including the ultimate tensile strength σ_B, yield strength σ_{yield}, toughness k and strain at break ε_B. In addition, the initial value of the stress-strain derivative represents the Young's modulus E. According to the Gaussian theory of rubber elasticity,[42] it is connected to the polymer network structure. The cross-link density ν_c in a polymer is a function of the Young's modulus E and can be determined according

$$\nu_c = \frac{E}{3RT} \tag{2.16}$$

with the universal gas constant $R = 8.314\,\mathrm{J\,mol^{-1}\,K^{-1}}$ and the absolute temperature T.

Small, thermally induced volumetric changes of solid state materials, such as thermal expansion in polymer networks can be precisely determined in dilatometric measurements.[106] Thereby, small actuation effects can be distinguished from simple thermal expansion.

2.4.4. Cyclic thermomechanical measurements (CTMs)

As Lendlein and Kelch have highlighted,[7] SMPs need thermomechanical processing to exhibit shape memory or actuation behavior. Such processing is conducted in CTMs. As a basic requirement, the employed apparatus has to be able to steer the temperature and mechanical deformations in strain- or stress-controlled mode. In a common approach, tensile testing machines equipped with a thermochamber are used.[109] Such systems allow to precisely define the settings of stress or strain and temperature in a sequence of testing segments, such that complex thermomechanical treatments are feasible. Alternatively, DMA devices may be used in tensile or bending mode.[64,110]

A full CTM procedure includes thermomechanical pretreatment of the specimen, such as shape programming or the application of a constant stress, and the subsequent investigation of the shape memory and actuation behavior.[111] Most importantly, the testing temperatures are systematically set to temperatures around a predetermined phase transition temperature T_{trans}, which can be either a crystallization / melting or a glass transition temperature. The response of the SMP to the individual testing segment is quantified by the dependent parameter, which is either the strain or the stress.

As an example of a convenient one-way shape memory procedure, a sequence of testing segments for one thermomechanical cycle of a dual-shape measurement with free strain recovery is shown in Scheme 2.6.

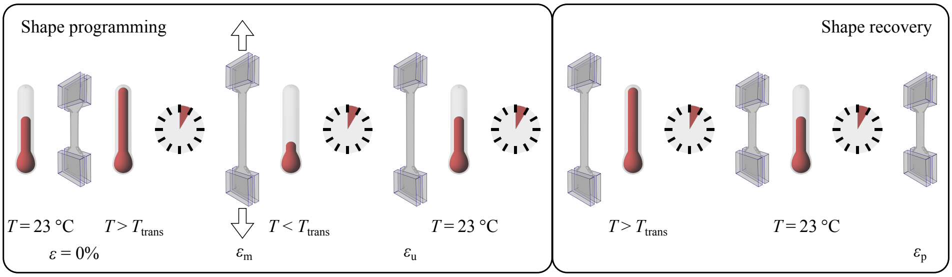

Scheme 2.6: One cycle of a dual-shape measurement as conducted in CTMs, including shape programming and free strain recovery. Details are given in the text.

The thermomechanical cycle consists in a shape programming and a shape recovery step. During shape programming, the SMP is heated from 23 °C to above the phase transition temperature T_{trans} and deformed to a strain ε_m. Adjacently, the deformation is fixed by cooling below T_{trans}. In result, the SMP maintains a stable, temporary shape after unloading ε_u.

Subsequent to shape programming, the polymer response to heating is quantified. Free strain recovery is initiated by heating the SMP above the temperature T_{trans}, with the clamps maintaining zero tensile force and the crosshead following specimen contraction. The recovered strain of the permanent shape ε_p is finally determined. Appropriate holding times ensure stable thermal conditions.

Characteristic strain-related shape memory quantities are calculated for each thermomechanical cycle N from the obtained stress-strain-temperature datasets, including the shape fixity ratio[112,113]

$$R_f(N) = \frac{\varepsilon_u(N)}{\varepsilon_m}, \tag{2.17}$$

the total shape (strain) recovery ratio

$$R_{r,tot}(N) = \frac{\varepsilon_m - \varepsilon_p(N)}{\varepsilon_m} \tag{2.18}$$

and the shape (strain) recovery ratio

$$R_r(N) = \frac{\varepsilon_m - \varepsilon_p(N)}{\varepsilon_m - \varepsilon_p(N-1)} \tag{2.19}$$

which reflect the polymer's ability to maintain a programmed temporary shape, to recover its initial, permanent shape and to conduct cyclically reproducible shape changes, respectively.

In addition, the specimen's response to heating can be determined under fixed strain conditions. Therefore, an identical programming procedure is applied. During fixed strain recovery, the strain of the programmed specimen is maintained at the constant strain ε_u and the maximum recovery stress $\sigma_{r,max}$ during heating above T_{trans} is measured. From the loading and recovery stresses, the stress recovery ratio $R_S(N)$ is calculated according

$$R_S(N) = \frac{\sigma_{r,max}(N)}{\sigma_l(N)}, \tag{2.20}$$

which is a measure of the specimen's ability to recover the initially applied loading stress σ_l.

Actuation measurements of semicrystalline SMPs are conducted under isotonic conditions. In a first step, a thermomechanical pretreatment applies the constant stress, as exemplarily depicted in Scheme 2.7. In detail, the pretreatment starts by specimen heating above T_{trans}, which in this case is the crystallization / melting transition temperature. Thereafter, an initial stress σ_i is applied, which is subsequently reduced to the constant stress σ_c. Adjacently, the loaded specimen is exposed to thermal cycling, consisting in heating above T_{trans} and cooling below T_{trans}. The stress σ_c is maintained and the change in strain is monitored throughout the CTM. As above, stable thermal conditions are ensured by introduced holding times.

A comprehensive description of widely applied shape memory testing procedures is given by Sauter *et al.*[111]

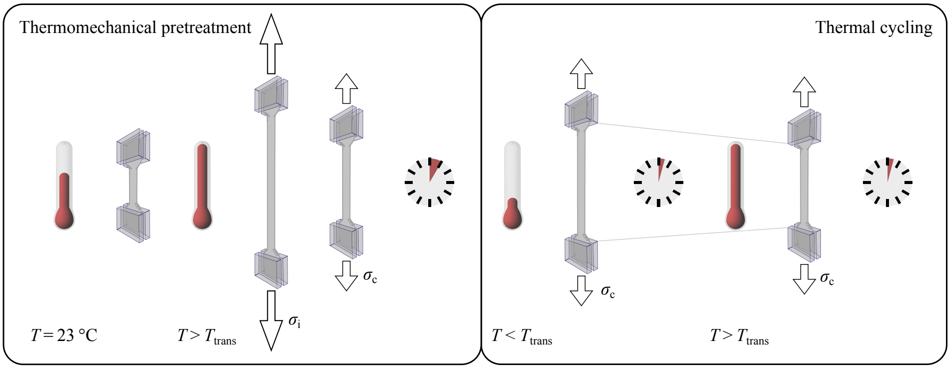

Scheme 2.7: Actuation measurement under isotonic conditions as conducted in CTMs, including thermomechanical pretreatment and one thermal cycle. Details are given in the text.

2.4.5. Wide-angle X-ray scattering (WAXS)

Diffraction describes the interaction of waves with physical obstacles. It occurs, where the wavelength and the investigated obstacles are of the same order of magnitude. Accordingly, X-rays with wavelength $\lambda = \sim 1\,\text{Å}$ interact with atomic structures, and hence can be used to determine the periodicity of these, allowing to resolve interatomic distances, *e.g.* in polymer crystallites. As a potential radiation source, X-rays tubes are commonly employed in the laboratory.[114] Synchrotron radiation is advantageous due to the tunability of the monochromatic X-ray wavelength. It has a much higher brilliance than X-ray tubes, *i.e.* increased photon density, which allows for shorter exposure times and / or increased signal-to-noise ratios.

As the basic principle, a beam of X-rays, transmitted through a polymer specimen, is diffracted by crystalline domains. The scattered beams interfere with each other. The condition for constructive interference of X-ray beams is given by Bragg's law

$$n\lambda = 2d\sin(\theta), \tag{2.21}$$

with the integer n determining the order given, λ the wavelength, the spacing d of two scattering planes in the crystalline lattice and the angle θ between the incident X-ray and the scattering planes.

As a result, bright spots and dark regions from constructive and destructive interference yield a characteristic diffraction pattern on an attached screen. The analysis of the Bragg peaks, their angles and intensities, gives information about the particular crystal structure, the orientation of the crystalline domains and the degree of crystallinity.

From the combination of the calculated spacings and the angular position of the corresponding reflexes on the diffraction pattern the crystalline system may be deduced. Alternatively, comparison with reference samples allows to ascribe the observed signals to the respective structures.

In addition, peak deconvolution of the scattered intensity facilitates the assignment of reflexes to crystalline and amorphous regions. The degree of crystallinity χ_c can be estimated by comparison of the integrated diffraction intensity from crystals I_{cryst} with the totally scattered intensity I_{total}.

$$\chi_c = \frac{I_{cryst}}{I_{total}} \tag{2.22}$$

Moreover, two-dimensional scattering patterns obtain information regarding the degree of global orientation of the crystalline domains. For a given diffraction pattern, the Herman's orientation function f_o can be calculated according to Ref.:[115]

$$f_o = \frac{1}{2}(3\langle \cos^2(\phi)\rangle - 1) \tag{2.23}$$

with the azimuthal angle ϕ and its expected value $\langle \cos^2(\phi)\rangle$ defined as

$$\langle \cos^2(\phi)\rangle = \frac{\int_0^{\pi/2} I(\phi)\cos^2(\phi)\sin(\phi)d\phi}{\int_0^{\pi/2} I(\phi)\sin(\phi)d\phi}. \tag{2.24}$$

The Herman's orientation function is dimensionless; it varies between 1 for a system completely oriented in direction $\phi = 0$, is 0 for an isotropic distribution of the scattering objects and -0.5 for the objects aligned in direction $\phi = 90°$.

2.5. Shape Memory and Actuation Behavior of Polymer Networks

With an elastic, thermoresponsive polymer structure and the thermomechanical processing provided, the SMP is able to achieve the desired shape memory or actuation behavior. In the following, the microscopic mechanisms employed for shape programming, fixing and recovery and the various ways to trigger shape recovery are presented. In addition, a brief overview over the current status of SMP actuation is given.

2.5.1. One-way shape memory effect (1W-SME)

In a typical CTM dual-shape cycle, a semicrystalline SMP specimen is first heated above its melting transition. Thereby, the crystallites melt and the polymer network becomes rubbery

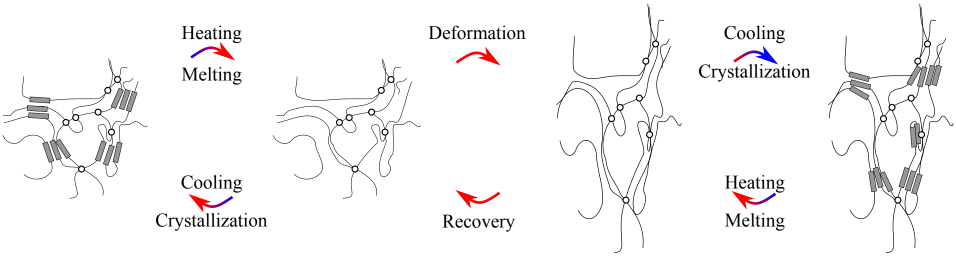

Scheme 2.8: Depiction of the microscopic mechanisms of shape fixing and shape recovery using a crystallization and melting transition. Details are given in the text.

(Scheme 2.8). Shape programming consists in the application of a deformation, followed by shape fixing through subsequent melt crystallization on cooling. The newly formed crystallites act as physical cross-links, which fix the temporary shape of the SMP. Subsequent heating induces melting, which resolves the crystalline cross-links. As a consequence, the specimen entropy-elastically recovers its almost permanent shape. The thermomechanical cycle can either be finalized by cooling to room temperature; alternatively, the adjacent cycle is directly appended.

In an alternative approach, the temporary shape of an SMP specimen is fixed by cooling below the glass transition.[116] Further approaches include temporary cross-links from light-induced photoreversible cycloaddition reactions in azobenzene[117] or by hydrogen bonding.[118] In simplified programming procedures, a quasi-plastic deformation of an SMP at a temperature below a suitable phase transition (‘cold drawing’) makes a distinct shape fixing step redundant.[119,120] Similarly, in polymers like natural rubber (polyisoprene), which does not crystallize under ordinary conditions, shape fixing can be achieved by strong deformation (‘hot drawing’) resulting in deformation-induced crystallization.[19] In any case, the shape fixing procedure is completed by stress release yielding a stable temporary shape.

Triggering is the antagonistic process to shape fixing, thus resolves the temporary network structure. In accordance with the applied shape fixing procedure, appropriate stimuli to trigger shape recovery in SMPs are selected. These include

- direct thermoresponsive triggering by specimen heating above
    - the melting transition,[83,113,121]
    - the glass transition[122,123] and
    - the dissociation transition of hydrogen bonding,[118] as well as
- indirect thermoresponsive triggering

  - by resistive and inductive heating with alternating electric[124] and magnetic fields,[125,126] respectively,
  - by exposure to infrared laser beam[127,128] or focussed ultrasound of high intensity[129] or
  - by lowering the glass transition temperature, *e.g.* by immersion in solvents,[130]
- photoresponsive triggering by exposure to light of specific wavelengths[117] and
- chemoresponsive triggering by variation of pH value.[131,132]

In essence, SMPs are thermo-, photo- or chemoresponsive.[92]

To employ more convenient stimuli and enable remote triggering, thermoresponsive SMPs can be triggered indirectly. For example, resistive (Joule) or inductive heating, infrared laser light transmitted by an optical fiber within the polymer matrix or focussed ultrasound of high intensity yield additional ways to locally heat the SMP. In case of chemoresponsiveness, the majority of described 1W-SMEs is triggered by a temperature shift of the phase transition, which has previously been employed to thermally fix the temporary shape. Examples are the immersion of styrene-based SMP in dimethylformamide (DMF)[130] as well as polyurethane SMP in DMF[133] and in water.[18] Here, a shift of the glass transition temperature above the ambient temperature occurs. Shape recovery in human or animal hair or nail (translucent keratin)[92] is enabled through dissociation of hydrogen bonds when exposed to water. In a special case, polymers containing hard segments from metal ligand complexes allow thermoresponsive triggering either directly or even indirectly both by chemical and photo-induced triggering.[134]

Photo- and chemoresponsive SMPs in the original sense, which are not thermoresponsive but solely rely on temporary photo- or chemoresponsive cross-linking, are rather rare. The former can be found in networks incorporating azobenzene groups in cinnamic acid, which carry out photoreversible cycloaddition reactions when exposed to alternating wavelengths (*e.g.* $\lambda > 260\,\mathrm{nm}$ or $\lambda < 260\,\mathrm{nm}$).[117,135] Actual chemoresponsiveness is known for pH-sensitive SMPs from cross-linked β-cyclodextrin modified alginate and diethylenetriamine modified alginate where shape fixing is conducted by elevations of the pH ≥ 11.5 and recovery triggered at pH 7.[132]

Depending on the SMP structure, the application of more than one temporary shape may be feasible. Adjacently, the applied deformations can be successively released, supplying multi-shape behavior.[116,136,137] In general, shape programming of multiple temporary shapes is achieved by two or more sequential shape programming procedures, each including a deformation and subsequent shape fixing procedure. By stepwise triggering, the intermediate temporary and finally the original shape are sequentially recovered.

In a first publication covering triple-shape properties in SMPs, phase-transitions of two different soft segments, the glass transition of poly(cyclohexyl methacrylate) and the crystallization/melting transition of a poly(ε-caprolactone) (PCL) soft segment within a multi-phase polymer network architecture were successfully employed.[138] For the same system, a one-step programming process to achieve triple-shape properties was designed by Behl *et al.*[139] Here, fixation of one deformation was achieved by cooling below both phase transitions in one cooling run. Stepwise heating yielded two distinct recovery steps. Alternatively, the crystallization and the glass transition temperature of one and the same PBA soft segment enabled triple-shape properties in an SMP.[27,28]

A slightly different approach to achieve triple-shape properties is given by the fabrication of layered polymer composites, which incorporate two epoxy-based[140] or organic-inorganic bilayers[141] with temperature-separated phase transitions, each supplying dual-shape properties. Even more, multiple deformations can be subsequently fixed and recovered at various temperatures within one broad glass transition in ionomeric perfluorosulfonic acid (Nafion®)[116] or in combination with a melting transition in semi-interpenetrating networks (achieving quintuple-shape properties).[137]

In any case, the 1W-SME (including multiple-shape changes) can be triggered only a single time. Once the specimen has recovered its original shape, it looses its thermoresponsivity. Repetition of the shape programming procedure is required to introduce the potential for another shape change.

2.5.2. Two-way shape memory effect (2W-SME)

In contrast, the ability of some semicrystalline SMPs to exhibit shape changes on cooling and heating under isotonic conditions is denoted as the 2W-SME, or as 'actuation behavior'. In case of tensile loading, the specimen expands on cooling and contracts on heating. Such actuation behavior has initially been observed in poly(cyclooctene)[8,38] and was confirmed for a number of cross-linked polymers with at least one crystallizable segment, including PCL cross-linked by POSS,[33] by DCP[63] or physically cross-linkedy by 4,4'-diphenylmethylene diisocyanate (MDI) and 1,4-butanediol (BD) as a chain extender.[29] Other SMPs capable of two-way shape memory are made from poly(ethylene-*co*-vinyl acetate) cross-linked by DCP[142] and networks of star-shaped poly(ω-pentadecalactone) (PPD)[40] as switching segments. Moreover, polymers incorporating two crystallizable soft segments, PCL and PPD, even exhibit two expansion and two contraction events, enabling the so-called reversible triple-shape effect.[39] On a side note, shape memory alloy/polymer hybrid materials are known to exhibit the 2W-SME.[9,143,144]

As a necessary condition for the 2W-SME, the elastomeric networks have to incorporate at least one crystallizable soft segment domain,[39] since thermoresponsive actuation is anticipated to rely on the effects of CIE and MIC.[38] Although much indirect evidence is given in literature, final prove for the correlation of oriented crystallization and mechanical specimen response on cooling, *i.e.* CIE, has not yet been given.

The typical 2W-SM procedure consists of the controlled application of isotonic conditions, which are maintained during the following thermal cycles. A thermal cycle includes cooling below the crystallization transition and heating above the melting transition temperature, while the established isotonic conditions are sustained.

In the last years, approaches have been made to enable free-standing actuation of SMP composites. The composite specimens were prepared by adhering a one-way programmed SMP component, capable of thermoreversible two-way shape memory behavior, to a flexible polymeric component. Initial heating of the composite structure induced recovery of the SMP component, leading to SMP contraction and hence composite deformation. The arising internal stress field between the components replaced the externally applied isotonic conditions. In result, the composites showed thermally-induced actuation behavior without application of an external stress. Examples for such composites are laminates of SMPUs and a flexible PU elastomer component[43,44] and an SMP rod embedded into an elastomeric matrix material.[45] The latter was able to perform a fully reversible transversal actuation of ∼ 10 %. Although able to induce reasonable movements, such composites suffer from inflexibility to adapt new shapes after fabrication and are restricted to relatively simple motions like bending / straightening and eventually expansion / contraction.

2.6. Applications

In principle, the scope of SMP applicability is as wide as that of plastics in general. So far, SMPs have found broad application in heat-shrinkable tubing[57] as well as in shrink-wrap packaging.[145] The increased reliability and functionality of recently developed SMPs open up new possibilities; additional fields for potential application, including biomedicine and aerospace industry, were identified. In biomedicine, SMMs allow for micro-invasive surgery in fields and cases, where dimensioning of tools and implants does not permit such a type of operation so far.

Devices like self-fitting tissue scaffolds or stents from SMPs are biocompatible, non-toxic and non-mutagenic. They typically have a temporary shape with optimized dimensions for delivery via catheter into the body. At the targeted location, the 1W-SME is triggered *in vivo*, transforming the stent from its temporary shape to the intended functional shape, aiming at recanalization of arteries, and therefore therapy stroke and myocardial infarction, removal of emboli, *etc.* (Figure 2.1). Finally, biodegradable polymers such as polyurethanes degrade into non-toxic substances, rendering adjacent operation for implant removal unnecessary.

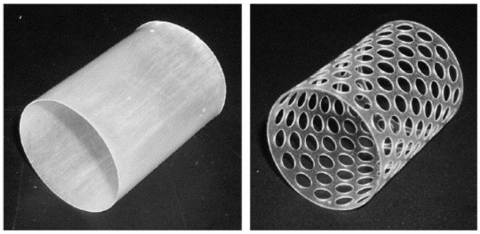

Figure 2.1.: Stents from SMPs. Reprinted from *Biomaterials*, **28**, C. Yakacki, R. Shandas, C. Lanning, B. Rech, A. Eckstein and K. Gall, Unconstrained recovery characterization of shape-memory polymer networks for cardiovascular applications, 2255-2263, (2007)[146] with permission from Elsevier.

A first device under the trade name MORPHIX®, an SMP-based suture anchor for graft fixation, received approval from the United States Food and Drug Administration in 2007 and has already hit the market. Other implants such as an interventional microactuator device for treating ischemic stroke are in the testing phase.[147] More shape memory devices are expected to come, *e.g.* stents for endovasculare strokes[148] and tissue scaffolds.[149]

In the scope of this work, a patent – granted in 2013 – aims to employ the 1W-SME in safety gloves for the medical field (Ref 1., List of Publications). By using SMPs as glove material, a good fit can be established while wearing a pre-expanded glove is simplified, even at increased material thickness. Thereby, the probability of perforation and accordingly the risk of infection of the surgeon during surgery can be minimized.

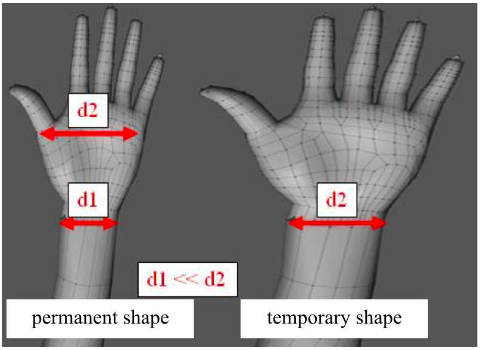

Scheme 2.9: Medical glove from SMPs in shapes optimized for working and wearing.

The SMP glove can be produced analogously to conventional gloves by dip coating. Thereby, a female mold is one or several times immersed in a polymer solution. The glove adapts its permanent shape. In the following step, programming of the glove is carried out in a process similar to blow molding. By heating above a suitable phase transition and parallel application of a pressure inside, it adapts to the outer shape of an oversized hand (Figure 2.9). Subsequent cooling below an appropriate phase transition fixes the temporary shape.

Prior to triggering, the user wears the expanded glove. In dependence of the particular shape recovery temperature, the body temperature of the wearer may already suffice to induce recovery and thus achieve a snug fit of the glove. Otherwise, an external source like hot air, water, or an infrared lamp can be employed to trigger the 1W-SME.

Furthermore, SMPs can be employed as switchable information carriers (Scheme 2.10). When the SMP tags labeled with Quick Response (QR) codes are deformed, the QR code cannot be read out using a code reading device, such as a smartphone. Initiating recovery of the SMP tag transfers the QR code back into a readable state. The technology is thought to be used in product and brand protection applications.[150–152]

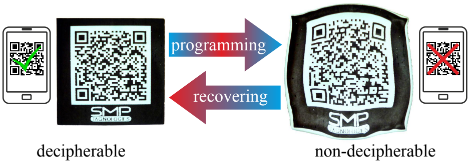

Scheme 2.10: Functionalized SMP tags labeled with QR code. The code can be unreadable (programmed shape) or decipherable (recovered shape).

From the thermodynamic point of view, entropy elasticity enables the use of elastomers as cooling agents. Heat can be transferred by stretching an elastomer outside and allowing it to relax inside of an isolated box, *e.g.* in refrigerators. SMPs can extend that functionality: recently not considered possible, SMPs were shown to be the first material which supplies cold storage, *i.e.* the possibility to absorb heat on application of a stimulus.[19]

In addition, the application of SMPs has been successfully tested in space.[20] Unfolding of SMP-composite driven devices enables the employment of large structures for use on satellites, such as solar arrays, solar sails, sunshields or parabolic antennas.[153] These devices meet strict size and weight restrictions[154,155] and hence reduce the budget of space transportation.

Futuristic concepts of morphing structures like bionic aircraft[156,157] and biomimetic underwater robots[158] employ actuators from smart materials and two-way SMMs. Patents have *e.g.* been granted on morphing wings.[159,160] The National Aeronautics and Space Administration (NASA) is currently working on concept airplanes, which mimic the eagle's flight (Figure 2.2). NASA expects, that this concept leads to a revolutionary new aircraft design, which could result in improvements in several ways. Adaptive and seamless wings would create less drag and reduce weight in comparison to conventional control surfaces. In effect, higher flight speeds, extended ranges or reduced fuel consumption could be achieved.[161,162]

Figure 2.2.: NASA concept airplane.

Moreover, bionic applications have been approached mimicking animal movements, among them swimming of fish[163] and jelly fish,[164] walking and running of animals[14] as well as humanoid movements.[165–167]

2.7. Open Questions

So far, in-depth research on SMPs, covering a broad range of basic material properties, microscopic mechanisms and applications-specific aspects, has led to a broad variety of potential applications. However, open questions remain and new questions constantly arise, which have to be answered in order to achieve a more profound understanding of SMPs and to further extend the shape memory functionality:

- How can strain recovery be interrupted to obtain intermediate stable shapes (multi-shape recovery)?
- How can recovery behavior be thermomechanically influenced? / Does polymorphic crystallization behavior impact the shape memory and actuation behavior of semicrystalline SMPs?
- How does actuation of semicrystalline SMPs and in particular CIE work? What is the role of microstructural orientation?
- How does SMP actuation under isotonic conditions depend on load?
- Can SMP actuation be realized without application of external load?

To answer these questions, the present thesis investigates the shape memory behavior of two series of SMPs. One consists of chemically cross-linked SPOSS-PU hybrid polymer networks synthesized around rigid inorganic cores, the other one of physically cross-linked PEU block copolymers supplied by the Bayer MaterialScience AG (Scheme 2.11). The raised questions are

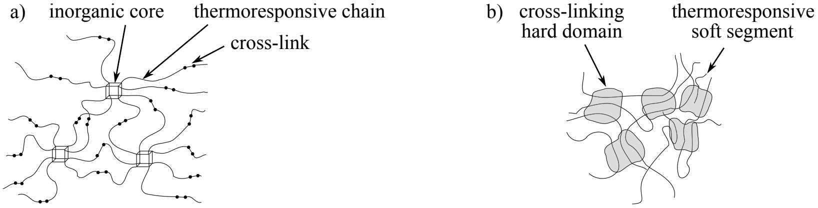

Scheme 2.11: Polymer networks: a) SPOSS-PU hybrids and b) PEU block copolymers for shape memory testing.

addressed by focusing on thermal and mechanical behavior as well as structural properties of the SMPs. Macroscopic shape changes were quantified in cyclic shape memory and actuation measurements. Additionally, the microscopic mechanisms were explored to progressively extend the shape memory and actuation behavior of the SMPs.

The following will be investigated after a comprehensive description of the experimental methods:

- The dual- (Chapter 4) and triple-shape (Chapter 5) recovery behavior of the series of SPOSS-PU nanocomposites.
- The dual-shape and actuation behavior of the series of PEUs and the influence of polymorphic crystallization behavior on the shape memory effect for one of those PEUs (Chapter 6).
- The effect of various thermomechanical pretreatments and associated constant load conditions on the subsequent actuation behavior in a physically cross-linked PEU (Chapter 7).
- The feasibility of stress-free bidirectional actuation and the microstructural orientation during cooling-heating cycles (Chapter 8).

3. Experimental

The following chapter reports on the investigated polymer networks and the experimental methods employed. Detailed description of the exact settings, testing programs and procedures is given were appropriate.

3.1. Materials

Two model networks containing crystallizable aliphatic poly(ester) soft segments were studied. On the one hand a series of organic-inorganic hybrid SPOSS-PUs was prepared by building block synthesis from star-shaped POSS-PCL blocks, which were finally cross-linked by PU. On the other hand, phase-segregated PEUs of various soft segment content from the Bayer MaterialScience AG were examined.

3.1.1. Synthesis of star-shaped polyhedral oligomeric silsesquioxane-poly(ε-caprolactone) poly-urethanes (SPOSS-PUs)

Octakis(dimethylsilyloxy) cubic silsesquioxane ($Q_8M_8{}^H$) was purchased from Hybrid Plastics Inc. (Product #: SH1310). Allyl alcohol (99%), stannous octoate ($Sn(Oct)_2$, 95%), hexamethylene diisocyanate (HMDI, 99%), and dibutyltin dilaurate (DBTDL) were obtained from Sigma-Aldrich. ε-Caprolactone (>99%) was supplied by Tokyo Chemical Industry and distilled over calcium hydride under reduced pressure for purification. Platinum divinyltetramethyl disiloxane complex, (Karstedt's catalyst) was acquired from Aldrich Co. and diluted to a solution of $2\,\mathrm{mmol\,l^{-1}}$ in dry toluene. Toluene was distilled from sodium/benzophenone under nitrogen prior to use. Other chemicals were used as received.

In a first step, octakis(dimethylsilyloxy) hydroxypropyl silsesquioxane (HPS) was produced by the direct hydrosilylation reaction of $Q_8M_8{}^H$ with allyl alcohol according to Laine *et al.*[85,168] Therefore, in a two-necked flask, 1.0 g of $Q_8M_8{}^H$ (0.98 mmol) was dissolved in 5 ml anhydrous toluene. 0.70 ml allyl alcohol (9.82 mmol) and 0.02 ml of the Kartedt's catalyst were added to the solution and the mixture was stirred at 40 °C for 15 min in argon atmosphere. Finally, a period of 24 h at 23 °C allowed the reaction to continue.

Table 3.1.: Chemicals used in SPOSS-PCL and SPOSS-PU synthesis for the various POSS-PCL ratios. Additional chemicals used for SPOSS-PU synthesis: 35 ml chloroform, 1 µl DBTDL.

	SPOSS-PCL synthesis			SPOSS-PU synthesis	
POSS-PCL ratio	HPS (g)	ε-CL (g)	$Sn(Oct)_2$ (µl)	POSS-PCL (g)	HMDI (µl)
160	1	12.3	9.87	7	228
200	1	15.4	12.31	7	185
240	1	18.5	14.79	7	156
400	1	30.8	24.62	7	80

For the POSS-PCL synthesis, 1 g HPS was added to predetermined amounts of ε-caprolactone and Sn(Oct)2 (0.10 wt%) using a Schlenk flask (Table 3.1). In greater detail, molar HPS-PCL ratios of 1:160, 1:200, 1:240 and 1:400 were chosen. To degas the mixture, a minimum of three cycles freeze-pump-thaw was conducted. Adjacently, the reaction was carried out for at least 12 h at 120 °C. Then, the mixture was diluted by chloroform and the product precipitated in excess amount of cold methanol. After repeating the precipitation process for two more times the product was dried *in vacuo*.

To obtain the final SPOSS-PU, POSS-PCL and Chloroform were inserted into a two-necked flask equipped with a magnetic stirrer. HMDI was added, after POSS-PCL was fully dissolved. The polyurethane reaction was started by the addition of DBTDL and carried out for at least 6 h at 23 °C and 200 rpm under argon atmosphere. Afterwards, the solution was poured into polytetrafluoroethylene plates. Degassing was allowed to take place inside a nitrogen oven for 24 h at 23 °C, before curing was conducted for 12 h at 80 °C. Purification with chloroform and subsequent vacuum drying yielded the final SPOSS-PU products.

3.1.2. Physically cross-linked poly(ester urethanes) (PEUs)

PEU elastomers including Desmopan® DP 2795A SMP, simply referred to as ‘PEU’, and a series of PEUs of similar composition, termed here ‘PEU-h(ssc)’, ‘PEU-m(ssc)’ and ‘PEU-l(ssc)’ in line with the highest (h), medium (m), and lowest (l) PBA soft segment content, were fabricated by the Bayer MaterialScience AG.

The soft segment was composed of PBA, which was obtained from a condensation reaction of 1,4-butanediol (BD) with adipic acid. In a patented soft segment pre-extension process,[169] the poly(adipate) diols reacted with excess of 4,4’-methylenediphenyl diisocyanate (MDI). Reactive pre-extended polymer chains formed. Finally, further quantities of MDI and BD were added to form the PU hard segment domains (Scheme 3.1).

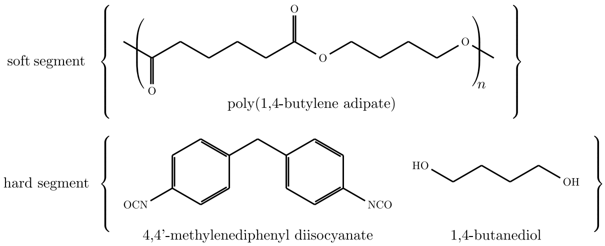

Scheme 3.1: Composition of PEU hard and soft segment.

Higher PBA chain length corresponded to increased amount of soft segment content. According to the Bayer MaterialScience AG, the molecular weight of Desmopan® DP 2795A SMP was $3500\,\mathrm{g\,mol^{-1}}$. The starting molecular weight of PBA used to synthesize the other PEUs was $4100\,\mathrm{g\,mol^{-1}}$. Further information regarding the synthesis of Desmopan® DP 2795A SMP is given in Ref.[170] The injection molded plaques with a thickness of 2 mm were used as received.

3.2. Methods

3.2.1. DSC

Calorimetric measurements were performed with an EXSTAR DSC 7020 from Seiko Instruments Inc. on PEU block copolymers and with a DSC 2920 from TA instruments on SPOSS-PU hybrids.

In a standard procedure, the samples of ∼ 5 mg in weight were heated from −25 °C to 100 °C at a rate of $\dot{T} = 10\,\mathrm{K\,min^{-1}}$, cooled to −60 °C at a rate $-\dot{T}$ and kept at −60 °C for 2 min. Finally, a second heating run to 100 °C at $\dot{T}$ was conducted. The first heating run reflected the thermal history of the specimen. Adjacent cooling and the second heating were employed to determine transition temperatures and enthalpies of crystallization / melting for the unbiased polymer. When thermomechanically pretreated specimens were investigated, cuts were taken from the middle of the tensile bar.

3.2.2. Mechanical characterization

The fracture mechanics at 23 °C were determined in uniaxial tensile tests using a Zwick Material Testing 1464. In advance, a 24 h temperature conditioning of tensile bars was carried out at 23 °C. After clamping with a gauge length of 10 mm, a preload of 5 N was applied. Then, the specimen was stretched with a rate of 0.5 $\%\,\mathrm{s}^{-1}$ ($3\,\mathrm{mm\,min}^{-1}$) until fracture occurred. From the obtained data sets, the Young's modulus, the specimen toughness, the elongation-at-break and the maximum tensile strength were determined.

For uniaxial tensile testing at 60 °C, an MTS Insight 10 device was employed in combination with the Thermcraft thermochamber. Before running a tensile test, the specimen was clamped with a gauge length of 10 mm and a pressure of 6 bar. After heating to 60 °C, the specimen was stretched with a strain rate of 0.5 $\%\,\mathrm{s}^{-1}$ to 800%.

Dynamic mechanical analysis (DMA) was conducted using a Netzsch DMA 242 (PEUs) and a DMA 2980 from TA Instruments (SPOSS-PUs), operating in single cantilever bending mode. Samples with dimensions of $5 \cdot 2 \cdot 2\,\mathrm{mm}^3$ were used. The temperature was ramped from -100 to 100 °C with a heating rate of $1\,\mathrm{K\,min}^{-1}$ (PEUs) and $3\,\mathrm{K\,min}^{-1}$ (SPOSS-PUs). The storage modulus E', the loss modulus E'' and the loss factor $\tan(\delta)$ were determined at a frequency $f = 1\,\mathrm{Hz}$. Since DMA results were found to be very sensitive to the thermal history of SMP samples (*e.g.* storage conditions), all samples were annealed for 10 min at 60 °C and stored at room temperature (at 23 °C and 50% air humidity) for at least one week, before their mechanical properties were studied in DMA.

Thermomechanical analysis (TMA) was conducted on $2.5 \cdot 2.5\,\mathrm{mm}^2$ cuts from SMP specimens using a Seiko Instruments TMA/SS120C. The temperature was ramped from -100 to 100 °C at a rate of $1\,\mathrm{K\,min}^{-1}$. Contact between the TMA stamp and the specimen was ensured using a force of 5 mN. To monitor changes in specimen thickness after application of a training procedure, a cut from an accordingly prepared specimen was transferred to the TMA. In this case, the temperature was cycled in between -10 and 60 °C at a rate of +/- $1\,\mathrm{K\,min}^{-1}$, while the thermally induced changes in specimen thickness were quantified.

3.2.3. Swelling experiments

Rectangular polymeric samples with a dimensioning of $33 \cdot 25 \cdot 2\,\mathrm{mm}^3$ and an initial mass m_0 in between 1.03 and 1.26 g were weighted in air and water at 23 °C with a Sartorius AC 211 balance. Then, the samples were stored for 6 h at 60 °C in the swelling agent ethyl acetate (EA) before the weighing procedure was repeated. In addition, the sample weights were determined after drying for 5 d on air (23 °C and a relative humidity of 50%). The volumes of the pristine and swollen state and the density of the SMPs were calculated using the buoyancy-floating method.

As basic parameters for the calculation of the degree of swelling Q and the cross-link density ν, the density of EA was given by $\rho_{EA} = 0.897\,\mathrm{g\,cm}^{-3}$ ($V_{EA} = 98.2\,\mathrm{cm}^3\,\mathrm{mol}^{-1}$, $M_{w,EA} = 88.1\,\mathrm{g\,mol}^{-1} \Rightarrow \rho_{EA} = 0.897\,\mathrm{g\,cm}^{-3}$).[171] The Flory polymer-solvent interaction parameter for PBA in ethyl acetate at 120 °C is $\chi_{PBA-EA} = 0.43$.[172]

3.2.4. CTMs

CTMs were conducted to quantify the shape memory and actuation behavior of SMPs, using an MTS Insight 10 electromechanical testing system, equipped with a Thermcraft thermochamber and a Eurotherm 2404 temperature controller unit (Figure 3.1). A Eurotherm 2404 temperature controller steered two electrical heating elements in the back of the thermochamber and a solenoid valve, which controlled the injection of liquid nitrogen from a dewar under a pressure of 0.5 bar into the thermo-chamber. Diffusion of air inside the chamber was provided by an electric motor-driven fan, shielded by a baffle to prevent direct exposure of the specimen to the air stream. An thermocouple was mounted near the specimen, with its tips placed inside a rectangular sample of the investigated material, in order to create conditions similar to those inside the specimen.


Figure 3.1.: Setup for cyclic thermomechanical measurements.

Dumbbell-shaped type 5 B tensile bars (EN ISO 527-2: 1996) or type S3A tensile bars (DIN 53504) were punched out of the 2 mm thick polymer samples and clamped at respective initial gauge lengths of 10 mm (type 5 B tensile bar) or 20 mm (type S3A tensile bar) into the pneumatic grips of the electromechanical testing system (Figure 3.2), using a clamping pressure between 3 or 6 bar (details for the individual measurements are given in Appendix A). In subsequent measurements, the specimen strain ε was directly determined from crosshead displacement and changes in tensile force were monitored with a 100 N load cell. The nominal tensile stress σ was calculated by normalizing the measured force to the initial cross section of the specimen, which by standard was 4 mm^2 (type 5 B tensile bar) or 8 mm^2 (type S3A tensile bar).

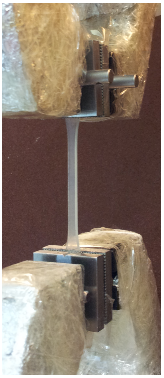
Figure 3.2.: Clamped specimen

In the following, the herein employed thermomechanical procedures for shape memory and actuation measurements are described. The selected parameters are given in the Appendix (Table A.1, shape memory measurements and Table A.2 actuation measurements).

The dual-shape properties of SMPs were characterized in two specific tensile testing programs. Shape recovery either quantified changes in strain (free strain recovery) or stress (fixed strain recovery). In both cases, shape memory cycling started with an identical shape programming procedure. It consisted in heating the specimens from room temperature (23 °C) to T_{high} at a heating rate $\dot{T}_h$, followed by an adjacent holding time and finally the tensile deformation to the maximum strain ε_m. Based on the stress-strain curve, the Young's modulus E and the loading stress σ_l were quantified.

After a temperature holding time, the change in stress during temperature holding $\Delta\sigma$ was recorded and the relative stress decrease $^{\Delta\sigma}/_{\sigma_l}$ calculated. Adjacently, shape fixing was conducted by cooling the specimens to T_{low} at a cooling rate $\dot{T}_c$. Two more holding times were applied, one preceding and the other one following a final stress release at a force rate $\dot{F}_u$. The fixed strain after unloading ε_u was either determined at T_{low} or after heating to 23 °C.

Subsequent to shape programming, the polymer response to heating was quantified. Free strain recovery was initiated by heating the specimen at the heating rate $\dot{T}_h$ to the temperature T_{high}, with the clamps maintaining zero tensile force and the crosshead following specimen contraction. After a final holding time t_h, which ensured stable thermal conditions and completed the thermomechanical cycle, the strain of the permanent shape ε_p was determined.

The strain recovery onset temperature $T_{r,onI}$ was defined as that temperature, where the tangent line through the inversion point of the strain-temperature curve intersected with a horizontal line at the strain ε_u.

In addition, the specimen's response to heating was determined in fixed strain recovery. Therefore, the strain of the programmed specimen was maintained at the constant strain ε_u and the maximum recovery stress $\sigma_{r,max}$ arising during heating to T_{high} at a heating rate $\dot{T}_h$ was quantified. In addition, $T_{r,onII}(N)$ was defined as the temperature, where the tangent line through the inversion point of the stress-time curve was zero. The thermomechanical cycle was either directly completed at T_{high} or an adjacent cooling run to room temperature (23 °C) and the respective holding time were added. In total, $N = 5$ thermomechanical cycles were conducted.

In triple-shape measurements, each of $N = 5$ thermomechanical cycles included two shape programming and two shape recovery events. Programming started by application of a first temporary shape after heating to T_{high} at a heating rate $\dot{T}_h$ and a subsequent holding time t_h. Deformation to a strain ε_{m1} at a rate $\dot{\varepsilon}$ was followed by another holding time and subsequent cooling to T_{mid} at a rate of $\dot{\varepsilon}$. Then, the second deformation ε_{m2} was applied at the same rate, again followed by a holding time and subsequent temperature decrease to T_{low} at the cooling rate $\dot{T}_c$. Similar to the dual-shape measurements, the Young's moduli during first and second deformation E_1 and E_2 and, where appropriate, the yield strain ε_{yield} were determined. In a final step, unloading of the stress at a force rate $\dot{F}_u$ and another holding time completed the programming procedures. Adjacently, the strain of the fixed shape A after two-fold programming was determined as ε_A.

Subsequently, the shape recovery behavior, *i.e.* the change in strain, was investigated by heating to T_{mid}, followed by a holding time and heating to T_{high} at a heating rate $\dot{T}_h$, which finalized the thermomechanical cycle. The induced changes in strain were monitored and the strains ε_B and ε_C of recovered shapes B at T_{mid} and C at T_{high} were recorded after holding times t_h. The recovered strains were calculated for the cycle N as

$$\varepsilon_{A\to B}(N) = \varepsilon_A(N) - \varepsilon_B(N), \tag{3.1}$$

$$\varepsilon_{B\to C}(N) = \varepsilon_B(N) - \varepsilon_C(N) \tag{3.2}$$

and the totally recovered strain

$$\varepsilon_{A\to C}(N) = \varepsilon_A(N) - \varepsilon_C(N) \tag{3.3}$$

In an alternative approach, shape B^* instead of B was determined on the basis of the underlying shape switching transitions; the equations are adapted accordingly. Finally, $T_{r,on}$ was defined as that temperature, where a sharp kink in the strain-temperature diagram was observed.

Actuation under isotonic conditions was established using a thermomechanical pretreatment, which was either stress- or strain-controlled. Stress-controlled pretreatments started by heating the SMP specimens from 23 °C to T_D. The temperature was maintained for a temperature holding time t_h, before an initial stress σ_i was applied at a rate of $\dot{\sigma}$. In a next step, the stress was reduced to the constant stress $\sigma_c = {}^2\!/\!_3\, \sigma_i$ at the unloading rate $-\dot{\sigma}$. After another temperature holding time at T_D, the strain ε_{pre} was recorded and the thermomechanical pretreatment completed.

In contrast, strain-controlled pretreatments differed by the way the load was applied and released. Here, the heated specimen was deformed to an initial strain ε_i at a strain rate $\dot{\varepsilon}$, resulting in the formation of a maximum loading stress σ_i. Subsequently, the strain was reduced at a strain rate $-\dot{\varepsilon}$ to ε_{pre} and the corresponding stress σ_c was recorded.

Independent of the thermomechanical pretreatment, the actuation behavior was tested in $N = 5$ thermal cycles, with the stress maintained at σ_c. One thermal cycle consisted in cooling to T_{low} at a cooling rate $\dot{T}_c$, a subsequent temperature holding time of t_h, adjacent heating to T_{high} at a heating rate $\dot{T}_h$ and final temperature holding at T_{high} for a time t_h. The thermally induced changes in strain $\Delta\varepsilon = \varepsilon - \varepsilon_{pre}$ were quantified; in one case, 20 consecutive cycles were run (for $\sigma_c = 1.25\,\mathrm{MPa}$).

For the investigation of triple-shape actuation, the stress-controlled pretreatment ($\sigma_i = 3.0\,\text{MPa}$, $\sigma_c = 2.0\,\text{MPa}$) was identically applied as described above, but extended by a final heating step to T_{high}. In this case, each of $N = 5$ thermal cycles consisted in cooling from T_{high} to T_{mid} at a cooling rate of $\dot{T}_{c1}$, cooling to T_{low} at a rate of $\dot{T}_{c2}$, heating to T_{mid} at a rate of $\dot{T}_{h1}$ and subsequent heating to T_{high} at a rate of $\dot{T}_{h2}$. Intermediate temperature holding times t_h were added after each step.

To enable stress-free actuation, a thermomechanical 'training' procedure was designed that essentially resembled a strain-controlled pretreatment, only differing by the stress release segment. In this case, heating to T_{high} and a temperature holding time were followed by deformation to ε_i at a strain rate $\dot{\varepsilon}$. During unloading, the stress was released at a strain rate $-\dot{\varepsilon}$ to a minimum stress $\sigma_c = 0.025\,\text{MPa}$ to maintain the steerability. Adjacently, thermal cycling was conducted under almost stress-free conditions between T_{high} and T_{low} at heating and cooling rates of $\dot{T}_h$ and $\dot{T}_c$, respectively. The changes in strain were monitored.

Thermomechanical training and the resulting actuation were also probed in alternative geometric loading scenarios. Therefore, a cylindrically-shaped and an S3A specimen were subjected to thermomechanical pretreatment under compressive and torsional loading conditions. In case of compression, the specimen was pretreated using the electro-mechanical MTS insight 10 testing system, equipped with a a 10 kN load cell. After heating to T_{high} at a rate $\dot{T}_h$, the stress σ_i was applied at a rate $\dot{\sigma}$ to the cylindrically-shaped specimens with a diameter of 30 mm and a height of 6.4 mm and subsequently released at $-\dot{\sigma}$. Quantification of changes in thickness was conducted in a thermomechanical analysis (see below).

In case of torsional training, manual application of five complete revolutions (1800°) was applied to an S3A specimen at 60 °C, before the deformation was fully released. The adjacent shape changes were followed by photography.

In general, the determined strain suffered from a systematic error arising from thermal expansion of the tensile rods. In particular, a constant position of the cross-head during shape programming (shape fixing) in conjunction with thermal contraction of the tensile rods on cooling applied an additional deformation to the specimen, yielding a net strain increase, in particular at low temperature. In result, significantly increased stresses were quantified.

In addition, actuation measurements were affected in the same way. In this case, changes in the length of tensile rods in relation to the observed shape changes are comparably high. Since thermal expansion of the rods was directed opposite to the quantified actuation, specimen expansion and contraction during thermal cycling were underestimated.

3.2.5. WAXS

Diffraction studies were conducted on SMP specimens using an INEL CPS 120 diffractometer equipped with an 120° curved position sensitive detector. The detector allowed a simultaneous data collection in 4096 bins over a range of 120° in 2θ. The setup was employed in Debye-Scherrer geometry. The X-ray source was a 1500Q sealed tube with a copper target. To average the crystallite reflections, contributing the diffraction pattern, the sample holder was rotated around the axis normal to the planar surface of the sample.

High-intensity WAXS measurements were performed at the synchrotron microfocus beamline μSpot (BESSY II of the Helmholtz Centre Berlin for Materials and Energy). The setup was employed as described in Ref.[173] The measurements were conducted at a wavelength of 1.00 Å and an exposure time of 120 s. A two-dimensional MarMosaic X-ray detector (CCD $3072 \cdot 3072$) collected the scattered intensities 200 mm behind the sample position. Processing of the obtained scattering images and conversion into diagrams of scattered intensities *vs.* scattering angle 2θ (with respect to the wavelength of the Cu-K_α-line) and scattering vector q was performed using the computer program FIT2D.[174] To determine the degree of crystallinity, the intensity *vs.* q was deconvolved. As a criterion, a reflex was attributed to crystallinity when its half width at half maximum did not exceed 1°.

In situ WAXS measurements were conducted during thermal cycles using the setup and settings described above. The samples were loosely clamped into a TCS 120 (Anton Paar) sample-holder unit. The temperature was steered using a TCU 50 temperature control unit. A Peltier heater and a Pt 100 temperature sensor are built into the cooling/heating block. The temperature was cycled between -10 and 60 °C at temperature rates of +/- 3 K min^{-1}. Each minute, a frame with an exposure time of 30 s was carried out.

3.2.6. Proton nuclear magnetic resonance spectroscopy (^{1}H-NMR)

^{1}H-NMR was performed using a Bruker DPX (400 MHz) NMR spectrometer. The samples were immersed in deuterated chloroform ($CDCl_3$). Chemical shifts δ are reported in ppm with the internal tetramethylsilane (TMS) signal at 0.0 ppm as a standard.

4. SPOSS-PUs and their Dual-Shape Properties[b]

In this chapter, the synthesis of a model polymer network for covalently cross-linked polymer network structures is presented. Nanostructured organic-inorganic hybrid SPOSS-PUs from PCL soft segment chains were selected due to their well-defined structures and their controllable thermal and mechanical behavior. In greater detail, SPOSS-PU networks were build from a core of rigid inorganic POSS with PCL network chains attached to each of its eight corners. PCL was used due to its thermoplastic behavior, high elasticity and melting temperatures ranging from 45 to 67 °C.[37] Polyurethane hard segments from HMDI connected the dangling PCL chains, thereby cross-linking the SPOSS-PCL to form a three-dimensional SPOSS-PU network.

The basic thermal and mechanical properties are given and discussed. Shape memory measurements were systematically conducted around the PCL crystallization and melting temperatures. In that respect, the mechanical response of the programmed SPOSS-PU specimens to heating was studied under free strain as well as fixed strain conditions in five thermomechanical cycles. Particular interest was devoted to the influence of the PCL chain length on the shape memory properties of the SPOSS-PUs.

4.1. Molecular Structure

4.1.1. Star-shaped POSS-PCL macromolecules

SPOSS-PU synthesis was carried out in a multi-step procedure. In a first step, HPS was prepared by tethering the reactive silicon vertices of POSS with hydroxyl (OH) groups. The newly formed complex was employed as the starting point for building block synthesis. At the attached OH groups, ring opening polymerization of the ε-CL monomers started. The PCL chain length was set by the POSS/PCL feed ratio (molar ratio of M_{POSS}/M_{PCL}, Table 4.1) to obtain various PCL arm lengths and thus modify the macromolecular structure. This ratio also governed the hard and soft segment content (HSC and SSC, respectively). The former corresponds to the cross-

---

[b] Chapter adapted from Ref. 2. (List of Publications) with permission from The Royal Society of Chemistry.

Table 4.1.: Theoretical molar ratio of POSS to PCL (M_{POSS}/M_{PCL}), hard and soft segment content (HSC and SSC, respectively) and repeating unit $R.U.$ of PCL chains as well as $R.U._{NMR}$ determined from ^{1}H-NMR.

	M_{POSS}/M_{PCL}	HSC (wt%)	SSC (wt%)	$R.U.$	$R.U._{NMR}$
SPOSS-PCL 160	1:160	16.7	83.3	20	19
SPOSS-PCL 200	1:200	15.7	84.3	25	25
SPOSS-PCL 240	1:240	15.1	84.9	30	30
SPOSS-PCL 400	1:400	13.8	86.2	50	49

link density, while the latter is equivalent to the average PCL chain length. SPOSS-PCLs from four different POSS-PCL ratios, targeting at PCL repeating units of 20, 25, 30 and 50, were synthesized.

NMR was carried out in order to evaluate the structure of the star-shaped POSS-PCLs. An exemplary plot is given for SPOSS-PCL 160 (Figure 4.1).

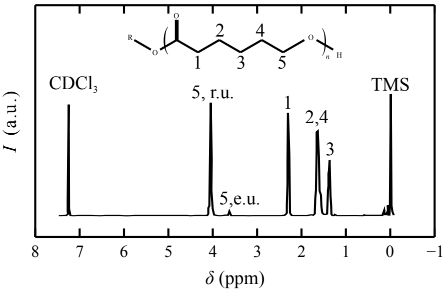

Figure 4.1.: Intensity I *vs.* chemical shift δ of ^{1}H-NMR for SPOSS-PCL 160 and ascription to the respective atomic units (5,r.u. marks the unit within the PCL repeating unit and 5,e.u. within the PCL end unit).

Most importantly, the signals at $\delta = 4.05$ ppm and $\delta = 3.62$ ppm were ascribed to the —CH_2 groups of the repeating and end units of the PCL chains, respectively. The ratio of the integrated intensities of these peaks reflected the amount of the corresponding units in the investigated samples and therefore allowed to deduce the mean PCL repeating unit. Table 4.1 compares the theoretical and experimentally verified SPOSS-PCL parameters. A comparably good agreement was found, which suggested that the PCL chains formed the predicted POSS-PCL stars with PCL chains attached to each of the 8 POSS OH groups.

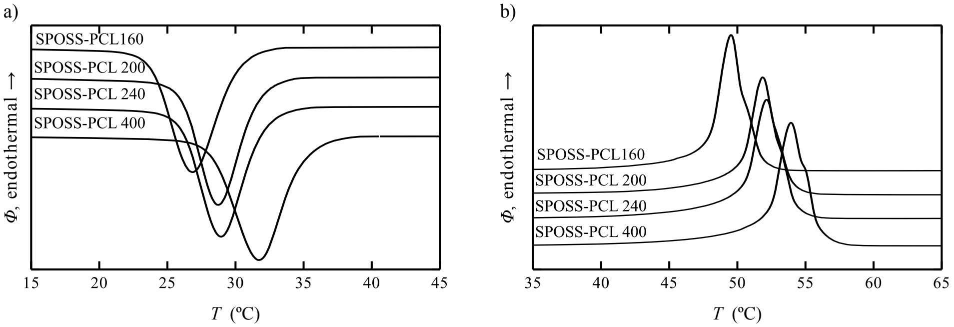

Figure 4.2.: DSC thermograms showing a) crystallization (cooling) and b) melting (second heating) of PCL for the series of SPOSS-PCLs at heating and cooling rates of +/– 10 K min^{-1}.

To study the thermoresponsiveness of the POSS-PCLs, thermal characterization was conducted by means of DSC in between −80 to 120 °C. No signal hinting at the glass transition has been observed. Endo- and exothermic peaks in the thermograms of cooling and second heating indicated PCL crystallization between 27 and 32 °C and PCL melting at temperatures between 50 and 54 °C (Figure 4.2). Increased PCL chain length yielded higher transition temperatures. This finding is in line with the dependence of crystallization and melting transition temperature on the chain length in PCL homopolymer,[37] similar POSS-PCLs[175] and for homogeneous polymers and copolymers in general.[52]

A slightly lower degree of crystallinity at decreased PCL chain length was observed, as evident by a relative increase of the crystallinity by 6% between SPOSS-PCL 160 and 400. This trend may be due to a depression in the PCL crystallinity, resulting from constraining effects of the PCL bindings to the POSS cores. Such observations have been made for star-shaped polymers and dendrimers from PCL chains.[176] Moreover, the sharp and unimodal melting transition profiles indicated narrow distributions of the PCL lamellar thickness. This finding further supported the previously drawn deduction that ring opening polymerization of PCL yielded SPOSS-PCL macromolecules with homogeneous PCL chain length.

4.1.2. SPOSS-PU networks

In the final step of the synthesis procedure, the PCL chain ends of the POSS-PCL macromolecules were cross-linked using HMDI and DBTDL as catalyst to form polyurethane. A full chain from PCL and PU connecting two POSS cores is sketched in Scheme 4.1. Scheme 4.2 depicts the

Scheme 4.1: Full SPOSS-PU chain from PCL and HMDI, connecting two POSS cores.

covalently cross-linked SPOSS-PU network. As a potential structural factor, the presence of PU segments on the one hand and POSS nanoparticles on the other hand principally allow for the formation of hard domains. Such structures may act as additional physical cross-links. PU hard domains are commonly employed in thermoplastic PEUs. Crystalline POSS domains in POSS-PCL networks have been observed by Lee *et al.*[33] However, previous studies on systems similar to the present one have shown that the formation of PU linkage disrupts the formation of POSS domains.[30] However, the formation of either PU or POSS domains can not be fully excluded.

The PCL chains of various lengths constituted the thermoresponsive soft segment. At increased PCL chain length, *i.e.* higher PCL soft segment content, the POSS and PU content and accordingly the chemical cross-link density were lower (compare Formula 2.5). Consequently, the SPOSS-PUs were named according to their POSS-PCL ratio. More details on synthesis and characterization of SPOSS-PUs are given in Refs.[30,177]

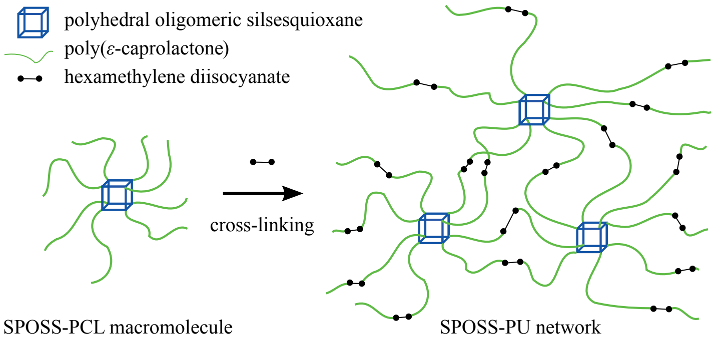

Scheme 4.2: SPOSS-PU network synthesis from SPOSS-PCL macromolecules.

4.2. Mechanical Properties

The viscoelastic properties of SPOSS-PUs were investigated in DMA. As a main finding, the peak temperature of the loss factor tan(δ), here associated with the glass transition temperature T_g of the PCL soft segment, was consistently observed at $\sim -30\,°\mathrm{C}$.

Significantly lower glass transition temperatures T_g at $-64\,°\mathrm{C}$ have been observed in DSC for PCL homopolymer with molecular weights of $125\,000\,\mathrm{g\,mol^{-1}}$ (commercial TONE® 787) according to Refs.[178,179] In a similar system from POSS and PCL, a slightly higher glass transition temperature of $-50\,°\mathrm{C}$ was observed and explained by constraining effects from cross-linking.[33] In good agreement with the present finding, T_g was independent from the POSS content. Here, the attachment of the PCL chains to the POSS and PU units may have even stronger constrained the degree of freedom of the PCL chains, thereby further shifting the glass transition to higher temperatures.

The glass transition was accompanied by a strong decrease of the storage modulus G'. This decrease was most pronounced at high POSS contents and low PCL chain length. Figure 4.3 exemplarily depicts the viscoelastic behavior of SPOSS-PU 200. When heated from -70 to $50\,°\mathrm{C}$, the modulus G' decreased by one order of magnitude from 3.2 GPa to 0.3 GPa. Low values of the tan(δ) in between 0.04 and 0.10 exemplify the low viscous response, which also manifested in small values of the loss modulus G''. G'' had a maximum of of 215 MPa (at $-40\,°\mathrm{C}$) and even lower values at deeper and higher temperatures. In turn, the dominance of the storage modulus G' indicated pronounced elastic responses of the chemically cross-linked SPOSS-PU network and suggested highly reversible, elastic shape changes and good recoveries during shape memory testing.

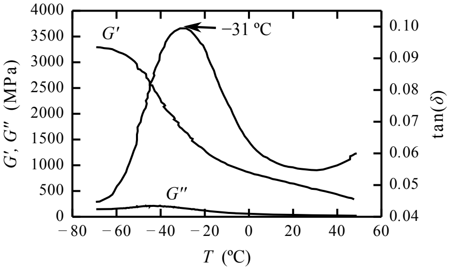

Figure 4.3.: DMA measurements: storage modulus G', loss modulus G'' and loss factor tan(δ) *vs.* temperature for SPOSS-PU 200 ($f = 1\,\mathrm{Hz}$).

4.3. Dual-Shape Properties

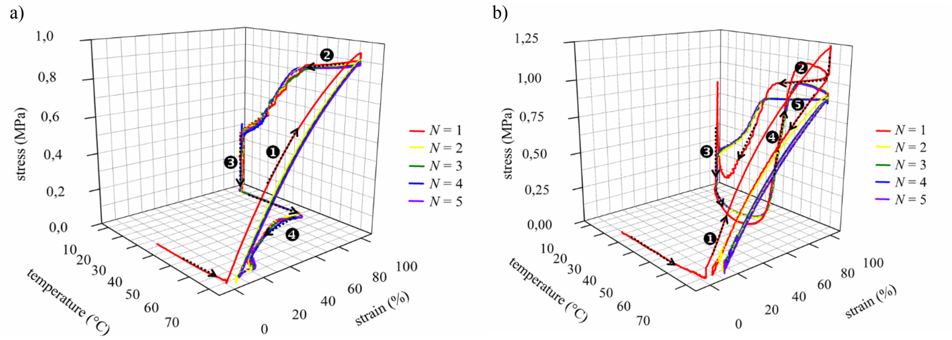

Figure 4.4.: Five shape memory cycles for SPOSS-PU 160 using two different recovery scenarios. Shape programming includes ❶. deformation to 100%, ❷. cooling from 70 to 10 °C and ❸. stress release. Recovery is triggered by ❹. heating a) under free strain conditions and b) under fixed strain conditions. Finally, ❺. unloading releases the resulting recovery stress (only in b).

In a next step, the shape memory behavior of SPOSS-PUs was studied. The low and high temperatures of the shape memory cycle were set to 10 and 70 °C in order to clearly exceed the PCL crystallization and melting peak temperatures on cooling and heating by at least 15 °C, respectively. Shape programming prepared the specimens for subsequent shape recovery. Two thermally triggered recovery scenarios were investigated. Five shape memory cycles are exemplarily depicted for SPOSS-PU 160 in Figure 4.4: in one scenario, the heated specimens were allowed to contract and the recovered strain was quantified (free strain recovery, Figure 4.4a). In another scenario, the length of the heated specimen was kept constant and the thermally induced stress was monitored (fixed strain recovery, Figure 4.4b). In any case, the thermomechanical cycle started by shape programming, preparing the SPOSS-PU specimens for shape memory.

4.3.1. Shape programming

Prior to shape programming, SPOSS-PUs were heated to 70 °C. In step ❶ of the thermomechanical cycle, the heated SPOSS-PU specimens were deformed to a strain of 100%. The corresponding stress-strain curves show a monotonously increasing stress and a typically elastomeric deformation profile. Values of the Young's modulus $E(70\,°C)$ (Table 4.2) were determined from the initial value ($\varepsilon = 0\%$) of the stress-strain derivative. For comparison, the shear moduli from

Table 4.2.: Young's modulus E and loading stress σ_l for the series of SPOSS-PU during shape programming in the first cycle ($N = 1$) and cycle-averaged ($N = 2 - 5$).

	E (MPa)		σ_l (MPa)	
	$N = 1$	$N = 2 - 5$	$N = 1$	$N = 2 - 5$
SPOSS-PU 160	2.6 ± 0.2	1.9 ± 0.2	1.3 ± 0.1	1.0 ± 0.1
SPOSS-PU 200	1.4 ± 0.2	1.0 ± 0.1	0.7 ± 0.1	0.6 ± 0.1
SPOSS-PU 240	1.1 ± 0.2	1.0 ± 0.1	0.8 ± 0.1	0.5 ± 0.1
SPOSS-PU 400	0.7 ± 0.2	0.4 ± 0.1	0.3 ± 0.1	0.2 ± 0.1

DMA measurements (Section 4.2) were converted to tensile moduli (Section 2.4.3). As a result, $E(50\,°\mathrm{C}) \geq 680\,\mathrm{MPa}$ (SPOSS-PU 200) exceeded the corresponding value of the Young's modulus E during tensile deformation at 70 °C by more than two orders of magnitude. This strong difference clearly demonstrates that the melting transition was exceeded, once again exemplifying that the SPOSS-PUs specimens were in their rubbery state.

The highest Young's moduli E were found at the lowest PCL chain length (SPOSS-PU 160) and the highest amount of POSS, which corresponds to the findings for G' from DMA below the melting PCL transition. In parallel, the loading stress σ_l, which was determined after deformation to 100%, increased at higher cross-link density and reached up to 1.3 MPa in SPOSS-PU 160. These trends are in good agreement with the generic dependence of mechanical properties, *i.e.* resistance to deformation, on the cross-link density of elastomers and SMPs.[42,180] In subsequent thermomechanical cycles ($N = 2$ – 5), a decrease of E and σ_l was observed for all SPOSS-PUs mainly between the first and the second thermomechanical cycle. This suggests that irreversible deformation occurred mainly during the first cycle. The following cycles only marginally contributed to further irreversibility.

After deformation, slight isothermal stress decrease $\Delta\sigma$ occurred while the strain was kept constant for 5 min at 70 °C (Table 4.3). A time-dependent stress decrease was observed and attributed to the viscoelastic phenomenon of stress relaxation.[102] For the sake of simplicity, the relaxation is here represented by the ratio of stress decrease to loading stress ${}^{\Delta\sigma}/_{\sigma_l}$. SPOSS-PUs with increased PCL chain length exhibited the highest ratio ${}^{\Delta\sigma}/_{\sigma_l}$.

The molecular bases of stress relaxation are ambiguous. Viscous flow and slipping of poly-

Table 4.3.: Absolute and relative stress decrease $\Delta\sigma$ and ${}^{\Delta\sigma}/_{\sigma_l}$ during SPOSS-PU holding at $\varepsilon_m = 100\%$ and 70 °C ($N = 1$).

	$\Delta\sigma$ (MPa)	${}^{\Delta\sigma}/_{\sigma_l}$
SPOSS-PU 160	0.15	0.12
SPOSS-PU 200	0.09	0.13
SPOSS-PU 240	0.08	0.13
SPOSS-PU 400	0.07	0.26

mer chains may have played a role. In additional, silicon and oxygen are known to show interchanging Si—O bonds.[181] More relevantly to the present case, bond interchanges have also been observed in siloxane polymer networks, as described in Ref.[182] In the presence of stress, the bonds tend to rearrange themselves such that the stress is reduced. The same mechanism might have applied here, slightly reducing the stress during temperature holding.

Shape programming proceeded by cooling the SPOSS-PU specimens to 10 °C (step ❷). In result, the stress decreased and the temporary shape was fixed due to two parallel processes.Firstly, crystallization transformed a part of the amorphous, rubbery PCL soft segment into crystalline domains. Consequently, this fraction omitted to further supply the entropy-elastic stress and even started to effectively cross-link the deformed SPOSS-PUs, thereby stabilizing the temporary shape. Secondly, even the stress from the remaining amorphous PCL soft segment decreased due to the proportionality of the entropy-elastic stress and temperature (Section 2.3.2).

In the vicinity of 10 °C, a final stress increase was attributed to the interaction of a measurement artifact from the tensile testing system and thermal contraction of the SPOSS-PU specimen (see also Section 3.2.4). However, a clear trend was apparent for the SPOSS-PU series (compare Figure 4.5, Section 4.3.3), making a closer look worthwhile. The measured stress increase was negligible in SPOSS-PU 160 and most pronounced in SPOSS-PU 400. In this temperature regime, slight thermal contraction of the tensile rods at maintained cross-head position induced a small deformation of the semicrystalline SPOSS-PUs. Consequently, the observed trend can be explained by differences in the specimens stiffness on the one hand and of the temperature, were it became stiff, *i.e.* the crystallization temperature. The latter increased with higher soft segment content and apparently dominated the observed effect. For SPOSS-PU 400, a high crystallization temperature allowed for stress formation over an extended temperature interval (more than 20 °C). Moreover, highest PCL content in the series suggests an increased degree of crystallinity, favoring highest moduli of these specimens in the semicrystalline state. In turn, almost insignificant stress increase in SPOSS-PU 160 for cycles $N = 2 - 5$ was ascribed to the lower PCL chain length and crystallization temperature. To sum up, the final stress increase resembles the SPOSS-PUs' response to deformation at low temperature. A detailed discussion of deliberate SPOSS-PU deformation at 10 °C is given in Section 5.1.

Shape programming was finalized by stress release at a rate of $5\,\mathrm{N\,min^{-1}}$ and heating to 23 °C. In result, the specimens contracted by 1 to 4% (step ❸). The resulting temporary shapes were stable at a fixed strain ε_u. The corresponding shape fixity ratio R_f for the SPOSS-PUs is given in Table 4.4. In any case, shape fixity ratios of more than 96% were observed. Although of low difference, the shape fixity tended to slightly increase with increasing POSS content. Comparable enhancements of the shape fixity with increasing hard segment content have been observed in PU block copolymers.[24,183]

Table 4.4.: Shape memory properties for the series of SPOSS-PUs in the first thermo-mechanical cycle ($N = 1$) and cycle-averaged ($N = 2 - 5$). Given are the shape fixity ratio R_f, the recovery onset temperature $T_{r,onI}$, the total recovery ratio $R_{r,tot}$ and the recovery ratio R_r.

	R_f (%)		$T_{r,onI}$ ($°C$)		$R_{r,tot}$ (%)		R_r (%)
SPOSS-PU	$N = 1$	$N = 2 - 5$	$N = 1$	$N = 2 - 5$	$N = 1$	$N = 2 - 5$	$N = 2 - 5$
160	98 ± 1	98 ± 0.2	48 ± 1	48 ± 1	92 ± 3	91 ± 2	98 ± 3
200	99 ± 1	98 ± 0.1	47 ± 1	46 ± 1	91 ± 3	88 ± 1	99 ± 1
240	96 ± 1	97 ± 0.1	50 ± 1	50 ± 1	93 ± 3	89 ± 1	99 ± 1
400	96 ± 1	96 ± 0.1	59 ± 1	59 ± 1	79 ± 3	75 ± 6	94 ± 8

In a progressive approach, the influence of the artifactual stress on the shape programming procedure was reduced. SPOSS-PU 400 was exemplarily selected, because its measurement suffered from the highest artifactual stress. Therefore, the principle measurement procedure stayed identical with the exception of the lower testing temperature T_{low}. In order to avoid final stress increase, T_{low} was increased to 23 °C, which is close to the offset of the crystallization transition of PCL. As a result, much lower stresses during shape fixing (0.95 MPa *vs* 3.5 MPa for cycles $N = 2-5$) and consistent enhancements of the shape fixity were quantified ($R_f(N = 1)$: 97%; $R_f(N = 2 - 5)$: 97%). This approach demonstrated that the adaptation of the testing parameters to the individual SPOSS-PU composition influences the quantified shape programming parameters.

4.3.2. Free strain recovery

In step ❹ of the thermomechanical cycle, the shape (strain) recovery behavior of the programmed SPOSS-PU specimens was investigated under free strain conditions (Figure 4.4a). When heated from 10 to 70 °C, a slight initial increase in strain (between 1 and 3%) was due to thermal expansion of the SPOSS-PU specimens (and slight expansion of the tensile rods of the electromechanical testing system). At the onset recovery temperature $T_{r,onI}$, further heating initiated specimen recovery. In principle agreement with the trend in DSC melting temperatures, the higher PCL content shifted $T_{r,onI}$ to increased temperatures (Table 4.4). Here, melting of the crystalline network chains transformed the stiff, crystalline domains into molten soft segment. As a consequence, the SPOSS-PU networks regained their rubbery characteristics. Entropyelastic specimen contraction drove recovery of the almost permanent shape.

The recovered strain ε_u was determined after holding the SPOSS-PU specimens for 5 min at 70 °C; the shape recovery ratios R_r and $R_{r,tot}$ are given in Table 4.4 (above). As expected from the low values of the loss factor tan(δ) and the loss modulus G'', excellent shape recovery ratios R_r of almost 100% were observed for all SPOSS-PU specimens in cycles $N = 2 - 5$.

With proceeding thermomechanical cycling, all the SPOSS-PU specimens exhibited a slight cyclic decrease of the shape fixity R_f and total shape recovery ratio $R_{r,tot}$. However, stable cyclic thermomechanical behavior was established, as exemplified by values of the shape recovery ratio $R_r(N = 2-5)$ close to 100%. It can be concluded, that after initial adaptation to shape programming in the first thermomechanical cycle, the cyclic shape memory behavior for the specimens is highly reliable and reproducible.

Pronounced dual-shape properties have also been observed in similar SPOSS-PCL networks[33] and POSS-poly(lactide-*co*-glycolide) (PLGA) networks,[34] when these were triggered by heating above both the PCL / PLGA and the POSS melting transition. In the latter case, the melting temperature of POSS moieties and the glass transition temperature of PLGA were employed to achieve shape fixity and recovery ratios close to 100%. It has to be added, however, that fixing and recovery by two transitions requires a broad temperature interval, in the considered case from 25 to 120 °C.

In the present case, a composition-dependent trend was apparent in the total recovery ratios $R_{r,tot}(N = 2-5)$, which reflect the amount of the elastically recoverable SPOSS-PU deformation on heating. Highest values of $R_{r,tot}(N = 2-5)$ were found at increased POSS content. The tendency of lower recovery ratios at decreased PCL chain length contrasts observations in other SMPs from PCL soft segment, including polyurethanes from PCL[22] and PCL cross-linked by DCP.[38] Here, the fraction of unrecoverable, residual strain ($\varepsilon_r = 100\% - R_{r,tot}(N = 2-5)$, values in between 9 and 25%), which is the main factor for lowered shape recovery, was in good quantitative agreement with the observed relative stress decrease $^{\Delta\sigma}/_{\sigma_l}$ during stress relaxation. Accordingly, stress relaxation is expected to provide a major contribution to irreversible deformation, most apparent during shape programming at high PCL content (Subsection 4.3.1). Consequently, lower (total) shape recovery was observed at increased PCL chain length.

Under the adapted testing conditions with a modified lower testing temperature, shape recovery in SPOSS-PU 400 slightly improved ($R_{r,tot}(N = 1)$: 85%; $R_{r,tot}(N = 2-5)$: 76%) and $R_r(N = 2-5)$: 97%). However, even under these conditions, SPOSS-PU 400 was unable to achieve the same fixity and (total) recovery ratios as SPOSS-PU 160 did, such that the general finding stayed valid: lower network chain length and higher amount of chemical cross-linking from POSS result in an increased total shape recovery $R_{r,tot}(N = 2-5)$.

4.3.3. Fixed strain recovery

In the second recovery scenario, the response of identically programmed SPOSS-PU specimens to heating at a fixed strain ($\varepsilon = \varepsilon_u$) was evaluated (step ❹). The strain, stress and temperature of the first thermomechanical cycle are depicted for all the SPOSS-PUs in Figure 4.5. Heating

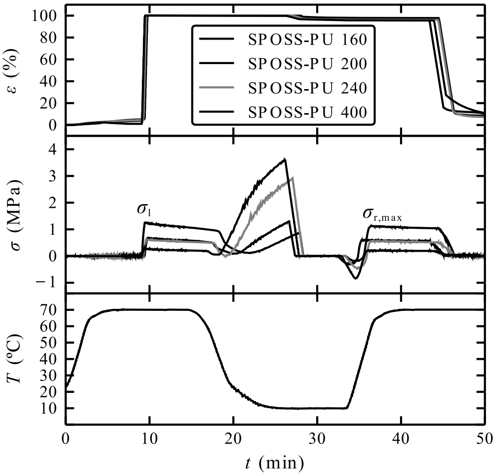

Figure 4.5.: One shape memory cycle including programming and fixed strain recovery ($\varepsilon_m = 100\%$, $N = 1$); plotted are strain ε, stress σ and temperature T *vs.* time t for the different SPOSS-PUs.

of the programmed specimen under fixed strain conditions initially build up a negative stresses, illustrating the incipient development of an expansive force. This finding corresponds to the slight initial expansion observed under free strain conditions.

When heated further, stress started to increase at the stress recovery onset temperature $T_{r,onII}$, where melting of the soft segment crystallites within the SPOSS-PU specimens set in (Table 4.5). A composition-dependent trend of the recovery onset temperature $T_{r,onII}$ confirmed the trend observed for the onset temperatures during free strain recovery $T_{r,onI}$. However, the temperatures

Table 4.5.: Shape memory properties of fixed strain recovery for the series of SPOSS-PU for the first thermo-mechanical cycle ($N = 1$) and cycle-averaged ($N = 2-5$).

	$\sigma_{r,max}$ (MPa)		$T_{r,onII}$ (°C)		R_S (%)	
	$N = 1$	$N = 2-5$	$N = 1$	$N = 2-5$	$N = 1$	$N = 2-5$
SPOSS-PU 160	1.1 ± 0.1	1.0 ± 0.1	41 ± 1	41 ± 1	88 ± 1	100 ± 6
SPOSS-PU 200	0.6 ± 0.1	0.5 ± 0.1	49 ± 1	48 ± 1	86 ± 1	97 ± 2
SPOSS-PU 240	0.6 ± 0.1	0.5 ± 0.1	51 ± 1	52 ± 1	87 ± 1	93 ± 7
SPOSS-PU 400	0.2 ± 0.1	0.2 ± 0.1	55 ± 1	55 ± 1	68 ± 1	76 ± 4

of the stress recovery onset $T_{r,onII}$ are consistently lower than the stress recovery temperature in free strain shape recovery.

Slightly below 70 °C, the stress reached the maximum recovery stress $\sigma_{r,max}$ and formed a plateau during the adjacent temperature holding time. In accordance with the loading stress quantified during shape programming, highest $\sigma_{r,max}$ arose at high cross-link density and decreased with higher network chain length. In line with the above described stress relaxation behavior, $R_S(N = 1)$ values significantly below 100% point out, that irreversible deformation must have taken place prior to the first stress recovery. In analogy to the shape (strain) recovery ratio R_r, the stress recovery ratio R_S approximates 100% in the subsequent cycles. In particular, highly cross-linked SPOSS-PUs exhibited an almost perfectly reversible deformation. Final stress release (step ❺) transfered the specimen close to its initial shape and finalized the thermomechanical cycle under fixed strain conditions.

4.4. Conclusion

A series of SPOSS-PU networks were synthesized in a stepwise procedure. First, PCL chains were attached to inorganic POSS cores. NMR and DSC showed the formation of homogeneous SPOSS-PCL macromolecules, which were then chemically cross-linked to obtain SPOSS-PU networks.

In CTMs, the PCL crystallization and melting transition were employed for shape fixing and triggering of shape recovery, respectively. The SPOSS-PU with the highest POSS content showed highly reliable shape memory performance, as demonstrated by cycle-averaged shape fixities, shape recoverabilities and stress recoverabilities close to 100%. Stress relaxation after deformation at 70 °C was identified as the main source of irreversible deformation, which slightly reduced the shape memory performance of SPOSS-PUs, in particular at increased PCL chain length. As potential cause, viscous flow of PCL chains and the occurrence of SI—O bond interchanges were considered. An effective way to minimize viscous flow was given by the incorporation of high POSS content and accordingly increased cross-link density from covalent bonds. Finally, modification of the network structure allowed to obtain recovery onset temperatures in between 41 and 59 °C.

5. Triple- and Multi-Shape Properties of SPOSS-PUs[c]

In a progressive approach, the previously shown dual-shape programming procedure was extended to enable triple-shape properties for the same series of SPOSS-PUs. As before, the SPOSS-PU specimens were transformed from their original to a first temporary shape, fixed by cooling below the PCL crystallization transition temperature. Subsequently, a second programming step applied an additional deformation, this time fixed by cooling below the glass transition temperature of the PCL soft segment. The response of the thermomechanically programmed SPOSS-PUs to stepwise heating above the glass and melting transition was studied under free strain conditions.

The investigations focussed on the influence of the PCL chain length on the triple-shape properties, the characteristics of shape recovery triggered by heating above the PCL glass and melting transition temperatures and the interrelation of the two programming and recovery steps. Finally, the ability of SPOSS-PUs to exhibit multi-shape properties, *i.e.* recover and maintain several shapes during staged heating, was examined.

5.1. Triple-Shape Properties

Four SPOSS-PUs of different PCL chain lengths were investigated in triple-shape measurements. Figure 5.1 shows the stress-strain-temperature diagrams for the first of five thermomechanical cycles for each SPOSS-PU. During triple-shape programming, two subsequent deformations to strains $\varepsilon = 100\%$ and 200% were fixed by cooling to $10\,°\mathrm{C}$ (below the PCL crystallization, $T_c \geq 27\,°\mathrm{C}$, Section 4.1.1) and $-40\,°\mathrm{C}$ (below the PCL glass transition, $T_g \sim -30\,°\mathrm{C}$, Section 4.2), respectively. Subsequently, incremental heating of the thermomechanically programmed SPOSS-PUs to 30 and 70 °C allowed to recover from the two-fold fixed, temporary shape A to the once fixed, temporary shape B and finally to shape C.

---

[c] Chapter adapted from Ref. 3. (List of Publications) with permission from The Royal Society of Chemistry.

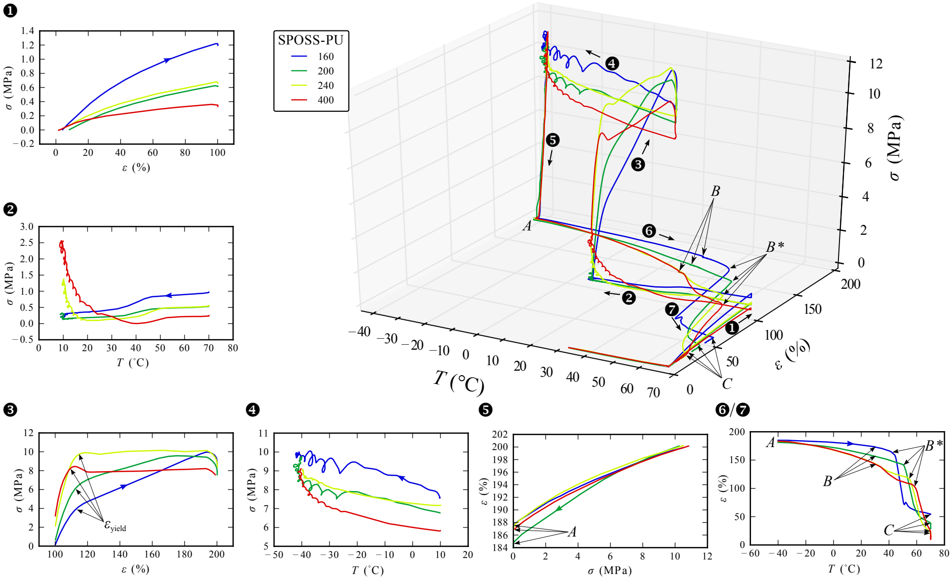

Figure 5.1.: Three-dimensional stress-strain-temperature diagram of the first thermomechanical cycle during triple-shape testing of four SPOSS-PUs. The small plots at the left and bottom side are two-dimensional projections of the individual steps for the same dataset. The thermomechanical cycle included ❶. deformation at 70 °C to 100%, ❷. cooling to 10 °C, ❸. deformation to 200%, ❹. cooling to −40 °C and ❺. unloading. Successive shape recoveries were triggered by heating ❻. to 30 °C and ❼. to 70 °C.

5.1.1. Triple-shape programming

Initially, the SPOSS-PUs were heated from 23 to 70 °C. In step ❶ and ❷ of the thermomechanical cycle, deformation of 100% and cooling to 10 °C transformed the rubbery specimens from their permanent to the first temporary shape. These steps were identical to the dual-shape testing procedure as described in Section 4. The stress-temperature diagram of step ❷ in Figure 5.1 clearly shows the three different phases of shape fixing for the four SPOSS-PUs. Initial cooling induced a temperature-proportional decrease in stress, attributed to a decreasing stress from entropy elasticity (Section 2.3.2). On further cooling, PCL crystallization resulted in a pronounced stress decrease. The final stress increase arose from a measurement artifact (Section 3.2.4).

At 10 °C, a second deformation up to a strain of 200% was applied. The stress-strain diagram of that second deformation (step ❸) shows the characteristic features of a ductile polymer, for

Table 5.1.: Young's moduli E_1 and E_2 of first and second tensile deformation at 70 and 10 °C, respectively, and tensile strain at yield ε_{yield} (second tensile deformation) for SPOSS-PUs in the first measurement cycle ($N = 1$) and cycles-averaged ($N = 2 - 5$). No yielding is observed in specimens of SPOSS-PU 160 and 200 in cyles $N = 3 - 5$.

	E_1 (MPa)		E_2 (MPa)		ε_{yield} (%)	
SPOSS-PU	$N = 1$	$N = 2 - 5$	$N = 1$	$N = 2 - 5$	$N = 1$	$N = 2 - 5$
160	2.1 ± 0.1	1.4 ± 0.1	42 ± 3	48 ± 4	112 ± 3	n.a.
200	1.2 ± 0.1	0.7 ± 0.1	58 ± 3	59 ± 4	110 ± 3	n.a.
240	1.3 ± 0.1	0.7 ± 0.1	100 ± 3	89 ± 2	116 ± 3	121 ± 0.3
400	0.8 ± 0.1	0.3 ± 0.1	113 ± 3	109 ± 2	109 ± 3	107 ± 0.2

instance yielding. Such behavior is typical for semicrystalline polymers (compare Section 2.3.2) and contrasts the previously observed rubbery stress-strain behavior at 70 °C. During initial deformation, the stress-strain diagram shows a high initial gradient (Young's modulus) and strong stress increase. Compared to the Young's moduli E_1 during the first deformation at 70 °C, Young's moduli E_2 at 10 °C increased by a factor > 20 (Table 5.1), documenting the high stiffness introduced by the semicrystalline PCL domains. Furthermore, the Young's moduli E_2 increased with higher PCL chain length, which contrasts the composition-dependent tendency of E_1 during the deformation of the rubbery SPOSS-PU. Obviously, the higher PCL content and the arising degree of PCL crystallinity enhanced the effective cross-link density at 10 °C and thereby increased the SPOSS-PU stiffness at higher amount of PCL content.

In addition, a yield point between 109 and 116% was observed in all SPOSS-PUs, apparent by a change in the slope of the stress-strain curve in SPOSS-PU 160 and 200. In SPOSS-PU 240 and 400, the yield point was even followed by a slight decrease of the nominal stress, indicating the formation of a neck. With the strain increasing further, the stress trajectories of SPOSS-PU 240 and 400 formed plateaus, which were associated with neck propagation.

Indeed, a neck became evident by a strong, local decrease of the specimens' cross-section and high opacity of the affected region. Necking is a well-known phenomenon in semicrys-

Table 5.2.: Strain ε_A of shape A for SPOSS-PUs in the first measurement cycle ($N = 1$) and cycles-averaged parameters ($N = 2 - 5$) at −40 °C.

	ε_A (%)	
SPOSS-PU	$N = 1$	$N = 2 - 5$
160	185 ± 3	182 ± 0.5
200	184 ± 3	182 ± 0.3
240	181 ± 3	182 ± 0.2
400	184 ± 3	184 ± 0.1

talline polymers, including PCL homopolymer[184] and composites of poly(L-lactic acid)/PCL at PCL contents of > 40%.[185] In SPOSS-PU 160 and 200 necking was not observed.

The triple-shape programming procedure was completed by cooling the specimens below the glass transition to −40 °C (step ❹). Residual stresses of ~ 11 MPa from cooling were reduced to zero. As a result, a second temporary shape – shapes *A* (step ❺) – was established at strains between 181 and 185 % (Table 5.2), almost independent of the number of cycles.

5.1.2. Triple-shape recovery

After the triple-shape programming procedure was completed, recovery of the SPOSS-PUs was quantified in two different scenarios. In scenario *S1*, successive heating of the two-fold programmed SPOSS-PUs to 30 and 70 °C induced two distinct shape recoveries. Figure 5.2a (black curves) shows strain and temperature *vs.* time for the exemplarily chosen SPOSS-PU 200.

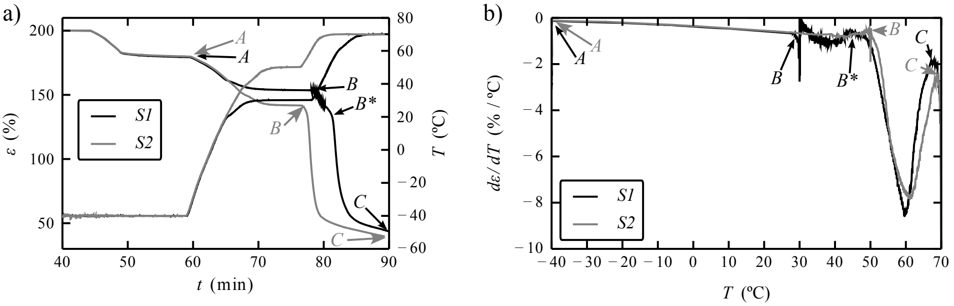

Figure 5.2.: Recovery behavior of SPOSS-PU 200 during heating either from −40 to 70 °C with an intermediate holding temperature of either 30 °C (scenario *S1*, black line) or 50 °C (scenario *S2*, grey line). Plotted are a) strain and temperature *vs.* time and b) strain–temperature derivative *vs.* temperature for both scenarios. Vertical deviations of the strain-temperature derivative at 30 and 50 °C originate from temperature differentiation at temperature holding times ($\lim_{dT \to 0} (\frac{d\varepsilon}{dT}) = \infty$).

In course of the first heating (step ❻), slight strain releases between 13 and 41% (cycle $N = 1$) transformed the SPOSS-PU specimens from two-fold fixed shape *A* to temporary shape *B*. The second heating in step ❼ induced recovery of shape *C*, with the strain changes even exceeding the associated deformation of 100% applied in course of shape programming. The high strain recovery values suggest, that part of the second deformation has been recovered in course of the second heating step. In other words, a fraction of the second deformation – fixed by cooling below the glass transition – was released by heating the SPOSS-PUs above the PCL melting transition.

In a progressive approach, another recovery scenario (*S2*, gray curve) probed the influence of testing temperatures on the shape recovery profile. This time, the specimen was heated from −40 to 50 °C in step ❻ and from 50 to 70 °C in the adjacent step ❼. The increased intermediate temperature allowed to test whether a stable shape B could be found above the previously tested temperature. In addition, more balanced recovery strains for the two subsequent transitions were expected. Indeed, the recovered strain in the first heating step significantly increased and a stable shape B was detected at 50 °C, indicating that stable shapes can be found in a broader temperature interval below the melting transition of PCL chains (Section 4.1.1).

The stain-temperature derivatives depicted in Figure 5.2b give a more detailed picture of shape recovery scenarios *S1* and *S2*. The associated curves clearly show two regions. While heating from −40 to ∼ 50 °C, low recovery rates of less than $1\,\%\,\mathrm{K}^{-1}$ illustrated a gradual, yet slowly progressive recovery. Similarly, initial heating from 30 °C in scenario *S1* yielded the same low recovery rate, suggesting the same underlying recovery mechanism. During heating, the thermal and accordingly the inner energy of the semicrystalline SPOSS-PU specimens continuously increased, enhancing the micro-brownian motion of PCL chains. Thereby, PCL soft segment chains gradually gained the abililty to recover their initial shape. However, PCL crystallites still acted as physical cross-links and thus constrained the microscopic movements of PCL chains inside the SPOSS-PU matrix, resulting in a rather small contraction rate.

In turn, the strain-temperature rate accelerated by a factor of 10, when the vicinity of the PCL melting transition was reached, as demonstrated by a pronounced, single peak. Here, the vanishing physical cross-links from PCL crystallites enabled efficient recovery of the specimen's permanent shape. Accordingly, the characteristics of the associated (phase) transitions were completely different. A broad glass transition enabled gradual shape recovery at a low rate, while a pronounced, narrow melting transition drove the most distinct shape change.

To make an appropriate assignment of the recovered strains to the respective transitions, the onset temperatures of the melting-induced recovery were determined. Initial melting-induced recovery was indicated by a sharp decrease in the slope of the strain-temperature diagram and the onset temperature of the melting transition parabola in the strain-temperature derivatives $T_{r,on}$. The endmost shape identified before PCL melting was termed B^*. In accordance with B^*, the recovered strains for heating above the glass transition $\varepsilon_{A\rightarrow B^*}$ and the melting transition $\varepsilon_{B^*\rightarrow C}$ were calculated, yielding rather plausible strain recoveries (Table 5.3).

In good agreement with the dual-shape properties, the strain change $B^* \rightarrow C$ was most pronounced at high cross-link density (SPOSS-PU 160), when it was heated above the PCL glass transition temperature. However, it still exceeded the applied strain of 100%, suggesting that

Table 5.3.: Triple-shape recovery properties of SPOSS-PUs, including strain recoveries $\varepsilon_{A\rightarrow B^*}$ and $\varepsilon_{B^*\rightarrow C}$ and the recovery onset temperature $T_{r,on}$ of the second contraction. For reference, strain releases from dual-shape measurements ε_{dual} are supplied.

	$\varepsilon_{A\rightarrow B^*}$ (%)		$\varepsilon_{B^*\rightarrow C}$ (%)		$T_{r,on}$ (°C)		ε_{dual} (%)
SPOSS-PU	$N = 1$	$N = 2 - 5$	$N = 1$	$N = 2 - 5$	$N = 1$	$N = 2 - 5$	$N = 2 - 5$
160	25 ± 4	34 ± 4	131 ± 4	105 ± 4	44 ± 0.6	43 ± 0.8	91 ± 1
200	17 ± 4	30 ± 6	146 ± 4	125 ± 1	45 ± 0.6	45 ± 0.5	88 ± 1
240	63 ± 4	55 ± 1	103 ± 4	103 ± 4	48 ± 0.6	47 ± 0.7	89 ± 1
400	76 ± 4	73 ± 1	98 ± 4	98 ± 1	55 ± 0.6	55 ± 0.2	75 ± 6

part of the second deformation was recovered in this heating step. In contrast, the shape changes $A \rightarrow B^*$ during the first heating in SPOSS-PU 160 were relatively small. More balanced strain recovery of $A \rightarrow B^*$ and $B^* \rightarrow C$ was found at increasing PCL chain length. SPOSS-PU 400 showed the highest strain recovery $\varepsilon_{A\rightarrow B^*}$ within the SPOSS-PU series. As a possible cause, irreversible deformation particularly at increased POSS content is considered.

5.1.3. Thermoreversible necking

Table 5.4.: Residual strain $\varepsilon_{r,dual}$ and $\varepsilon_{r,triple}$ after recovery of the permanent shape for SPOSS-PUs in dual- and triple-shape measurements, respectively.

	$\varepsilon_{r,dual}$ (%)	$\varepsilon_{r,triple}$ (%)
SPOSS-PU	$N = 2 - 5$	$N = 2 - 5$
160	9 ± 2	43 ± 4
200	12 ± 1	27 ± 1
240	11 ± 1	24 ± 4
400	25 ± 6	13 ± 1

Additional information regarding irreversible deformation during the second thermomechanical programming was deduced from comparison of the residual strains after cycling with the ones observed in dual-shape measurements (Table 5.4). In that case, residual strains increased with higher PCL chain length due to the occurrence of stress relaxation (compare Chapter 4). The same mechanism should have equally impacted the triple-shape measurements, since their first programming procedure was equivalent to programming in dual-shape measurements. In addition, irreversible deformation from the second programming procedure was expected to increase the residual strain in triple-shape measurements and should be represented by the difference of the residual strains in dual- and triple-shape measurements, $\varepsilon_{r,triple}$ and $\varepsilon_{r,dual}$.

The highest difference of $\varepsilon_{r,triple}$ and $\varepsilon_{r,dual}$ was found at low PCL chain length (SPOSS-PU 160). At decreased PCL chain length, *e.g.* for SPOSS-PU 400, there was no considerable difference (the negative difference is not meaningful). The results indicate that irreversible deformation during the second shape programming was most pronounced at high POSS content and short PCL chains. Such a trend may possibly originate from the deformation step ❸ of the thermomechanical pretreatment, where the shorter PCL chains reach a state of full chain extension earlier than the longer ones. Further elongation without structural damage cannot be achieved. Consequently, the probability that SPOSS-PU specimens suffer from intermolecular bond breakage in hard- or soft segments is most pronounced at low PCL chain length.

In contrast, higher PCL chain length obviously enabled SPOSS-PU 400 to respond more flexible to the low-temperature deformation. Even more, in this case the formation of a neck was found, which is commonly considered irreversible.[186] Necking is observed in amorphous and semicrystalline polymers and is associated with molecular rearrangements of polymer chains between the cross-links.[100] However, necking may also support extraordinary high deformations in amorphous polymer-clay nanocomposites,[187] which were able to recover deformations of up to 1800%.

Here, a neck formed during cold-drawing of the semicrystalline SPOSS-PUs. Probably, the necking process led to a microscopical reordering and increased orientation of the PCL crystallites. In any case, a visual impression of the neck and its thermally-induced recovery for SPOSS-PU 400 is depicted in Figure 5.3. The photos clearly illustrate the presence of a neck in the two-fold programmed shape *A*, apparent by a significant, local decrease of the specimens cross-section and high opacity. With heating, the neck boundaries propagated inwards (left part of Figure 5.3). Thereby, the opacity faded and the neck completely disappeared (mid of Figure 5.3), recovering the intermediate shape *B*. From that point onwards, the melting-induced shape recovery started, visible as a highly transparent region. A transparent spot developed firstly in the middle of the

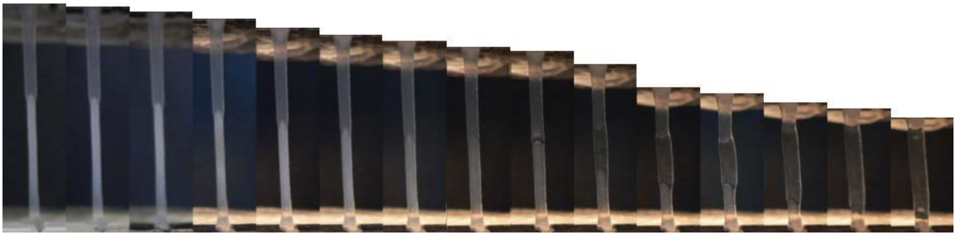

Figure 5.3.: Photo series showing strain recovery in SPOSS-PU 400, while heating from −40 (left) to 70 °C (right). An opaque appearance of the lower part of the specimen at low temperatures marks the necked region.

specimen and propagated outward, until the complete SPOSS-PU specimen was transparent and rubbery, having recovered its permanent shape C.

Obviously, the formation of a neck was a quasi-plastic process, which could be almost completely reversed by heating above the melting transition temperature. Even when shape programming was repeated for five times, each time accompanied by necking, the recovery process stayed almost unchanged. This point is impressively demonstrated by the high cyclic reproducibility of the thermomechanical cycles in multi-cycle measurements of SPOSS-PU 400 (Figure 5.4a and Table 5.3).

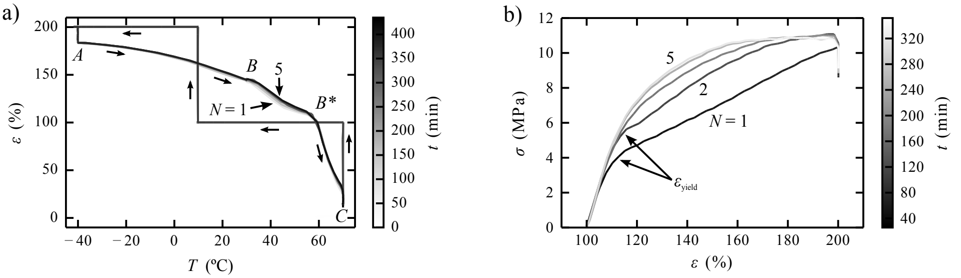

Figure 5.4.: Cyclic behavior of a) SPOSS-PU 400 and b) SPOSS-PU 160 for $N = 5$ cycles. a) Strain-temperature diagram for SPOSS-PU 400. Small cyclic deviations were only observed between the shapes B and B^* (inset). b) Stress-strain behavior of SPOSS-PU 160 during the second tensile deformation (step ❸) at 10 °C.

In SPOSS-PU 400, the strain-temperature curves of the different cycles showed, that the thermomechanical behavior was almost perfectly repeated during the five cycles. Marginal cyclic deviations were only detected in the temperature range between 30 and 55 °C. In contrast, strong cyclic changes in the recovered strains of the first and the following cycles were observed at lower PCL content (SPOSS-PU 160), in particular for $\varepsilon_{B^*\rightarrow C}$. This was due to a cyclic increase in the irreversible deformation. Here, the stress-strain relation of the second deformation to 200% indicates a progressive cyclic hardening (Figure 5.4b). A yield point was observed in cycle one and two. It shifted to increased stress and strain with cycling, until it finally merged into a continuative stress-strain curve, which did not exhibit a yield point. The cyclic strain hardening, *i.e.* the steady increase of the area below the curve – equivalent to the applied work – suggested an advancing alteration of the internal SPOSS-PU structure. Probably, each deformation led to further breakage of intermolecular bonds.

5.2. Multi-shape Properties

The gradual recovery behavior of SPOSS-PUs below the PCL melting transition temperature and the ability to maintain a shape B at 30 °C or a shape B^* between 43 and 55 °C were a motivation to test whether SPOSS-PU has multi-shape properties. In an exemplary CTM, interruption and continuation of the strain recovery process was carried out by applying temperature holding times of 5 min at various temperatures $T < T_m$(PCL) to an identically programmed SPOSS-PU 400, which was identically programmed as for common triple-shape measurements (Figure 5.5).

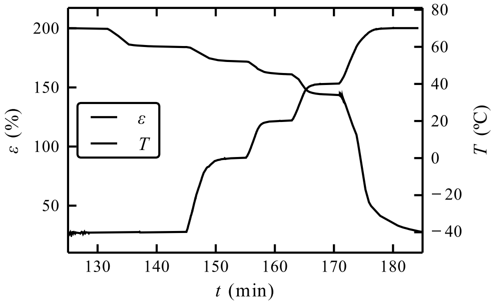

Figure 5.5.: Strain-temperature diagram showing the thermomechanical response of SPOSS-PU 400 to staged heating from −40 to 0, 20, 40 and finally 70 °C.

As a result, the shapes were found at each tested temperature, *i.e.* stable strains formed at plateaus of 184% (−40 °C), 173% (0 °C), 162% (20 °C), 148% (40 °C) and 28% (70 °C). An additional temporary shape could have been observed up to ∼ 55 °C, as suggested by a sharp decrease of the storage modulus at that temperature. However, at least three distinctively different shapes were associated with heating up to the onset of the PCL melting temperature, fixed by cooling below a single transition. Similarly, in networks from PCL and poly(cyclohexyl methacrylate) (PCHMA), a single deformation and shape fixing step allowed for two separate shape recovery steps.[139] However, in their case two phase transitions, the PCL melting and the PCMA glass transition, were employed for shape fixing and recovery. Here, heating above a single transition triggered several shape recovery steps, with the final heating above the melting transition yielding a last one. Similar observations have been made by Xie[116] in ionomeric perfluorosulfonic acid (Nafion®), who found that a broad glass transition allows several shape fixing and recovery steps.

5.3. Conclusions

The four programmed SPOSS-PUs exhibited distinct triple-shape behavior. In each case, heating above the glass transition temperature induced a first recovery step from two-fold programmed shape A to one-fold programmed shape B, while heating above the melting transition temperature triggered recovery of the permanent shape C.

The recovery characteristics of the first and second recovery process were strongly dependent on the underlying phase transition. Employment of the glass transition allowed to gradually recover, interrupt and resume the shape recovery process at any temperature below the PCL melting transition. A modified measurement even exemplified, that the number and magnitude of shape changes can be influenced by properly selecting additional holding temperatures. That way, a step-by-step release of strain could be achieved between the first and the second temporary shape, yielding multi-shape behavior.

A neck, which formed during deformation of the semicrystalline SPOSS-PUs with higher PCL content was almost perfectly thermoreversible. Moreover, the compositions, which showed necking even exhibited higher recovery strains when heated above the glass transition temperature compared to the ones of lower PCL chain length. Accordingly, the modification of the PCL network chain length turned out to be determinant for the triple-shape properties of these SMPs. Finally, heating above the PCL melting transition recovered the biggest portion of strain, including strain that was not recovered in the course of heating above the glass transition. Here, the trend observed in the dual-shape measurements of SPOSS-PUs was verified: The higher POSS content supported the most pronounced shape recovery, when heated above the melting transition.

6. PEUs, their Shape Memory and Actuation Behavior[d]

The basic properties as well as the shape memory and actuation behavior of a series of PEU block copolymers with various PBA soft segment contents were investigated. In a first step, swelling experiments determined basic network properties, such as the cross-link density and the PBA chain length. The thermal properties, in particular the PBA phase transitions, were then studied using DSC. In addition, DSC was conducted to study the PBA melting transition after various crystallization and storage conditions. WAXS measurements resolved the associated crystalline structures and gave information regarding the degree of crystallinity. The mechanical and viscoelastic properties of the PEUs were studied in DMA and tensile tests at 23 and 60 °C.

For shape memory measurements, the PBA soft segment crystallization and melting transitions were employed for shape fixing and recovery, respectively. In addition, the influences of the crystallization and storage conditions on the respective crystalline structures and thereby on the shape memory properties were examined. Finally, the PBA crystallization and melting transition were deployed to enable PEU actuation under isotonic conditions.

6.1. Characterization of PEUs

6.1.1. Network structures

In a first attempt, the effective network structures of three phase-segregated PEUs were studied by swelling experiments. To avoid interference from crystalline PBA cross-links, swelling experiments were conducted at 60 °C, where the PBA soft segment is fully amorphous (the thermal properties of the PEUs are discussed in detail below). Hence, at that temperature the degree of physical cross-linking is solely provided by hard segment domains. During pretests, ethyl acetate turned out as an appropriate swelling agent and was therefore selected. Table 6.1 provides an overview on the main experimental results.

First of all, the density of the PEUs showed a composition-dependent trend. The PEU hard and soft segment constituents had a lower density $\rho_{PBA} = 1.019\,\mathrm{g\,cm^{-3}}$ (at 25 °C)[188] and higher

---

[d] © 2012 Wiley. Used with permission from Ref. 4. (List of Publications).

Table 6.1.: Network quantities determined from swelling behavior of PEU with high (h), medium (m) and low (l) PBA soft segment content in ethyl acetate at 60 °C: polymer density ρ, degree of swelling Q, gel content G, average PBA molecular weight M_w, number of PBA repeating units $R.U.$ and cross-link density ν_c.

	ρ (g cm^{-3})	Q	G (%)	M_w (g mol^{-1})	$R.U.$	ν_c (10^{-4} mol cm^{-3})
PEU-h(ssc)	1.190 ± 0.001	4.02 ± 0.02	97.9 ± 0.1	4120 ± 50	21.1 ± 0.2	2.9 ± 0.1
PEU-m(ssc)	1.193 ± 0.005	3.08 ± 0.03	98.8 ± 0.1	2090 ± 90	10.4 ± 0.4	5.7 ± 0.2
PEU-l(ssc)	1.197 ± 0.002	2.61 ± 0.02	99.0 ± 0.1	1330 ± 10	6.6 ± 0.1	9.0 ± 0.1

density $\rho_{MDI} = 1.230\,\mathrm{g\,cm^{-3}}$, respectively. Accordingly, the higher PEU density ρ suggests an increased amount of polyurethane hard segment and a decreased amount of PBA soft segment content in the PEU series. In line with their highest (h), medium (m) and lowest (l) soft segment content, the PEUs were termed "PEU-h(ssc)", "PEU-m(ssc)" and "PEU-l(ssc)". A higher degree of swelling Q was observed at growing soft segment content, implying that the PBA soft segment dominated the swelling behavior. Gel contents G of almost 100% indicated a mostly complete reaction of PBA with the MDI chain extended by 1,4-butanediol. In particular, slightly rising gel content with increasing hard segment content suggests the formation of a stable network structure from phase segregation. PBA mean molecular weights between 4120 and 1330 g mol^{-1} were quantified, corresponding to statistical numbers of PBA repeating units between 21.1 and 6.6 with the higher chain length at increased soft segment content.

6.1.2. Thermal properties

In a next step, the thermal properties of the PEU block copolymers were studied by means of DSC (Figure 6.1, Table 6.2). The PBA melting peaks were found in between 42 and 47 °C (Figure 6.1a).

Table 6.2.: PBA melting and crystallization enthalpies (ΔH_m, ΔH_c) and peak temperatures (T_m, T_c) of PEU-h(ssc), PEU-m(ssc) and PEU-l(ssc) from DSC during the first heating, (1^{st} h.), the first cooling (1^{st} c.) and the second heating run (2^{nd} h.).

	ΔH_m (J g^{-1})		ΔH_c (J g^{-1})	T_m (°C)		T_c (°C)
	1^{st} h.	2^{nd} h.	1^{st} c.	1^{st} h.	2^{nd} h.	1^{st} c.
PEU-h(ssc)	27.6	28.3	−27.3	46.7	44.7	8.0
PEU-m(ssc)	21.5	21.1	−19.5	44.3	40.5	−1.5
PEU-l(ssc)	18.4	18.5	−12.1	42.3	39.6	−3.4

In line with observations of a series of similar poly(ester urethanes),[189] the growing soft segment chain length was connected to increasing PBA melting and crystallization enthalpies. An associated increase in degree of crystallinity was likely due to the higher segmental mobility and increased degree of conformational freedom at higher PBA chain length. Even more, a higher melting temperature suggests an increase in mean crystallite sizes.

In turn, a more confining environment from increased hard segment content respective physical cross-link density constricted molecular mobility and thereby reduced the degree of PEU crystallinity.

In good agreement with the ‘free volume’ theory, which describes the general dependence of the glass transition temperature on polymer chain length,[95,190] the PEU glass transition temperature increased from -49 to $-47\,°\mathrm{C}$ with growing PBA soft segment chain length (Figure 6.1b).

Despite of showing single, Gaussian-shaped PBA crystallization signals during cooling, the second heating run exhibited a broad signal with a shoulder at lower temperature in every single case (Figure 6.1c). Peak deconvolution of that asymmetric signals illustrates double melting behavior for each PEU in the series (Table 6.3) and suggests the presence of two crystalline forms.

Polymorphism in aliphatic polymers is a well-known phenomenon.[96] PBA homopolymer ($M_w = 40\,000\,\mathrm{g\,mol^{-1}}$) crystallizes in at least two different crystal forms, either in a monoclinic system (α crystal form) or in an

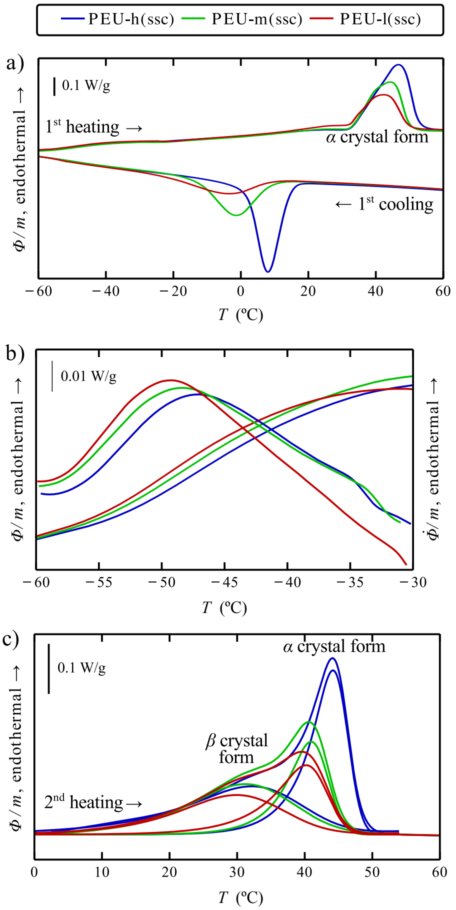

Figure 6.1.: DSC thermograms of a) first heating and cooling run, b) PBA glass transition during second heating (solid lines) and the associated time derivatives (dashed lines) and c) deconvolved PBA melting during second heating (solid, dotted and dashed lines) of PEU-h(ssc), PEU-m(ssc) and PEU-l(ssc).

Table 6.3.: Melting enthalpies ΔH and peak temperatures T_m for PBA α and β crystal form as derived from peak deconvolution of PBA melting observed in the second heating run.

	ΔH (J g^{-1})		T_m (°C)	
	α	β	α	β
PEU-h(ssc)	14.9	13.3	46.1	37.8
PEU-m(ssc)	9.1	12.2	43.0	36.8
PEU-l(ssc)	8.9	9.6	42.8	34.7

orthorhombic system (β crystal form).[191,192] Crystallization at high cooling rates[98,193] as well as low-temperature-annealing[191] results in the PBA homopolymer preferentially developing a meta-stable β morphology. In contrast, when annealing at increased temperatures[191,194] or when applying strong deformations,[195] PBA is more likely to crystallize in the thermodynamically stable α form. In the deconvolved thermograms, a main signal between 40 and 44 °C and a lower signal at about 35 °C were identified. In line with the assignment made for PBA homopolymer by Gan *et al.*,[191] the lower and higher temperature signals were assigned to melting of the PBA β and α crystal form, respectively.

To learn about the thermal stability of the PBA crystal forms, PEU-h(ssc) was selected for further DSC studies. In a first step, identical initial states were obtained by a thermal pretreatment, consisting in complete PBA melting and recrystallization. After annealing for various times at 25 °C, the PBA melting behavior was investigated in DSC. Figure 6.2 depicts the normalized heat flow of the first heating run.

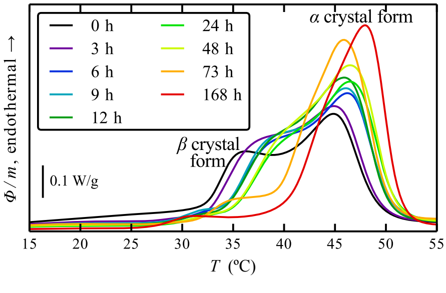

Figure 6.2.: DSC thermograms of the first heating run after PBA melting, recrystallization and room temperature annealing (PEU-h(ssc)) for various holding periods between 0 h and 1 week (168 h).

Again, the non-annealed sample exhibited the broad endothermal signal. When extending the room temperature annealing period, the lower temperature shoulder monotonously decreased and in parallel the high temperature signal increased, indicating a progressive shift of melting signals. This behavior illustrates the sensitivity of the PBA polymorphic mixture toward room temperature annealing. In greater detail, the lower temperature shoulder almost completely disappeared within one week (168 h) at 25 °C, while in the same period the higher temperature signal significantly increased. Accordingly, the PBA β crystallites must have been almost completely transformed into PBA α crystallites. Such behav
found that PBA β crystals are indeed transfor
thermal stability, apparently resulting in a PB
present case, the described endothermic signals d
that all three (untreated) PEUs were initially p
On first cooling, the single exothermic signal s
most likely due to the development of PBA β cr
during subsequent heating (Figure 6.1c) illustra

In a next step, the influence of the cooling
investigated with a focus on the resulting PB

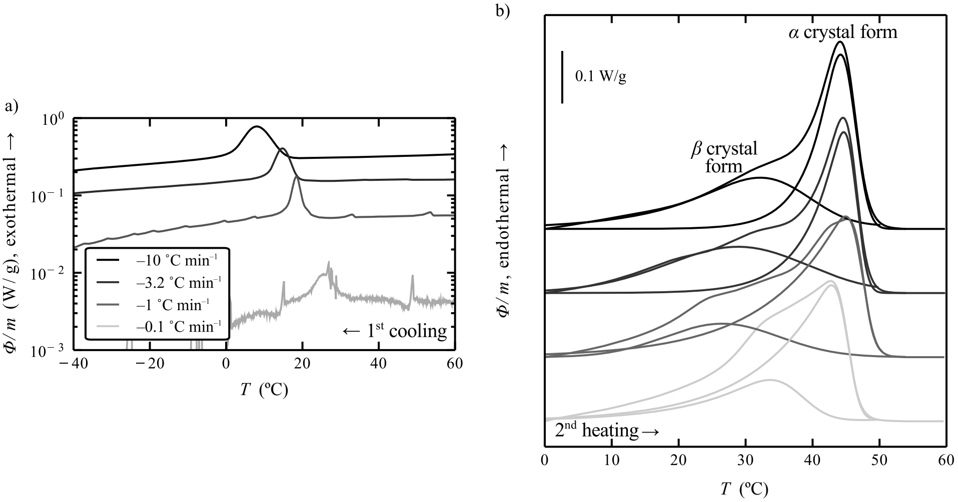

Figure 6.3.: DSC thermograms of a) PBA crystallization of PEU-h(ssc) in the first cooling run at various cooling rates and b) the following PBA melting in the second heating run. The dashed and dotted lines show the deconvolved melting signals, illustrating the contributions from the PBA β and α crystal forms.

h(ssc), crystallization at cooling rates between 10 and 0.1 K min^{-1} resulted in the adjacent broad melting signal on heating. Peak deconvolution shows that melting of an increasing fraction of α crystals and a parallel decrease in the fraction of β crystals occurred when lowering the cooling rate during crystallization. The observed behavior was in good agreement with polymorphic studies after non-isothermal crystallization of PBA homopolymer ($M_w(\text{PBA}) = 12\,000\,\text{g}\,\text{mol}^{-1}$) by Kai *et al.*[193]

6.1.3. Crystalline structure

To verify the above made assignment of the polymorphic PBA phases, WAXS measurements were conducted on untreated and thermally pretreated PEUs, *i.e.* the PBA soft segment was molten and recrystallized (compare state in Figure 6.2, 0 h annealing). The radially integrated WAXS diffractograms for the three PEUs are depicted in Figure 6.4.

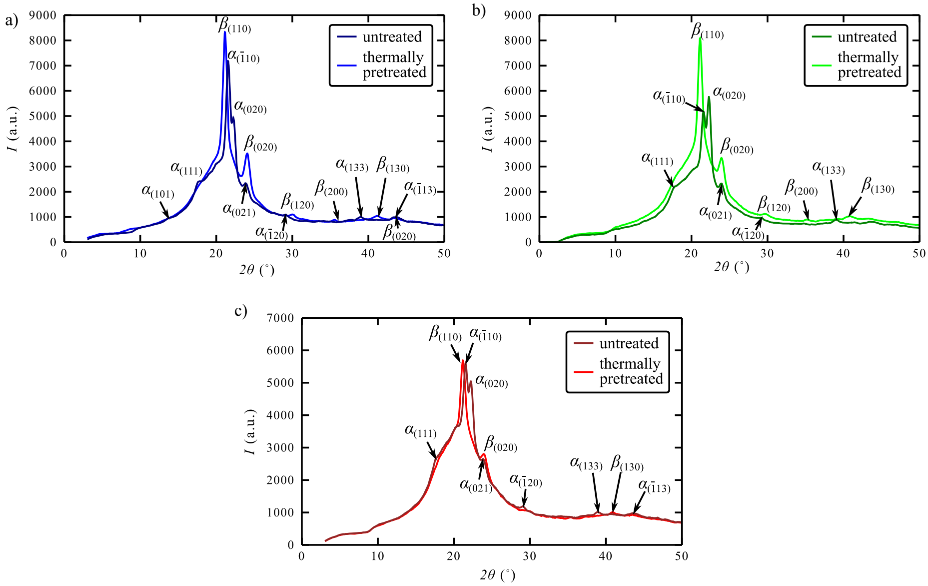

Figure 6.4.: WAXS diffractograms of untreated and thermally pretreated a) PEU-h(ssc), b) PEU-m(ssc) and c) PEU-l(ssc) with reflexes assigned to the PBA α and β crystal form. Thermal pretreatment consisted in PBA melting and crystallization.

In any case, a broad halo as the diffractograms base indicated the presence of an amorphous phase. Superimposed peaks were either assigned to the PBA α or β crystal form. As expected from the calorimetric measurements, the peak signals for untreated PEU (Figure 6.4, black lines) could be ascribed to the PBA α crystalline structure (monoclinic system, a = 6.73 Å, b = 7.94 Å, c = 14.20 Å, β = 45.5°).[191,195,196] In turn, reflexes after thermal pretreatment originated from the kinetically preferential β crystal form (orthorhombic system, a = 5.06 Å, b = 7.35 Å, c = 14.67 Å,[191] grey lines in Figure 6.4). In this case, no reflexes from the PBA α crystal form were detected. This finding supports the above made observation that under the given conditions, PBA in all three PEUs exclusively crystallized in the β crystal form, *e.g.* in the first DSC cooling run (Figure 6.1a). In consequence, a crystal-crystal ($\beta \rightarrow \alpha$ crystal) transformation must have taken place during the second heating run in the DSC measurements (Figure 6.1c). The same is true for DSC after room temperature annealing (Figure 6.2), because α crystal melting was apparent in all these thermograms. Hence, in the investigated block copolymers, the PBA crystallization and melting behavior was similar to that of PBA homopolymer. In addition, the PBA β melting behavior in PEU was also accompanied by a characteristic crystal-crystal transformation from the thermodynamically metastable β to the room temperature stable α morphology.[191] One in all, annealing of the PEUs at 23 °C resulted in the development of the PBA α crystal form, whereas thermal treatment represented a way to temporarily introduce β crystals.

In order to gain high precision diffractograms and determine the overall degree of PEU crystallinity at 23 °C, higher intensity synchrotron data (BESSY II) was collected for the untreated PEUs (Figure 6.5).

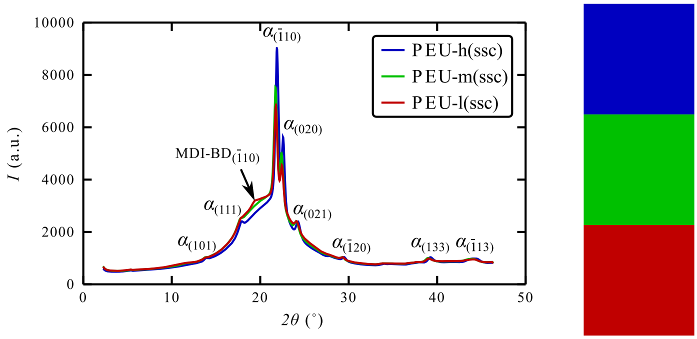

Figure 6.5.: High intensity synchrotron WAXS diffractograms of PEU-h(ssc), PEU-m(ssc) and PEU-l(ssc) measured at 23 °C. Almost all reflexes are assigned to the crystal lattice of the monoclinic PBA α morphology except for the one at $2\theta = 19.8°$ in PEU-l(ssc), which gives indication of the triclinic hard segment crystal structure (MDI-BD).

Accordingly, the degree of crystallinity, presumably composed of hard and soft segment crystallinity, decreased with the lower soft segment content. In detail, the total crystallinities were $\chi_c = 13.6\%$ (PEU-h(ssc)), 11.1% (PEU-m(ssc)) and 8.6% (PEU-l(ssc)). The same trend of increasing crystallinity with growing soft segment content has been found in block copolymers by Hojabri *et al.*[189] In addition, the diffractogram of PEU-l(ssc) exhibited a small signal at $2\theta = 19.8°$, which could neither be assigned to the α nor to the β crystal form. A similar signal at $2\theta = 19.7°$ has been observed in diffraction studies by Hwang *et al.*[197] on MDI-BD hard segment model compounds, ascribed in that publication to reflection (-106) of the triclinic unit cell ($a = 5.05\,\text{Å}$, $b = 4.67\,\text{Å}$, $c = 37.9\,\text{Å}$, $\alpha = 116°$, $\beta = 116°$, $\gamma = 83.5°$). Hence, PEU-l(ssc) obviously possessed a crystalline hard segment, in contrast to PEU-h(ssc) and -m(ssc). However, the observed signal ascribed to hard segment crystallinity was negligible, such that the observed PEU crystallinity was dominated by the soft segment. In case of PEU-h(ssc) and -m(ssc), the hard segment was expected to form glassy domains.

6.1.4. Mechanical properties

Untreated, semicrystalline and rubbery PEUs were investigated in uniaxial tensile tests at 23 and 60 °C. The results of the tests at 23 °C are shown in Table 6.4, the corresponding stress-strain diagrams are given in Figure 6.6.

Table 6.4.: Results from tensile testing at 23 °C on PEU tensile bars (strain rate = $0.5\,\%\,\text{s}^{-1}$, preload = 5 N), including Young's modulus E, tensile strain at break ε_B, tensile stress at break σ_B and fracture toughness k.

	E (MPa)	ε_B (%)	σ_B (MPa)	k (MJ m^{-3})
PEU-h(ssc)	39 ± 3	1927 ± 38	73 ± 3	63.5 ± 3.4
PEU-m(ssc)	40 ± 3	1811 ± 61	74 ± 5	62.0 ± 5.5
PEU-l(ssc)	47 ± 3	1707 ± 82	71 ± 4	57.5 ± 4.9

At low strains, growing hard segment content induced an increase in polymer stiffness as evident by the Young's modulus E. Even more, the three PEUs sustained tensile strains at break of more than 1600%. With growing soft segment content, the tensile strain at break increased; here highest amount of PBA yielded most pronounced fractions of both crystallizable (Figure 6.1a) and amorphous PBA segments is expected. The latter enables strong elongation due to high molecular mobility. The slightly increasing ultimate tensile strength and toughness with growing PBA content might be due to the increasing degree of soft segment crystallinity, as verified in the synchrotron WAXS measurements shown above.

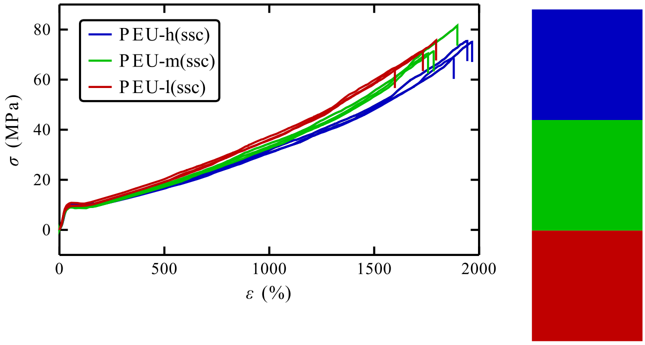

Figure 6.6.: Stress-strain diagram at 23 °C of PEU-h(ssc), PEU-m(ssc) and PEU-l(ssc) (strain rate = 0.5 % s^{-1}).

In the next step, the mechanical properties of the untreated PEUs were studied in tensile tests at 60 °C and thus above their PBA melting transitions (Table 6.5, Figure 6.7). Compared to room temperature deformation, the Young's moduli E at 60 °C decreased by more than one order of magnitude. However, the above described trend of increasing E with higher hard segment content stayed valid. The estimation of the cross-link density ν_c from the Young's moduli E (Table 6.5) according Formula 2.7 reflects an increasing ν_c at higher hard segment content, confirming the trend observed in the above described swelling experiments.

In the associated stress-strain derivatives of the considered PEUs, an inversion point indicated the onset of PBA deformation-induced crystallization (Figure 6.7). With increasing soft segment content, the PBA crystallization onset shifted toward higher strains (from 195 to 251%). Flory's 'Principles of Polymer Chemistry' gives a plausible explanation:[53] On elongation, a state close to full chain extension is earlier reached in polymer networks with lower chain length. Here,

Table 6.5.: Results from tensile testing at 60 °C on PEU tensile bars up to a strain of 800% (strain rate = 0.5 % s^{-1}), including Young's modulus E, strain and stress at PBA crystallization onset ($\varepsilon_{c,on}$ and $\sigma_{c,on}$) and cross-link density ν_c as calculated according Formula 2.7.

	E (MPa)	$\varepsilon_{c,on}$ (%)	$\sigma_{c,on}$ (MPa)	ν_c (10^4 mol cm^{-3})
PEU-h(ssc)	2.0 ± 0.1	251 ± 2	1.9 ± 0.1	2.4 ± 0.1
PEU-m(ssc)	2.8 ± 0.1	217 ± 2	2.6 ± 0.1	3.4 ± 0.1
PEU-l(ssc)	3.6 ± 0.1	195 ± 2	3.3 ± 0.1	4.3 ± 0.1

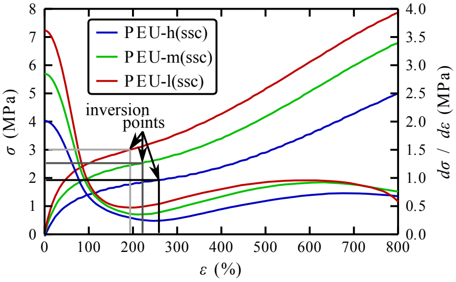

Figure 6.7.: Deformation diagram showing stress (solid line) and the corresponding stress-strain derivatives (dotted lines) *vs.* strain at 60 °C for PEU-h(ssc), PEU-m(ssc) and PEU-l(ssc) (strain rate = 0.5 % s^{-1}). The onset of deformation-induced PBA crystallization is indicated by the presence of inversion points.

deformation-induced crystallization sets in first, because the shorter soft segment chains are more susceptible to orientation than the longer ones.

The quantification of the mechanical properties of untreated PEUs was completed by DMA (Figure 6.8). Here, changes in slope of the storage modulus E' indicate two consecutive phase

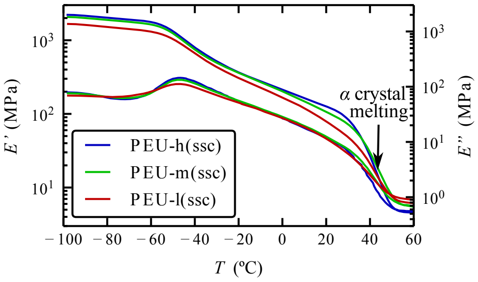

Figure 6.8.: DMA measurements showing the elastic modulus E' (solid lines) and loss modulus E'' (dotted lines) between −100 and 60 °C for PEU-h(ssc), PEU-m(ssc) and PEU-l(ssc) ($f = 1$ Hz).

changes for all three PEUs. These changes were ascribed to the PBA glass transition and PBA melting transition, starting at about −50 and 30 °C, respectively (Figure 6.8, solid lines). At deeper temperatures, slightly increased elastic moduli were favored by the higher PBA content, providing higher fractions of crystalline and glassy PBA domains in PEU-h(ssc) and PEU-m(ssc). In agreement with the calorimetric measurements,[189] the peak temperatures of the loss modulus E'', corresponding to T_g, were located at $\sim 47\,°\mathrm{C}$. Above the glass transition temperature, diminishing E' and E'' values indicated decreasing resistance toward deformation; the PEUs became progressively softer. Final heating above the soft segment melting transition (well above $30\,°\mathrm{C}$) yielded a strong decrease of the storage modulus. The PBA α crystal melting temperatures were located in between 37 and $40\,°\mathrm{C}$ in the PEU series, as determined by the inversion point of the storage modulus E'. As a final indication for shape memory testing, a decrease in the ratio of storage moduli from rubbery and semicrystalline state suggests that highest shape fixities may be observable at the highest soft segment content, due to the lowest associated ratios $^{E'(60\,°\mathrm{C})}/_{E'(23\,°\mathrm{C})}$ with values of 0.05 (PEU-h(ssc)), 0.07 (PEU-m(ssc)) and 0.10 (PEU-l(ssc)).

6.2. Thermomechanical Behavior

6.2.1. Shape memory properties

To investigate the influence of average PBA chain length on the shape memory characteristics of PEUs, a deformation strain of 100% was applied and fixed by cooling to $-20\,°\mathrm{C}$ (below T_c(PBA)). Recovery was triggered by heating to $60\,°\mathrm{C}$ (above T_m(PBA)). Figure 6.9 gives an overview of the stress, strain and temperature *vs.* time during shape programming for the three PEUs; the

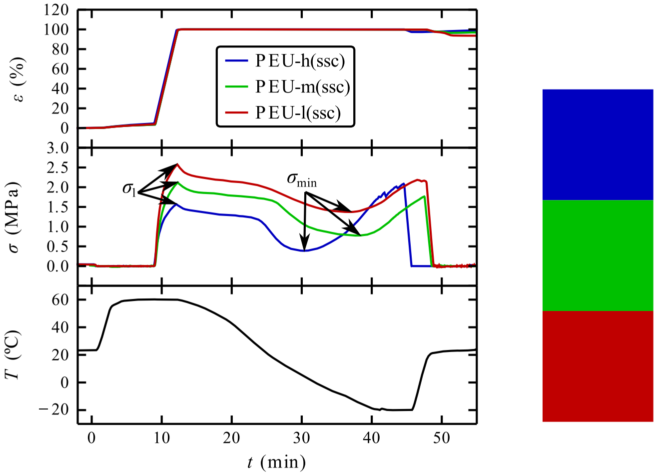

Figure 6.9.: The shape programming procedure showing the evolution of strain ε, stress σ and temperature T *vs.* time t for PEU-h(ssc), PEU-m(ssc) and PEU-l(ssc) specimens.

Table 6.6.: Parameters from the shape programming procedure, including loading stress σ_l, minimum stress during cooling σ_{min}, the ratio of loading to minimum stress $^{\sigma_{min}}/_{\sigma_l}$ and the strain after unloading ε_u as measure of shape fixity, given for the first cycle ($N = 1$).

	σ_l (MPa)	σ_{min} (MPa)	$^{\sigma_{min}}/_{\sigma_l}$	ε_u (%)
PEU-h(ssc)	1.5 ± 0.1	0.3 ± 0.1	0.20 ± 0.01	99 ± 1
PEU-m(ssc)	2.1 ± 0.1	0.8 ± 0.1	0.38 ± 0.01	96 ± 1
PEU-l(ssc)	2.6 ± 0.1	1.3 ± 0.1	0.50 ± 0.03	92 ± 1

main results are summarized in Table 6.6. In course of shape programming, elongation of 100% yielded the highest loading stress at highest hard segment content. This observation is consistent with the trend in tensile tests at 60 °C (Figure 6.7). Cooling the PEUs below the PBA crystallization transition temperature to −20 °C fixed the temporary shape. As evident by a stress decrease during cooling in Figure 6.9 and the ratios of minimum and loading stress $^{\sigma_{min}}/_{\sigma_l}$ (Table 6.6), PBA crystallization resulted in efficient stress reduction, most pronounced at increased soft segment content. This trend was expected from the DMA tests, in which a lower ratio $^{E'(60\,°C)}/_{E'(23\,°C)}$ was found for PEUs with high soft segment content (Figure 6.8). As a result, PEU-h(ssc) exhibited very good shape fixity with a permanent shape at a strain ε_u close to 100%, whereas systematically lower ε_u values were detected for the other two PEUs. A comparable decrease in shape fixity at growing hard segment content has also been observed in PEUs with crystallizable PCL soft segments.[21]

A more detailed description of the shape programming procedure is given by the stress-temperature derivatives of cooling, which are exemplarily shown for PEU-h(ssc) (Figure 6.10).

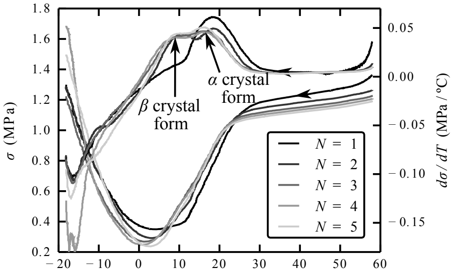

Figure 6.10.: Stress (solid lines) and the corresponding stress-temperature derivatives (dotted lines) *vs.* temperature during shape fixing for PEU-h(ssc) ($\varepsilon_m = 100\%$, $N = 1 - 5$).

For cycles $N = 2 - 5$, a broad peak consisting of two signals at 18 and 9 °C was observed. This observation contrasts the PBA crystallization behavior in DSC, which has only shown one crystallization signal (in the β crystal form). Here, the presence of stress and the resulting chain alignment may have supported additional crystallization in the α crystal form. Literature on structurally related PEU (Irogran® PS455-203) states that PBA deformation-induced crystallization occurs exclusively in the α phase.[198] Hence, in the present case the applied deformation may very well have supported the development of an α crystal form. Accordingly, the two signals were ascribed to crystallization in the PBA α and β crystal form, respectively.

To investigate the strain- and stress-related shape recovery characteristics of the three PEUs, the programmed specimens were heated from 23 to 60 °C (Figure 6.11). Shape recovery started with an immediate, slight decrease in strain at 23 °C (Figure 6.11a), indicating the melting of PBA β crystallites due to their lower thermal stability. As most apparent in the strain-temperature derivatives of PEU-h(ssc), a strong signal was assigned to PBA α crystal melting. At decreasing soft segment content, the signal shifted toward lower temperatures (Figure 6.11a).

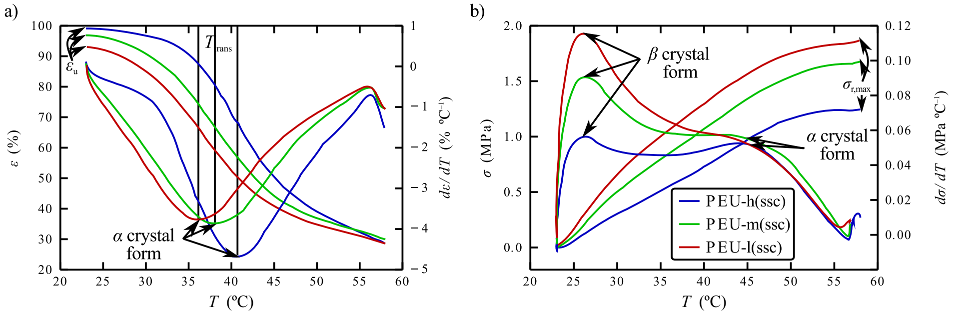

Figure 6.11.: Recovery behavior of programmed PEU-h(ssc), PEU-m(ssc) and PEU-l(ssc) specimens under a) free strain and b) fixed strain recovery conditions. Depicted are the evolution in strain and stress above temperature and the respective strain- and stress-temperature derivatives (dotted lines) for cycle $N = 1$.

Under fixed strain recovery conditions, the PEUs again instantaneously responded to heating at around 23 °C. However, here the stress instantaneously increased at a high rate, as apparent by a maximum in the stress-temperature derivative at about 27 °C (Figure 6.11b). In addition, the second melting signal peaked at around 43 °C. With the previous findings in mind, the lower temperature signal was again ascribed to PBA β crystal melting, which occurred prior to α crystal melting (second melting signal). One in all, the stress recovery behavior was highly sensitive to the crystalline polymorphic mixture of the PBA β and α crystal form.

Finally, Table 6.7 summarizes the parameters of strain and stress recovery. At growing soft

Table 6.7.: Influence of PEU composition on free strain recovery ($\varepsilon_u - \varepsilon_p$), the associated transition temperature T_{trans} and the maximum recovery stress $\sigma_{r,max}$. All parameters are given for the first cycle ($N = 1$) and cycle-averaged ($N = 2 - 5$)
.

	$\varepsilon_u - \varepsilon_p$ (%)		T_{trans} (°C)		$\sigma_{r,max}$ (MPa)	
	$N = 1$	$N = 2 - 5$	$N = 1$	$N = 2 - 5$	$N = 1$	$N = 2 - 5$
PEU-h(ssc)	79 ± 1	73 ± 1	41 ± 1	41 ± 1	1.3 ± 0.1	1.2 ± 0.1
PEU-m(ssc)	76 ± 1	71 ± 1	38 ± 1	39 ± 1	1.7 ± 0.1	1.6 ± 0.1
PEU-l(ssc)	70 ± 1	69 ± 1	36 ± 1	36 ± 1	1.9 ± 0.1	1.8 ± 0.1

segment content, higher strain recoveries $\varepsilon_u - \varepsilon_p$ were detected. On the contrary, the maximum recovery stresses $\sigma_{r,max}$ increased at higher hard segment content. Both trends may be explainable by the length of the soft segment chains. In course of shape programming, the shorter chains approach a state of full chain extension earlier than the longer ones, so that a transfer of stress onto the hard segments led to increased stresses at lower chain length. According to literature, dichroic studies on similar PEUs exposed to deformation and subsequent stress release show a persistent orientation of hard segments.[199–201] In contrast, the polyester soft segments fully reverse their anisotropy on stress release. In the present case, the same behavior may have led to deformation of the hard segment domains, which is considered irreversible under the given thermomechanical conditions ($T_{m,PU} \sim 190\,°\mathrm{C}$).[73] Consequently, reduced recovery strains were detected in PEU of higher hard segment content.

With proceeding cycling, a slight decrease of the shape memory parameters was evident when comparing the first with the following cycles ($N = 2 - 5$, Table 6.7). The general composition-dependent trends remained unchanged, as well as the transition temperatures.

To return to the influence of PBA polymorphism on the PEU behavior, the composition with the highest degree of crystallinity, PEU-h(ssc), was selected for further shape memory testing under fixed strain conditions. With the intention to allow for the crystal-crystal transformation to take place (compare DSC in Figure 6.2), programmed PEU-h(ssc) specimens were stored for extended holding times of 3 and 6 h at 23 °C. The diagram of the stress-temperature curves during recovery clearly shows an increasing recovery onset temperature from 23 to 29 °C, even for annealing times of only 3 h (Figure 6.12). Apparently, the thermal stability of the PBA crystal phase increased, indicating the occurrence of the $\alpha \rightarrow \beta$ transformation. Thereby, the polymorphic mixture determined the thermal stability of the temporary shape and the recovery onset temperature.

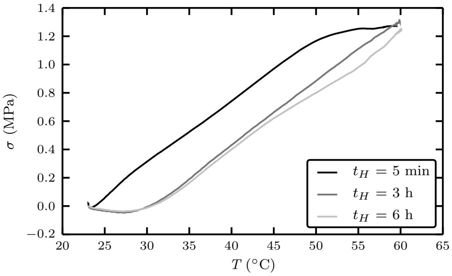

Figure 6.12.: Fixed strain recovery of PEU-h(ssc). Depicted are the stress *vs.* temperature after room temperature (23 °C) annealing for t_H of 5 min, 3 h and 6 h.

The considered transformation under stress was apparently less time intensive compared to the one observed in the DSC experiments (Figure 6.2). In other words, in a deformed, highly ordered networks the $\beta \rightarrow \alpha$ transition is more probable to occur compared to a stress-free isotropic arrangement of the polymer chains. As such, the extension of room temperature storage of programmed PEUs turned out to be an effective way to increase the crystalline PBA $^{\alpha}/_{\beta}$ ratio.

In further measurements the stress recovery behavior was quantified after altering the crystallization conditions. Therefore, the cooling rate during shape fixing was lowered from −5.5 to −2.0 and $-0.6\,\mathrm{K\,min^{-1}}$ and the subsequent recovery behavior investigated (Figure 6.13).

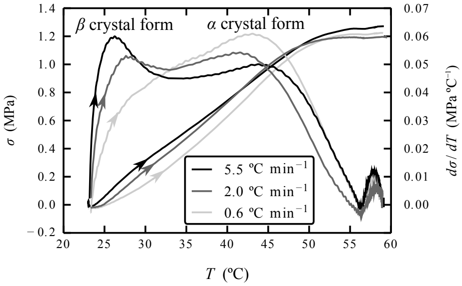

Figure 6.13.: Fixed strain recovery of PEU-h(ssc). Depicted are the stress (solid lines) and stress-temperature derivatives (dotted lines) *vs.* temperature after shape fixing at various cooling rates ($N = 1$).

In result, the onset stress recovery temperature slightly increased from 23 to 24 °C. An explicit picture is drawn by the strain-temperature derivative. Again, the stress increase was composed of two signals. A decrease of the lower temperature signal and at the same time an increase of the higher temperature signal exemplified the increasing amount of developing PBA α crystallites at lower cooling rates, which is in good agreement with the cooling-rate depending DSC measurements (Figure 6.3).

6.2.2. Comparison with SPOSS-PUs

The influence of the two various network architectures on the observed shape memory properties was deduced from comparison of the PEUs with the covalently cross-linked SPOSS-PUs. Both materials employed aliphatic polyester soft segment chains as a thermoresponsive component, with molecular weights of the same order of magnitude. As observed in DSC measurements, the melting and crystallization signals of SPOSS-PUs were much narrower. This primarily suggests a higher homogeneity of the soft segment chain length within the SPOSS-PUs and hints at a broader distribution of the crystalline and lamellar thickness in the PEUs. The well-defined structural SPOSS-PU networks were also associated with lower loss moduli $\tan(\delta)$ in DMA. Accordingly, the chemically cross-linked SPOSS-PUs were less susceptible to viscous flow than the physically cross-linked PEUs. The main structural difference of the investigated networks was given by the nature of their cross-links, which may or may not be subjected to deformation, and the width of the distribution of their network chain lengths.

The shape memory testing procedures were equivalent, with exception of the thermal parameters. In both cases, crystallization of the soft segment fixed the temporary shape, while shape recovery was triggered by soft segmental melting. For quantitative comparison of the shape memory properties, the (total) recovery ratios of PEUs were calculated: $R_{r,tot}(N = 2 - 5)$ was 74% (PEU-h(ssc)) and 71% (PEU-l(ssc)) and $R_r(N = 2 - 5) = 98\%$. Hence, the physically cross-linked PEU networks did not attain the performance of the SPOSS-PUs networks.

With respect to the shape fixity, the given value of ε_u (Table 6.6) in case of $\varepsilon_m = 100\%$ deformation is identical to the value of the shape fixity ratio R_f. Consequently, shape fixity ratios $R_f(N = 2 - 5)$ of PEUs were in between 92 and 99%. Accordingly, the distribution of their shape fixities was much broader than that of the SPOSS-PUs (Table 4.4). The fixity of PEU-h(ssc) slightly exceeded that of SPOSS-PUs, while the other two PEUs did not reach the shape fixity of any SPOSS-PU.

Qualitatively, the opposing trends of soft segment chain length on the shape recoverabilities can be explained by the following connection: PEUs with increased PBA soft segment chain length could be deformed to the strongest extent without transferring stress, *i.e.* inducing irreversible deformation to the hard segment domains. In contrast, SPOSS-PUs exhibited the most distinct shape memory properties at lower PCL soft segment chain length. Here, the covalent cross-links did not possess a spatial extension and the vast majority of covalent bonds must have remained perfectly intact, such that much lower irreversible deformation occurred (irreversible deformation at higher strains was observed in triple-shape measurements at low PCL chain length). In SPOSS-PUs, the main factor, which led to irreversible deformation was given by viscous flow as developing at lower cross-link density and higher PCL chain length.

Good shape recovery ratios R_r were achieved for both network series, mainly reduced by irreversible deformations of the polymer networks. The values indicate that with cycling a more and more reliable shape memory behavior could be obtained in any case.

6.2.3. Actuation behavior

Subsequently, the actuation (2W-SM) behavior during thermal cycling between 60 and −20 °C was investigated under isotonic contitions (Figures 6.14). In course of ‘strain-controlled pretreatment’, an elongation of 100% was applied to the PEU specimens and subsequently released to a strain value of 80% (Figure 6.14a). Resulting stresses between 1.3 MPa (PEU-h(ssc)) and 1.9 MPa (PEU-l(ssc)) were maintained during the adjacent thermal cycling. As evident from the strain-temperature plots in cycle $N = 5$ (Figure 6.14b), the actuation magnitude increased from 7% (PEU-l(ssc)) over 16% (PEU-m(ssc)) to 22% (PEU-h(ssc)) with a growing availability of crystallizable PBA segments. This trend corresponds to the findings by Hong *et al.* on polyurethanes with PCL soft segment.[29] As known from other polymeric networks with crystallizable segments, actuation mostly consists in CIE and entropy elasticity (EE) on cooling and MIC on heating.[38,40] Figure 6.14c shows the strain-temperature derivative of the expansion process. Considering the thermal stability of the PBA crystal forms, pronounced signals associated to expansion at 41 °C and slightly above 30 °C were assigned to the PBA α and β crystallization events, respectively. Apparently, under the selected constant stress conditions, PBA crystallized in the elongated networks in two crystal forms with increased crystallization temperatures. These were significantly exceeding crystallization temperatures determined in DSC measurements and even those from shape memory measurements during shape programming (isometric conditions). However, in semicrystalline networks from PPD switching segments, a similar shift in actuation temperature has been verified under constant stress conditions.[40]

Here, the constantly applied stress favored a progressively enhanced alignment of polymer chains and facilitated crystal growth at higher temperatures. On heating, the temperatures of contraction were located at about 50 °C and at 56 °C (Figure 6.14d), which is well above the respective recovery transition temperatures (Table 6.7) and again above the DSC melting peak temperatures (Table 6.2). Following the above described logic, the signals may be again ascribed

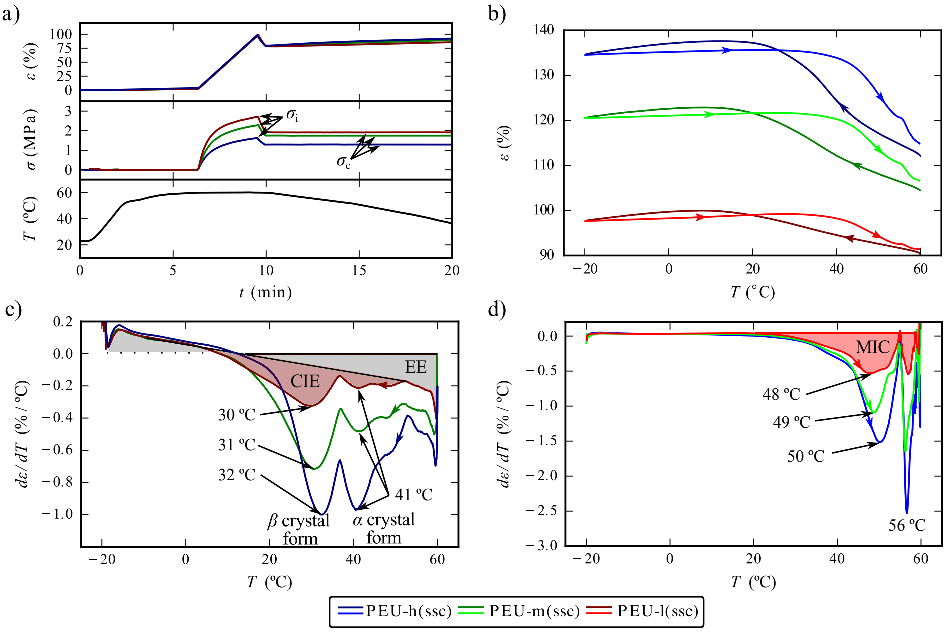

Figure 6.14.: Actuation of PEU-h(ssc), PEU-m(ssc) and PEU-l(ssc) after strain-controlled deformation (strain rate = $0.5\,\%\,\mathrm{s}^{-1}$). a) Strain ε, stress σ and temperature T *vs.* time t relation for the thermomechanical pretreatment, b) evolution of ε in the fifth cooling-heating cycle under constant stresses σ_c of 1.3 MPa (PEU-h(ssc)), 1.7 MPa (PEU-m(ssc)) and 1.9 MPa (PEU-l(ssc)) and the associated strain-temperature derivatives of c) cooling and d) heating.

to the α and β crystal form. However, due to missing evidence and complex PBA melting behavior[191] a definitive assignment in this case is not possible.

6.3. Conclusions

Three PEU block copolymers with various PBA soft segment contents were thermally and mechanically characterized. All of these exhibited pronounced shape memory and actuation behavior, when thermally cycled around the PBA melting and crystallization transition. PBA double melting behavior was observed in DSC due to the existence of two crystalline phases, with the associated polymorphic mixture being sensitive toward the cooling rate during non-isothermal crystallization and subsequent room temperature annealing. The existence of the corresponding PBA crystal forms within the PEU block copolymers, a thermodynamically stable α and a metastable β crystal form, was confirmed using WAXS.

With respect to the shape memory behavior, most pronounced shape changes were observed at highest soft segment content. Increased degree of crystallinity at growing PBA soft segment content supported the highest shape fixities. Lowered shape recoverabilities at a decreased PBA chain length was expected to result from irreversible deformation of the PU hard segment domains. In a progressive approach, systematic adjustment of the thermomechanical parameters allowed to influence the shape memory behavior, which was effected by the PBA polymorphic crystal mixture. This approach allowed to control the thermal stability of the temporary shape and equally the stress and strain recovery profiles. In particular the stress recovery behavior was highly sensitive to melting of the particular polymorphic PBA crystal mixture. Lower cooling rates and increased room temperature holding times resulted in higher amount of α crystallites, thereby enhancing the thermal stability of the temporary shape.

Finally, in actuation measurements, the PBA crystallization and melting transition drove PEU elongation and contraction, respectively. Here, a higher amount of crystallizable soft segment content supported most pronounced actuation magnitudes.

7. PEU Actuation under Various Constant Stresses[e]

This chapter deals with the actuation behavior, *i.e.* the 2W-SME, of a semicrystalline, thermoplastic PEU elastomer (Desmopan® DP 2795A SMP) under various isotonic conditions. Therefore, loads of various magnitudes were applied and partly released in a 'stress-controlled' thermomechanical pretreatment. The PEU actuation behavior, mainly consisting in CIE and MIC, was investigated between −20 and 60 °C. The influence of thermomechanical pretreatment and varying constant load conditions on the PBA crystallization process and thereby on CIE was studied by means of WAXS and DSC. The observed expansion events in actuation measurements were assigned to the crystallization of the particular PBA polymorphic forms and an entropy-elastic stress decrease while cooling. To learn about the actuation mechanism, the ability to conduct triple-shape actuation by employment of the two crystallization and melting transitions of the single PBA soft segment was investigated.

7.1. Thermal Properties

In order to identify suitable testing temperatures for the actuation measurements, the thermal properties of PEU were investigated in DSC (Figure 7.1). In good quantitative agreement with

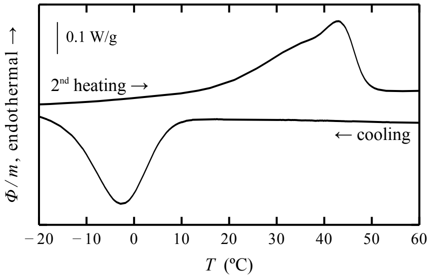

Figure 7.1.: DSC thermograms of the first cooling and second heating run for untreated PEU.

---

[e] © 2012 Wiley. Used with permission from Ref. 5. (List of Publications).

DSC measurements by Pretsch on the same material,[27] endo- and exothermic peaks were ascribed to melting and crystallization of the PBA soft segment at 43 and −3 °C, respectively. Similar to the PEUs in the previous chapter (Section 6.1.3), a single crystallization signal on cooling and a broad endothermic melting signal, likely composed of melting of the PBA α and β crystal forms, were observed.

7.2. Thermomechanical Pretreatment

Table 7.1.: Parameters of actuation measurements: Initially applied stress σ_i, corresponding strain ε_i, precyclic strain ε_{pre} and constant stress σ_c.

σ_i (MPa)	ε_i (%)	ε_{pre} (%)	σ_c (MPa)
0.75	18	15	0.50
1.50	60	47	1.00
1.88	106	79	1.25
2.25	227	199	1.50
3.00	385	362	2.00

Initially, a ‘stress-controlled’ pretreatment prepared the thermoplastic PEU specimens for actuation by the establishment of constant load conditions in a standardized and controlled fashion. To stay well above the PBA melting temperature, the initial deformation during pretreatment was applied at a temperature of 60 °C. Thereby, tensile deformation to an initial loading stress σ_i between 0.75 and 3.0 MPa resulted in deformations between 18 and 385% (Table 7.1).

The stress-strain curves in Figure 7.2 show the tensile deformation behavior of PEU during application of σ_i at a stress-rate of 0.2 MPa min^{-1}. The stress-strain diagrams exhibit an almost linear, elastic region (Hook’s law) at stresses < 1 MPa, which is followed by slight flattening due to the polymer chain alignment. The

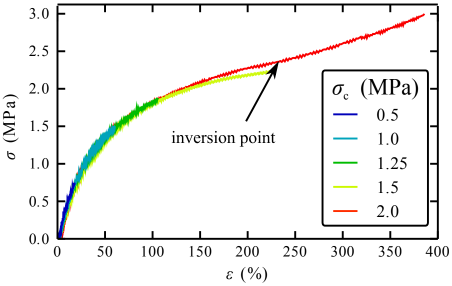

Figure 7.2.: Stress-strain diagrams for PEU specimens at 60 °C ($\dot{\sigma} = 0.2$ MPa min^{-1}) during thermomechanical pretreatment. The inversion point at (2.3 ± 0.1) MPa indicates the onset of deformation-induced crystallization of PBA soft segment.

occurrence of an inversion point at (236 ± 10)% indicates the onset of subsequent strain hardening at stresses above (2.3 ± 0.1) MPa, which is connected to the occurrence of deformation-induced crystallization.[53]

To reduce viscoelastic creep during adjacent thermomechanical cycling, the thermomechanical pretreatment proceeded by releasing the stress to the constant stress $\sigma_c = {}^2\!/_3\,\sigma_i$ a rate of $-0.2\,\mathrm{MPa\,min^{-1}}$. Subsequent temperature holding for 5 min completed the thermomechanical pretreatment, whereby the strain slightly changed (±2%) and finally stabilized at precyclic strains ε_{pre} between 15 and 362% (Table 7.1).

7.3. Thermoreversible Actuation

To investigate the actuation behavior of PEU, the specimens were cooled to −20 °C (below the PBA crystallization transition temperature) and heated to −60 °C (above the PBA melting transition temperature) under various constant stresses σ_c = 0.5, 1.0, 1.25, 1.5 and 2.0 MPa (Figure 7.3). As a result, the PEU specimens showed pronounced expansion on cooling, *e.g.* strain increases between 6 and 47% were detected in the first cooling run (Figure 7.3a). From $\sigma_c = 0.5$ to 1.5 MPa, a steady growth in specimen expansion occured, before it decreased when further increasing the constant stress to 2.0 MPa. On subsequent heating, PEU specimens contracted and thereby recovered the major part of the expansion.

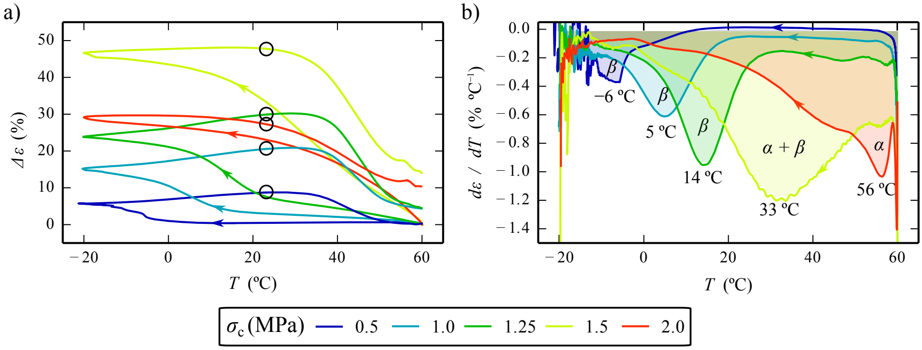

Figure 7.3.: Actuation behavior of PEU under various constant stresses σ_c between 0.5 and 2.0 MPa. a) Strain and b) strain-temperature derivatives during first cooling *vs.* temperature for cycle $N = 1$. Circles in a) mark the cyclic position, where specimens were extracted for subsequent WAXS / DSC measurements.

7.3.1. Crystallization-induced elongation (CIE)

A detailed picture of the expansion behavior is given by the strain-temperature derivatives of cooling (Figure 7.3b). At any loading stress, a minimum in the strain-temperature derivative clearly indicates pronounced expansion due to CIE. At the lowest stress (0.5 MPa), CIE was located at −6 °C, which was slightly lower than the DSC crystallization peak temperature of PBA (−3 °C).[27] Under higher loading stresses, the minima in the strain-temperature derivatives systematically shifted toward higher values, associated with a nominal increase of the temperature of CIE by more than 60 °C.

This shift is in line with a common phenomenon in polymers, connecting the crystallization temperature with the mechanical loading conditions.[202] However, such a strong temperature shift indicates a distinct increase in thermal stability of the PBA crystallites, which hints at PBA polymorphism.

7.3.2. Structure after CIE

To investigate the PBA crystalline state after CIE, PEU samples were extracted from actuation measurements and transferred to WAXS. The obtained diffraction patterns were analyzed together with the one of a thermally pretreated sample, which was exposed to PBA melting and recrystallization (Figure 7.4).

In every single case, crystal reflexes were apparent. Complete Debye-Scherrer rings are a characteristic feature and indicate isotropic distribution of PBA crystallites after PBA melting and recrystallization. As a result of thermomechanical pretreatment and cooling under stresses of up to 1.0 MPa, diffraction patterns with characteristic arcs evolved. These crystal reflexes were ascribed to the PBA β crystal form, likely arranged in lamellae. At stresses of 1.25 MPa and beyond, the reflexes in the diffraction patterns became much sharper and additional reflexes emerged, which were assigned to the PBA α crystal form. In turn, reflexes from the PBA β crystal form gradually decreased in intensity with further stress increase and finally completely disappeared ($\sigma_c = 2.00\,\mathrm{MPa}$). The thermodynamically stable PBA α crystal form was expected to preferably develop in the course of deformation. Such deformation-induced PBA crystallization in the α crystal form has been verified by Koerner *et al.* for a structurally related PEU (Irogran®).[198] Referring to the cooling process, the available PBA α crystallites acted as nuclei and thus promoted epitaxial PBA α crystal growth on the present α crystallites. Such a crystallization behavior has been observed in partially molten PBA homopolymer ($M_w(\mathrm{PBA}) = 9540$ and $12\,200\,\mathrm{g\,mol^{-1}}$).[194,203]

Plots of scattering intensity I *vs.* azimuthal angle φ illustrate the orientation of crystalline constituents within PEU (Figure 7.5). The meridional peaks at $\varphi = \pi/2$ and $3/2\,\pi$ basically

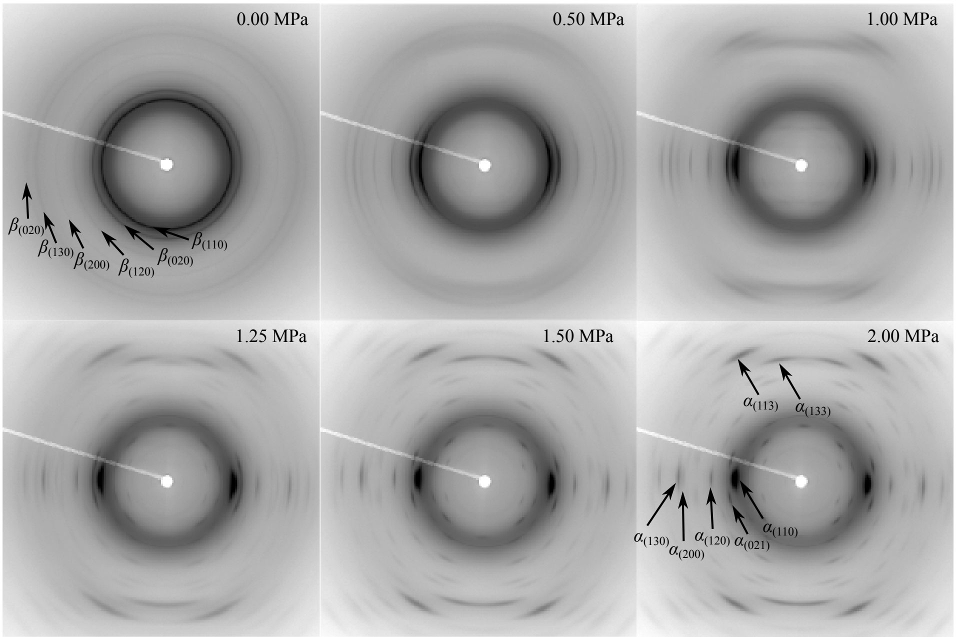

Figure 7.4.: WAXS diffraction patterns of PEU after application of thermomechanical pretreatment with stress pointing in vertically direction, followed by cooling from 60 to −20 °C and heating to 23 °C under various constant stresses σ_c and unloading. In addition, a reference measurement on PEU, which was subjected to PBA melting and recrystallization, is shown (0.00MPa).

represent the PBA $\alpha_{(110)}$ and $\beta_{(110)}$ reflexes, which were located perpendicular to the c-axis of the respective unit cells. Consequently, the c-axis pointed in both cases in direction $\varphi = 0$, implying that the long period of the PBA α and β crystallites was oriented parallel to the applied stress. In general, a higher orientation is expected to enhance specimen expansion in the course of cooling. However, an increase in the intensity of the major signals at $\varphi = {}^{\pi}/_{2}$ and ${}^{3}/_{2}\,\pi$ suggests a progressively growing orientation with a maximum magnitude at 2.0 MPa, which remarkably did not correspond to the highest expansion magnitude detected on cooling. The most pronounced expansion was exhibited by the measurement at a constant stress of 1.5 MPa. It is concluded, that with the higher degree of deformation-induced PBA crystallization the orientation of the PBA crystallites increased.

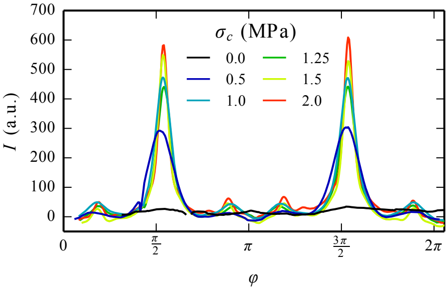

Figure 7.5.: Azimuthally integrated intensities of WAXS for PEU after application of thermomechanical pretreatment, followed by cooling from 60 to −20 °C and heating to 23 °C under various constant stresses σ_c and unloading.

DSC measurements were conducted on PEU specimens, which were subjected to the same thermal and thermomechanical pretreatment as those studied by WAXS. Figure 7.6 shows the endothermic signals of the first heating run, and thereby reflects the thermomechanical history of PEU specimens.

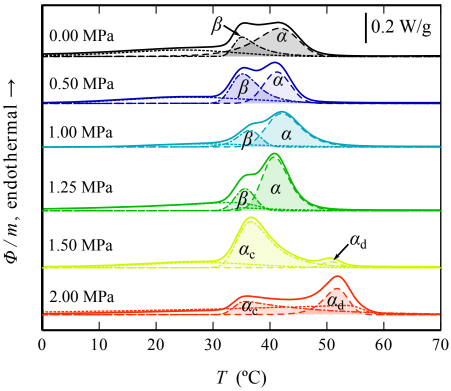

Figure 7.6.: DSC endotherms for untreated PEU (second heating scan) and after thermomechanical treatment (first heating scan). The PBA melting enthalpies are (from top to bottom) 20.3, 23.2, 22.0, 17.9, 24.9, 22.5, 23.6 and 22.6 J g^{-1}.

The thermally pretreated PEU exhibited a signal peak at 42 °C with a shoulder located at 35 °C. In agreement with the assignment made in Section 6.1.2, the shoulder and the main signal were ascribed to the melting of the PBA β and α crystal forms, respectively. The presence of

PBA α crystallites was due to a $\beta \rightarrow \alpha$ crystal-crystal transformation, starting after thermal pretreatment. Comparable melting behavior is also known from PBA homopolymer ($M_w(\text{PBA}) = 40\,000\,\text{g}\,\text{mol}^{-1}$).[191] When the load during actuation measurements was raised to 1.25 MPa, the lower temperature shoulder decreases in magnitude. At even higher stresses (1.5 MPa), the lower temperature signal suddenly increased, while the main melting signal at 42 °C disappeared. Instead, a new signal emerged at 51 °C and increased at even higher stress (2.0 MPa). The sudden appearance of a new peak suggests a drastic change in the crystalline morphology of the PBA soft segment.

Taking into account the results of our WAXS measurements, both signals at 2.0 MPa have to be ascribed to the PBA α crystal form. The question arises, why α crystal melting exhibited two signals. As a possible explanation, similar to other polymers subjected to ‘hot drawing’ and adjacent crystallization,[96,99,204] a shish-kebab structure with deformation-induced shish cores and kebab lamellae may have formed due to two crystallization processes. Accordingly, the higher temperature signal labeled by α_d likely originated from the shish core, which is a fibrous crystalline structure developing during deformation-induced PBA crystallization. Shish cores have been found to melt at temperatures significantly above the equilibrium melting transition, *e.g.* showed superheating in polypropylene by 13 °C.[205] A fibrous structure could thus explain the high-temperature melting signal at 51 °C. The associated deformation-induced crystallization was indicated by the occurrence of an inversion point and a following stress increase in the stress-strain diagrams (Section 7.2). The lower temperature signal α_c at 1.5 and 2.0 MPa may have originated from PBA α lamellae epitaxially melt-crystallizing as a kebab structure around the fibrous shish core. These lamellar crystallites may have dominated PBA melting and crystallization during thermal cycling under constant load and thus determined CIE and MIC during PEU actuation.

Slight initial expansion at isotonic conditions below 1.5 MPa can not be explained by CIE. In an attempt to separate this phenomenon from the actuation hysteresis, the lower temperature T_{low} during thermal cycling was set to 10, 20 and 30 °C. For an exemplarily chosen constant stress of 1.25 MPa, the change in strain $\Delta\varepsilon$ is shown for cycle $N = 1$ (Figure 7.7). When the specimen was cycled in between 60 to 30 °C, an almost linear strain-temperature dependence between 50 and 30 °C was observed on cooling as well as on heating. Such thermoreversible strain-temperature dependence in the rubbery state of PEU is at-

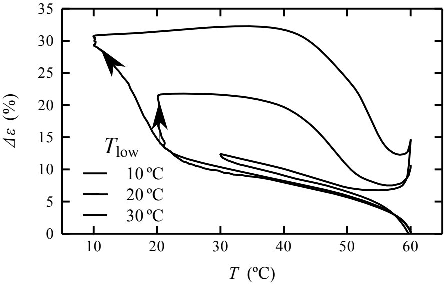

Figure 7.7.: Strain-temperature diagram of the first cycle for PEU under 1.25 MPa for different lower temperatures T_{low}.

tributed to entropy elasticity, for which the stress at a given elongation is a linear function of the temperature (Formula 2.2, Section 2.3.2). In effect, the resistance to the external load decreases on cooling, yielding a net strain increase.

Contrariwise, when a lower temperature T_{low} of 10 °C or 20 °C was selected, the temperature-linear expansion on cooling was followed by pronounced expansion due to CIE. In these cases, subsequent heating did not induce immediate contraction. Instead, the strain stayed at a high, stable level, until pronounced contraction finally started at ~ 37 °C. Stable strains at lower temperature suggest, that PBA crystallites formed a temporary network, which fixed the expanded strain of the low-temperature shape. Such material behavior is known from one-way shape memory measurements on the same material.[113,121] Accordingly, cooling below the crystallization peak temperature of -4 °C was able to fix 99% and more of an applied deformation of 100%. The temporary shape only becomes unstable when the PBA melting temperature was exceeded, thus the network from PBA crystallites vanished and thereby shape recovery was induced. Similarly, heating above the PBA melting temperature under isotonic conditions triggered MIC, even against the constraint of a constant external load. In result, MIC almost completely reversed CIE. Therby, the strain-temperature trajectory formed a hysteresis between the PBA crystallization and melting temperatures.

7.3.3. Melting-induced contraction (MIC)

The strain-temperature derivatives in Figure 7.8 illustrate the mechanical response of PEU to heating under the above discussed isotonic conditions. Accordingly, the loaded PEUs showed rather homogeneous contraction behavior. At any stress, a major signal between 43 and 46 °C

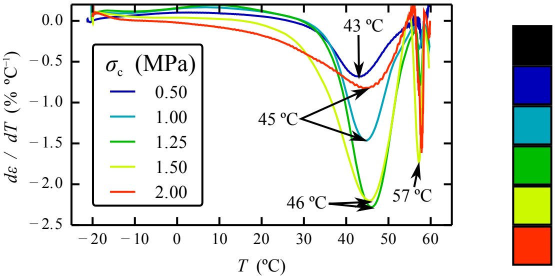

Figure 7.8.: Strain-temperature derivatives of heating plotted *vs.* temperature for PEU in the first thermomechanical cycle, which was thermomechanically pretreated and thermally cycled under various constant stresses σ_c.

in the strain-temperature derivative of heating was attributed to PBA melting, inducing specimen contraction due to entropy elasticity. Compared to the above described DSC melting temperatures, the temperatures of specimen contraction were increased, caused by the isotonic stabilization of the PBA crystallites. Concluding from WAXS and DSC data, the contraction signals at lower stresses were ascribed to the melting of the PBA β crystal form. In contrast, melting of the melt-crystallized PBA α crystallites was responsible for the major signal at higher stress (≥ 1.5 MPa). The marginal narrow peak at 57 °C was not clearly distinguishable from a measurement artifact caused by a test segment change in that temperature range.

7.3.4. Cyclic actuation behavior

Further interest was devoted to the cyclic evolution of the PEU actuation behavior. Therefore, the above mentioned isotonic conditions were again selected (1.25 MPa) and the actuation behavior of five thermomechanical cycles was determined (Figure 7.9).

Each cycle showed pronounced CIE and MIC. After completion of cycle $N = 1$, a residual strain of 4.5% remained, which may result from creep under isotonic conditions. This strain constituted the starting point of the second thermomechanical cycle. With ongoing cycling, the strain offset continuously increased, such that the entire strain hysteresis curve was shifted to higher strains. With an increasing number of cycles, the increment in strain due to creep diminished to a value of 1.3% in cycle $N = 5$. When drastically increasing the number of cycles to $N = 20$, residual strains as low as 0.3% were quantified, indicating the progressively increasing stability of thermoreversible PEU actuation.

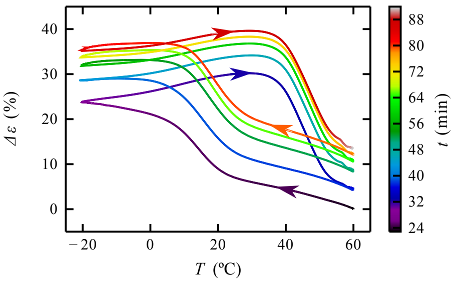

Figure 7.9.: Strain-temperature diagram for five thermal cycles of PEU under $\sigma_c = 1.25$ MPa.

Figure 7.10 shows PEU actuation of cycle $N = 5$ under various isotonic conditions between 0.5 and 2.0 MPa. Here the influence from creep was negligible. The strain-temperature trajectories formed distinct hysteresis loops up to stresses of 1.25 MPa, while at a higher stress of 1.5 MPa the hysteresis disappeared and the PEU specimen followed almost identical strain-temperature pathways during cooling and heating. Finally, at a stress of 2.0 MPa, the hysteresis even reversed, exhibiting contraction on cooling at temperatures below the expansion temperatures on heating.

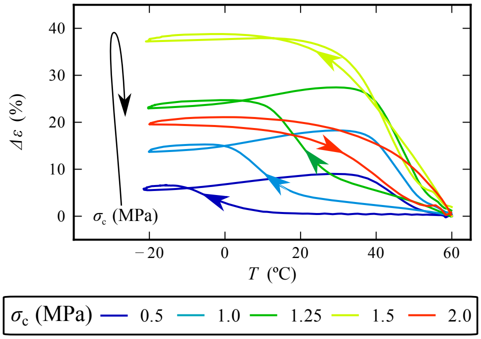

Figure 7.10.: Strain-temperature diagram of PEU under various constant stresses σ_c in cycle $N = 5$.

Compared with the first cycle, a systematic increase in the crystallization temperatures was observed in the strain-temperature derivatives (Figure 7.11a), *e.g.* CIE at 1.25 MPa shifted from 14 to 19 °C. This observation hints at increasing lamellar thickness or higher crystal perfection due to repeated thermomechanical cycling.

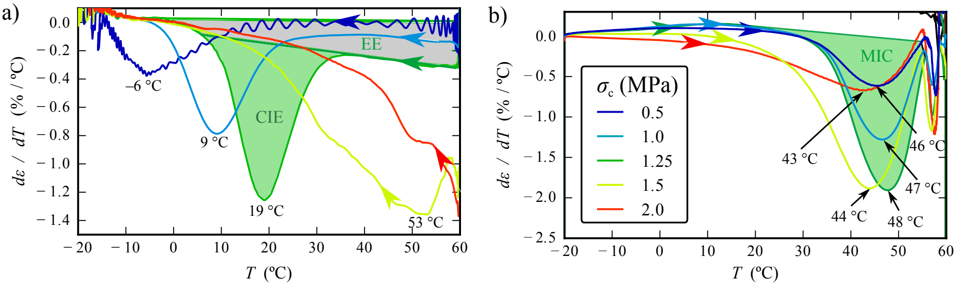

Figure 7.11.: Strain-temperature derivatives $d\varepsilon/dT$ for PEU actuation ($N = 5$) of a) cooling and b) heating under various constant stresses σ_c. Colored areas highlight the individual contributions of entropy elasticity (grey), crystallization-induced elongation (CIE, green) and melting-induced contraction (MIC, green) for $\sigma_c = 1.25$ MPa.

Moreover, at a stress of 1.5 MPa, the maximum temperature of CIE even shifted from 33 °C to 53 °C close to the maximum testing temperature, indicating the formation of stable α crystallites due to the successive deformation. In this case, the permanent isotonic conditions and the repeated heating above the equilibrium melting temperature seem to also have supported the formation of the high-temperature stable α crystal form, indicated by a high intitail value of the strain-temperature derivative at 60 °C. These crystallites then likely acted as nuclei for instantaneous and progressive crystallization on cooling, as it is known for PBA homopolymer.[194,203] As a result, CIE took place at temperatures as high as 53 °C, and even reached almost 60 °C for constant stress conditions of 2.0 MPa.

For the actuation curve at $\sigma_c = 1.25$ MPa, the individual contributions from CIE and entropy elasticity were exemplarily calculated. A linear function from regression of the strain-temperature derivative of cooling (Figure 7.11a) between 40 and 60 °C and extrapolation toward lower temperatures allowed to virtually separate the expansion associated with entropy elasticity and CIE. In the considered case, numerical integration of the respective areas above and below the linear regression function yielded strain expansion by 11.6% and by 12.0%, assigned to entropy elasticity and CIE, respectively. Thus expansion at 1.25 MPa consisted in almost equal parts of the temperature-linear entropy elasticity and CIE. The corresponding areas are highlighted in Figure 7.11a.

Final contraction of the PEUs was most pronounced at temperatures between 43 and 48 °C for all the tested stresses (Figure 7.11b). Here it is noticeable, that contraction signals at increased isotonic load, connected to the melting of the α crystal form, were located at slightly lower temperatures and show a more pronounced extension to lower temperatures. Such melting behavior indicates the presence of a stability inversion of α and β crystallites. Similar behavior has been observed by Gan *et al.*[191] and is ascribed to decreasing lamellar thicknesses of transformed α crystallites.

7.4. Reversible Triple-Shape Actuation

To investigate the feasibility of triple-shape actuation behavior in PEU, the standard pretreatment was applied to the PEU specimens. The thermal testing conditions during cycling were slightly modified. In particular, an intermediate holding temperature of 55 °C was introduced, such that thermal cycling between −20 and 55 °C almost reproduced the standard actuation temperature range (Figure 7.11). The lower testing temperature T_{low} was retained at −20 °C and the higher testing temperature T_{high} was increased to 70 °C. Diagrams of the respective strain evolution in the fifth thermomechanical cycle (Figure 7.12) show strain and temperature *vs.* time. In agreement with the above described single expansion process from β crystallization at $\sigma_c < 1.5$ MPa (Figure 7.3), expansion under triple-shape conditions was observed in the second cooling run between 55 to −20 °C. However, crystallization in the β crystal form was unable to promote significant shape changes on initial cooling from 70 to 55 °C (Figure 7.12a). In contrast, at a stress of 1.5 MPa, a slight strain increase of 4% in the first cooling run was observed, together with pronounced expansion during the second cooling.

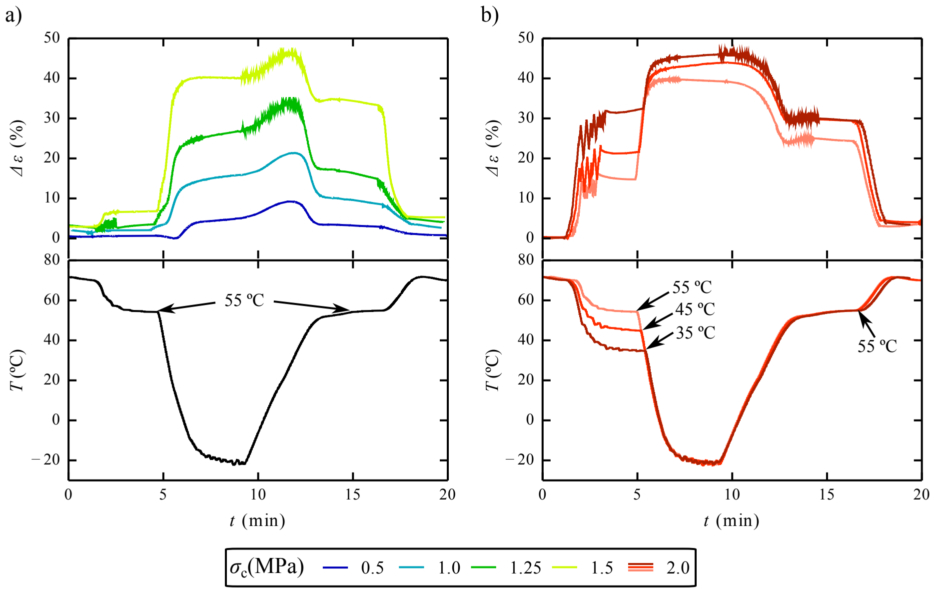

Figure 7.12.: Diagrams of strain (top) and temperature (bottom) *vs.* time during two-staged cooling and heating of PEU in cycle $N = 5$ for isotonic conditions a) between 0.5 and 1.5 MPa and b) at 2.0 MPa. Thermal cycling was conducted in between -20 and 70 °C with intermediate holding temperatures as indicated.

A pronounced first expansion of 15% (Figure 7.12b) was observed in the strain-temperature derivative at a constant stress of 2.0 MPa. In agreement with the DSC measurements, these expansion events were attributed to epitaxial crystal growth on deformation-induced, likely fibrillar α crystallites and subsequent development of the purely cooling-induced α crystal form, respectively. Even more, when the intermediate temperature was lowered to 45 and 35 °C, increased expansion strains were observed during first cooling (21 and 31%, respectively). The total expansion strains after both cooling runs add up to 40% ($T_{mid} = 55\,°\mathrm{C}$), 44% ($T_{mid} = 45\,°\mathrm{C}$) and 46% ($T_{mid} = 35\,°\mathrm{C}$). In line with the dual-shape actuation measurements at 2.0 MPa, this trend emphasizes that crystal growth under the given conditions is more pronounced at higher temperatures, which can be explained by an increased segmental mobility of the PBA segments. A drawback of actuation at stresses as high as 2.0 MPa is a high precyclic strain of 358%.

During temperature holding at -20 °C and on initial heating, the PEU specimens slightly expanded at stresses $\sigma_c \leq 1.5$ MPa (Figure 7.12a). Such a response suggests the occurrence of PBA post-crystallization and a $\beta \rightarrow \alpha$ crystal-crystal transition, respectively. At 2.0 MPa, the high degree of deformation-induced crystallization and the presence of a purely PBA α crystal form prevent such expansion. In any case, final heating to 55 and 70 °C yielded two distinct PEU specimen contractions and a stable intermediate shape at 55 °C. Subsequent melting of the PBA β and α crystal forms drove two sequential contractions at stresses $\leq$ 1.5 MPa. At 2.0 MPa, the two melting signals were attributed to the melting of the melt-crystallized and deformation-induced PBA α crystallites.

In an attempt to demonstrate, that indeed two separated crystallization and melting processes were involved in the two-step expansion and contraction behavior, thermal cycling after the commonly applied thermal pretreatment was conducted between 70 and −20 °C, while the intermediate holding step was omitted. The corresponding stress-strain derivatives in the fifth thermomechanical cycle are depicted in Figure 7.13. The derivative of expansion (Figure 7.13a) shows a broad peak with a maximum signal at 63 °C. Peak deconvolution was conducted by fitting two EMGs in the interval between 0 and 68 °C. As clearly indicated, two signals with peak temperatures separated by a difference of almost 20 °C suggest the presence of two subsequent crystallization events. In line with the assignments made for the melting signals in the calorimetric measurements, the deconvolved expansion events were ascribed to epitaxial crystal growth on the deformation-induced crystallites (α_d) and the melt-crystallized (α_c) lamellae. The intersection of the signals at 53 °C demonstrates that the intermediate temperature of 55 °C in the above described triple-shape actuation measurements was appropriately selected.

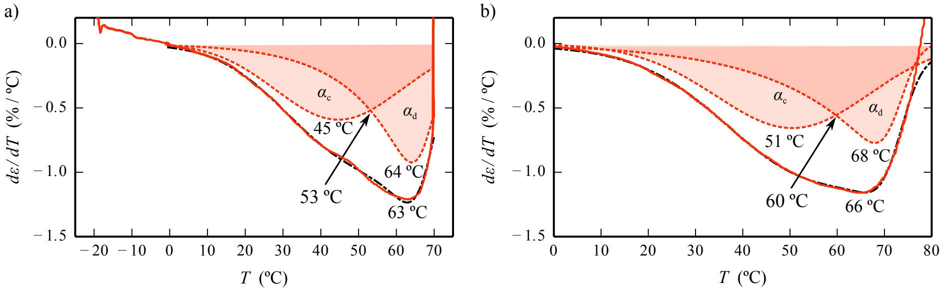

Figure 7.13.: Deconvolved strain-temperature derivatives of PEU actuation at a stress of 2.0 MPa and a modified upper testing temperature. Given are a) expansion on cooling and b) contraction on heating.

Finally, the MIC during heating was investigated. To remain free of measurement artifacts, an upper temperature of $T_{high} > 75$ °C was selected (only for the final heating run, not during prior thermomechanical pretreatment and cycling). In result, PBA melting drew a very similar picture (Figure 7.13b), confirming the findings deduced from the previous cooling run.

7.5. Conclusions

PEU showed actuation behavior under various constant loads. With the intention to lower the viscous creep in subsequent thermal cycles, an excessive tensile deformation during thermomechanical pretreatment was applied. The associated application of a strong deformation turned out to effect the subsequent polymorphic crystallization behavior. Accordingly, the temperature and magnitude of the adjacent PBA crystallization transition during thermomechanical pretreatment, and thereby CIE and MIC of the PEU specimen, were influenced. As detected by WAXS, small deformations favored PBA crystallization in the kinetically preferential β crystal form. At higher loads, deformation-induced PBA α crystallites developed, which supported further PBA α crystal growth on isotonic cooling. Calorimetric measurements allowed to further distinguish between deformation- and cooling-induced PBA α crystallites. The magnitude of CIE was highest, when a small fraction of deformation-induced PBA α crystallites favored pronounced cooling-induced PBA crystallization. Finally, MIC completed the actuation cycle. When adding an additional intermediate temperature holding step on cooling and heating, PBA double phase crystallization and melting transitions could be exploited to achieve isotonic triple-shape actuation.

8. PEU Actuation under Stress-Free Conditions[f]

In the previous section, thermoreversible actuation of a semicrystalline PEU was investigated under various isotonic conditions. It turned out that deformation-induced crystallization during thermomechanical pretreatment significantly supported the subsequent actuation behavior, even after partially releasing the applied stress. This was motivation to test the feasibility of PEU actuation behavior after complete stress release. Consequently, the applied thermomechanical pretreatment was modified such that extensive tensile PEU deformation maximized the degree of PBA deformation-induced crystallization. After adjacent stress release, the thermally-induced mechanical response of the specimen to cooling and heating was studied.

To probe the microstructural evolution during thermal cycling, *in situ* WAXS measurements monitored the PEU crystalline structure and orientation. In addition, DSC measurements were conducted on specimens after training. Finally, the geometric versatility of the applied concept was investigated in compressive and torsional arrangements.

8.1. Training and Actuation

In a first step, thermomechanical 'training' prepared the PEU for actuation. Therefore, the PEU specimen was heated to 60 °C (above the PBA melting transition, Figure 7.6 in Section 7.1) and an extensive, tensile deformation of 1000% was applied at a rate of 1 % s^{-1} (12 mm min^{-1}, Figure 8.1).

The stress-strain curve shows an inversion point at (2.4 ± 0.04) MPa and (201 ± 11)%, which differs from the previously detected inversion point (Section 7.2) due to the different specimen geometry. Further stress increase

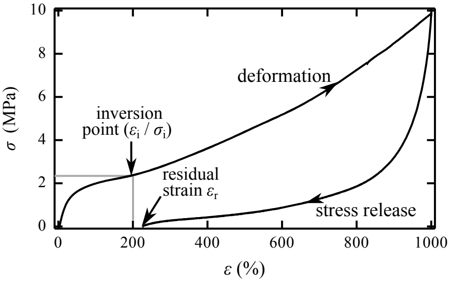

Figure 8.1.: Tensile stress σ *vs.* strain ε during thermomechanical pretreatment of PEU at 60 °C.

---

[f] Chapter adapted from Ref. 6. (List of Publications) with permission from The Royal Society of Chemistry.

and subsequent strain hardening up to a maximum stress of 9.9 MPa indicate the occurrence of pronounced deformation-induced PBA crystallization.[53]

After stress release, plastic residues of the relaxed sample defined the starting point for actuation in subsequent thermal cycles. The large plastic deformation (ε = 208%) is expected to mainly result from viscous flow of the amorphous soft segment domain and deformation-induced crystallization. Strain, temperature and stress *vs.* time for the entire measurement are depicted in Figure 8.2a. The inset shows a magnified view of the strain.

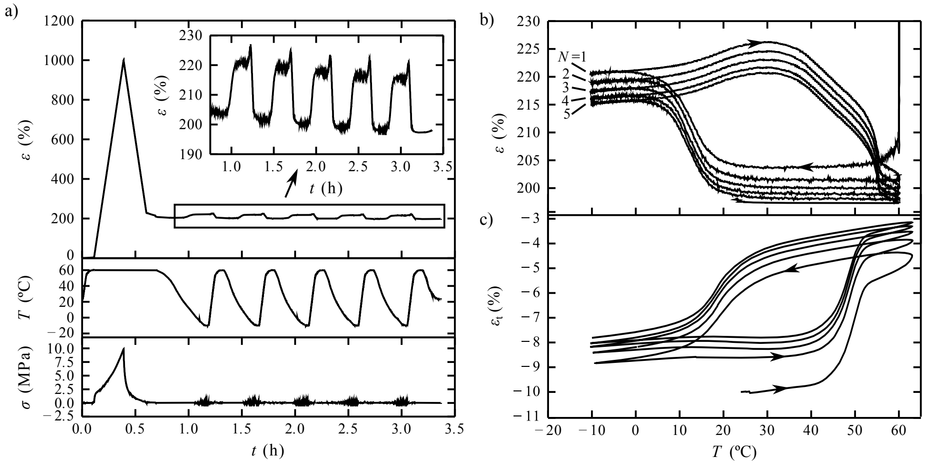

Figure 8.2.: Tensile training and subsequent actuation in PEU. Strain ε, temperature T and stress σ for the full measurement plotted a) *vs.* time t, b) *vs.* temperature T and c) PEU specimen thickness ε_t *vs.* temperature T perpendicular to the training direction as determined in dilatometric measurements.

Intestingly, the trained PEU specimen exhibited cyclic expansion and contraction. The thermal cycle started by cooling the PEU from 60 to −10 °C, to which the specimen responded by a remarkable expansion of 17%. When re-heating the specimen to 60 °C, it first expanded by 6% before it finally shrank by 25%. Photos give a visual representation of the two specimen shapes in Figure 8.3.

The change in strain plotted *vs.* temperature exhibited a hysteretic profile (Figure 8.2b), similar to the profiles observed under isotonic conditions (Section 7). CIE and MIC were located at temperatures between 10 and 20 °C and 35 and 50 °C, respectively. However, no sign of entropy-elastic expansion on initial cooling was detected, which can be explained by the absence of stress.

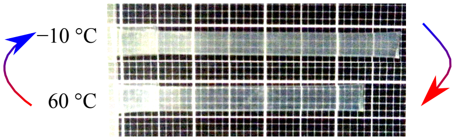

Figure 8.3.: Photos of a cut from a trained PEU specimen at −10 and 60 °C.

A strain-temperature curve from dilatometric measurement visualizes the flattening and thickening of an identically trained sample perpendicular to the training direction (Figure 8.2c). Accordingly, in course of thermal cycling the thickness decreased by 4.3% on cooling and increased by 4.9% on heating. Under the assumption of a constant specimen width, estimation of the PEU volumes at 60 °C (0.351 cm^3) and −10 °C (0.353 cm^3) exemplifies that expansion and contraction were apparently volume conserving.

Cyclic reproducibility of the actuation behavior was high, as evident in cooling-heating cycles quantifying elongation and thickness. A continuous development of the PEU specimen toward its original shape, *i.e.* lower elongation and higher thickness, is ascribed to viscoelastic creep. With proceeding cycling, the influence of creep gradually diminished. Moreover, measurements exhibiting 22 thermal cycles (Figure 8.4) and measurements on a trained PEU specimen, which has been stored for more than two weeks at room temperature (23 °C), suggest that cyclic actuation does not decrease over time but is a persistent phenomenon, with the amount of actuation cycles not explicitly limited.

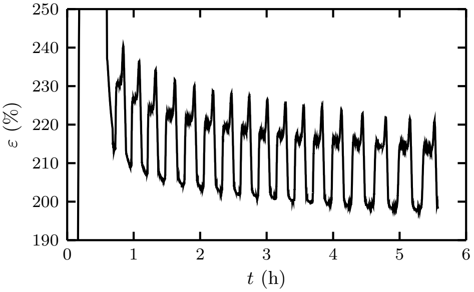

Figure 8.4.: Strain ε *vs.* time t of PEU during 22 cooling-heating cycles.

For comparison, thermal expansion of an untreated PEU specimen was investigated in TMA. Here, an expansion of 1.7% in the considered temperature range between −10 and 60 °C was observed, which is one order of magnitude lower than the above described actuation, clearly emphasizing the significance of the observed phenomenon.

Similar observations of stress-free actuation have been made by Behl *et al.*[206,207] and Zhou *et al.*[208] The former group found up to 250 stable actuation cycles in poly[ethylene-*co*-(vinyl acetate)] with polyethylene (PE) segments after a related thermomechanical training procedure. In their case, training consisted in a deformation at a temperature between the PE melting onset and offset temperature.

8.2. Microstructural Processes

To study the underlying processes of thermally induced two-way shape changes, *in situ* wide-angle X-ray scattering (WAXS) measurements resolved the microstructural evolution, including

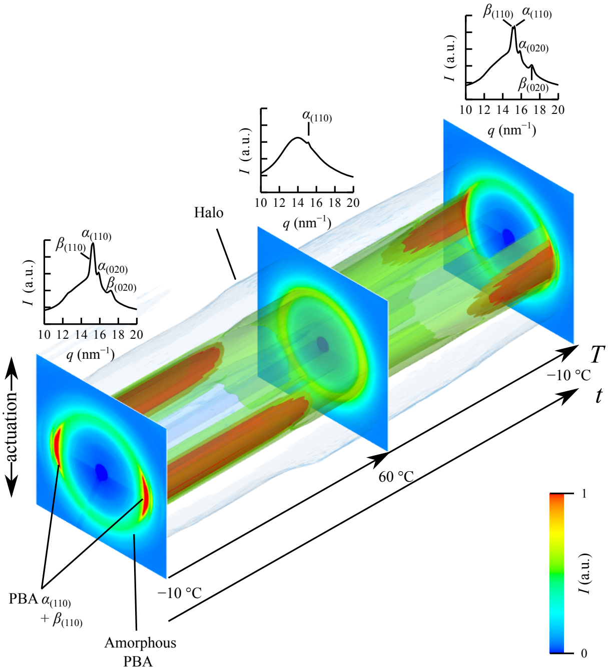

Figure 8.5.: Microstructural evolution of a trained PEU sample as illustrated by a 3D rendering of 52 successively aligned diffraction patterns (diffractograms attached). The sample was heated from its semicrystalline state at −10 °C (left) to 60 °C (above the PBA melting transition) and cooled to −10 °C (below the PBA crystallization transition).

changes of the crystalline morphology and orientation inside of trained PEU specimen. The diffractograms were continuously taken, while the specimen was heated from −10 to 60 °C and subsequently cooled to −10 °C (Figure 8.5)

Initially, PBA was in a semicrystalline state. The concentric ring (green) was attributed to disordered, amorphous PBA domains. Crystal reflexes were assigned to the PBA α and β crystal forms (compare Section 6.1.3). A strong equatorial signal from superposition of the PBA $\beta_{(110)}$ and $\alpha_{(110)}$ reflexes at $q = 15.09\,\mathrm{nm}^{-1}$ and $q = 15.31\,\mathrm{nm}^{-1}$, respectively, implies the presence of a long-range order and alignment of the PBA crystallites in direction of deformation applied during tensile training. Further crystalline reflections from the α and β crystal forms were detected, as displayed in the radial integration patterns attached to the diffractograms in Figure 8.5. In the course of heating to 60 °C the majority of crystalline reflexes disappeared, while an increasing intensity of the isotropic ring from the amorphous domain and extension of the halo indicates an increasing amount of amorphous PBA soft segment. Only a minor peak, visible in the inset at 60 °C suggests the existence of a small amount of high-temperature stable α crystallites within the rubbery PBA matrix. When the thermal cycle was completed by subsequent cooling, the heating process was almost completely reversed and the oriented crystalline reflections re-emerged.

To confirm the existence of high-temperature stable α crystallites, the melting behavior of a trained PEU sample was investigated in DSC (Figure 8.6). Here, the commonly observed PBA melting signal in the first heating (compare Section 7.1, Figure 7.1) run was accompanied by a tiny signal at 63 °C, strengthening the above made ascription.

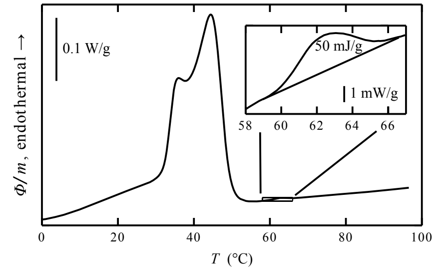

Figure 8.6.: DSC thermogram of first heating run for a trained PEU sample, showing the melting of PBA crystallites from cooling-induced crystallization and from deformation-induced crystallization (inset).

The plot of the Herman's orientation function f_o *vs.* temperature illustrates microstructural ordering and disordering during thermal cycling (Figure 8.7). It was calculated for each WAXS diffractogram, is 1 for a fully vertically aligned and 0 for a completely isotropic system. Its development is described by a hysteresis above temperature similar to the one of thermomechanical

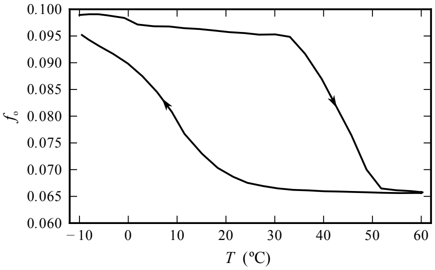

Figure 8.7.: Herman's orientation function f_o *vs.* temperature T, as calculated from the individual WAXS diffractograms after azimuthal integration.

actuation. In greater detail, the initial, semicrystalline state at −10 °C possessed an orientation of $f_o = 0.10$. When the temperature exceeded an onset of ~ 35 °C, a monotonous decrease of f_o to 0.06 parallel to the almost complete disappearance of the crystalline reflexes was observed. On cooling, from temperatures of 25 °C and below the polymer's initial long-range orientation was restored.

This behavior contrasts the typically isotropic crystallization behavior of polymers. For clarity, *in situ* WAXS was conducted on an untrained reference specimen (Figure 8.8).

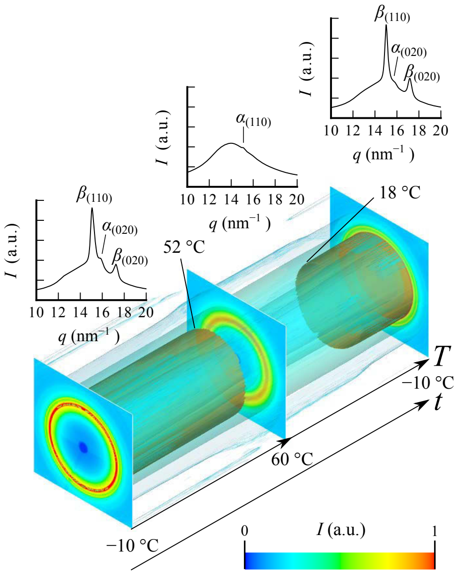

Figure 8.8.: Microstructural evolution of an untrained PEU sample as illustrated by a 3D rendering of 52 successively aligned diffraction patterns (diffractograms attached). The sample was heated from its semicrystalline state at −10 °C (left) to 60 °C (above the PBA melting transition) and cooled to −10 °C (below the PBA crystallization transition).

Indeed, in this case Debye-Scherrer rings were apparent over the entire temperature range, indicating the isotropic orientation of crystalline and amorphous domains during thermal cycling.

8.3. Modelling

In nematic liquid crystal elastomers, microstructural orientation plays a major role to achieve macroscopic actuation. For example, a collective orientation of rod-like molecules following the nematic director leads to expansion, while contraction is driven by the reversible process.[209] Similarly, the semicrystalline PEU specimen exhibited actuation, while it microscopically switched from an ordered, semicrystalline state at low temperature to a disordered, rubbery state at high temperature and *vice versa*. Here, the cause for microstructural orientation during cooling is addressed by firstly proposing a mechanism for global orientation of crystalline domains and secondly describing the microscopic shape change of a single PBA monomeric unit.

Apparently, a training procedure including excessive deformation, which exceeds the onset of deformation-induced PBA crystallization, is a necessary prerequisite for actuation in semicrystalline PEU (Figure 8.1). Koerner *et al.*[198] describe an arising global orientation after extensive deformation and relaxation for a related thermoplastic elastomer consisting of MDI and PBA (Irogran®). The group observed planar crystal lamellae, which consisted of α crystals oriented parallel to the deformation direction. In the present case, a similar alignment of crystallites after deformation was therefore expected. These oriented α crystals were stable at 60 °C, as detected in radial integration patterns at 60 °C (Figure 8.5) as well as in DSC (Figure 8.6). Consequently, these crystallites persisted after stress release and throughout cycling within the PBA matrix and thereby memorized the direction of training. On cooling, the present crystallites served as nuclei for oriented PBA crystallization. In good agreement with literature on PBA homopolymer,[194,203] a small amount of PBA α crystal nuclei within the PBA melt facilitated the formation of a polymorphic PBA mixture. In a fashion of self-organization, oriented PBA α and β crystallites may have grown on oriented α crystallites by chain folding of the PBA chains perpendicular to the training direction (Scheme 8.1). As an alternative explanation, crystallization of an oriented melt under load, as it is observed in cross-linked polyethylene, results in a parallel orientation of complex mesomorphic crystalline structures.[210] In that case, fibrous cores from deformation-induced crystallization parallel to the deformation direction induce row nucleation. In a similar matter, epitaxial crystal growth may have promoted lamellar formation with the chain axis oriented parallel to the deformation direction, as it has been observed for polyesters under load.[211] In any case, the existence of residual crystallinity at high temperature inevitably predetermined the global orientation of the crystalline regions after recrystallization.

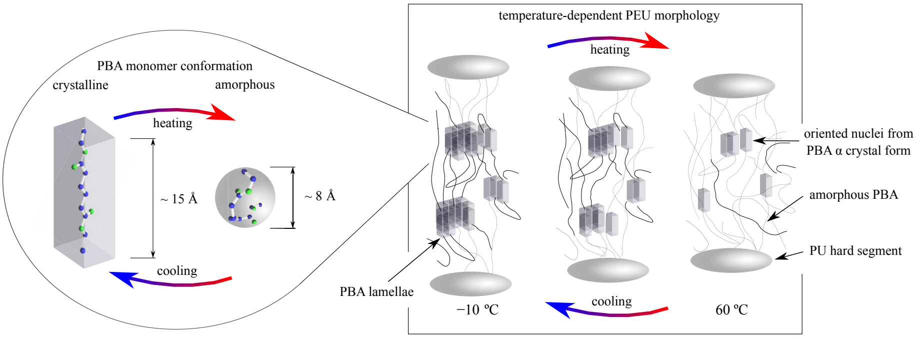

Scheme 8.1: Model proposed to explain the macroscopic PEU actuation on the base of microstructural changes, *i.e.* by adaptation of chain conformation and crystal orientation.

In an attempt to generate a better understanding of the observed actuation magnitude, the temperature-dependence of the PBA conformation for a single monomeric chain is discussed. In the semicrystalline state, the chain is fully extended,[196] embedded into the well-defined geometry of either an orthorhombic or a monoclinic crystal system with a long period of the unit cells of at most 14.7 Å (see Scheme 8.1, right hand side). In contrast, the entropically preferred, random coil conformation of a molten chain is isotropic, thus constitutes a spherical probability density.[42] For the sake of simplicity, the amorphous PBA chain is presumed to form a microscopic sphere[68,212] with a molecular packing similar to that of the α crystallites (the density $\rho_{PBA} = 1.019\,\mathrm{g\ cm^{-3}}$ only slightly alters when melting, density of α crystal form $\rho_\alpha = 1.023\,\mathrm{g\ cm^{-3}}$),[196] having a diameter of $\sim 8\,\text{Å}$. Accordingly, switching between the basic microscopic shapes of the PBA monomer, namely the spherical, random coil conformation with a diameter of $\sim 8\,\text{Å}$ and the crystalline cuboid conformation with an extension in c-direction by up to ~14.7 Å drives microscopic expansion and contraction in direction of the unit cells long period by ~ 80%. With the degree of PEU crystallinity (15%) assumed to linearly correlate to the quantified macroscopic shape changes, expansion and contraction of the crystallizable domains by a strain of 80% motivates macroscopic expansion and contraction by about 12%. Comparison with the measured actuation strain has to consider the initial length of the specimen after training, *i.e.* the persistent deformation, as the initial specimen length. Accordingly, an upper limit of the expansion strain of about 36% is expected for the given tensile actuation, slightly exceeding the determined value of 25%. Presumably, phenomena reducing the actuation magnitude explain that difference, such as imperfect orientation of PBA crystallites as well as internal specimen stress due to constraints from the network structure.

8.4. Polymorphic Transition

Finally, the observation of an initial expansion on heating by about 6% is addressed. Similarly to the above described CIE on cooling, a correlation with crystallization processes was expected. In the considered temperature-region between 0 °C and 40 °C, a $\beta \rightarrow \alpha$ crystal-crystal transformation is likely to occur.[191] In addition, strain changes of about 1% due to a $\beta \rightarrow \alpha$ crystal-crystal transformation have been observed in polytetrafluoroethylene by Hornbogen.[213]

Radially integrated WAXS diffractiograms during heating from −10 °C (blue) to 52 °C (red) show signals from the PBA α and β crystalline form (Figure 8.9a). Signals ascribed to the β crystalline form disappeared first due to PBA melting, while signals originating from the α crystalline form only slowly diminished. A clear sign of a crystal-crystal transformation has not been found. In any case, thermal expansion of the α and β unit cells, as suggested by a shift of crystalline reflections to lower values of the scattering vector q, might have participated in the observed expansion. Thereby, the dominant $\alpha_{(110)}$-peak almost reached the positioning of the $\beta_{(110)}$-peak (shifted from 15.26 to 15.11 Å).

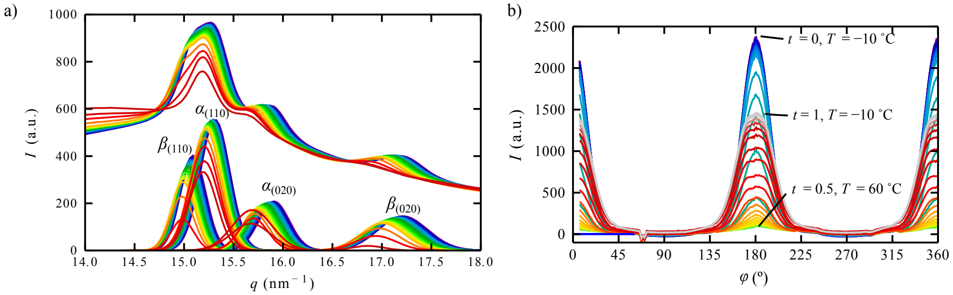

Figure 8.9.: Intensities from *in situ* WAXS measurements: a) radially integrated WAXS intensity and deconvolved reflexes *vs.* scattering vector q while heating the trained PEU specimen from −10 (blue) to 52 °C (red) and b) azimuthally integrated WAXS intensity *vs.* azimuthal angle ϕ during thermal cycling (temperature not color-coded).

The absence of a crystal-crystal transformation can be explained by the high time- and temperature-dependence of the PBA polymorphic mixture (Section 6). In consequence, PEU specimen preparation and a 4 day storage time at room temperature prior to WAXS measurements may have already induced the crystal-crystal transformation, such that the presence of a purely α crystal mixture prohibited further transformation. By contrast, specimen did not exhibit the expansion on initial heating after having been stored for several days at room temperature. In turn, the WAXS measurements indirectly hint at the occurrence of the polymorphic transformation. The detected PBA polymorphic mixture exhibited an increased amount of β crystallites after the thermomechanical cycle, compared with the polymorphic mixture before cycling. It is assumed, that the polymorphic mixture after withdrawing the PEU specimens from the tensile testing system was similar to the one detected after one thermal cycle. Accordingly, the difference can be ascribed to $\beta \rightarrow \alpha$ transformation taking place.

Further indication for the occurrence of crystallization processes prior to WAXS measurements, including the crystal-crystal transformation and post-crystallization phenomena is given by the intensity of the equatorial peaks during thermal cycling (Figure 8.9b). High equatorial peaks at 180 and 360° ($t = 0$) vanished, when the specimen was heated to 60 °C ($t = 0.5$) and reappeared on cooling ($t = 1$, color does not represent temperature). Pronounced differences in the magnitude of the these peaks before and directly after actuation can only be explained by changes in the polymorphic mixture and PBA post-crystallization.

In consequence, the difference between the initial and the final crystalline state as well as the expansion on initial heating may be ascribed to the PBA $\beta \rightarrow \alpha$ transformation.

8.5. Geometric Versatility

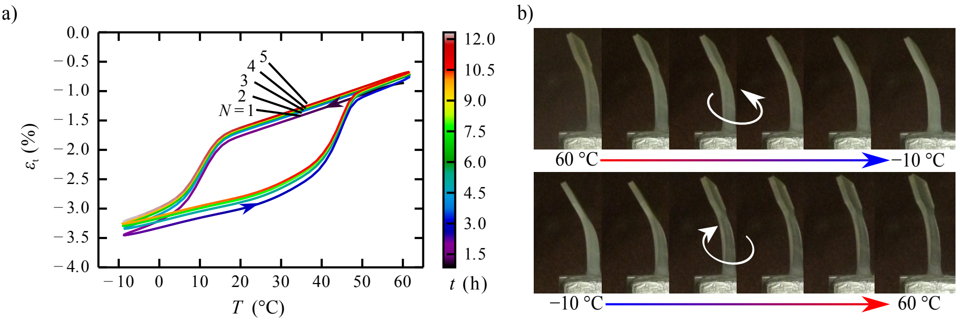

Figure 8.10.: Actuation between 60 and −10 °C after training in compression and torsion mode. a) Sample thickness as determined in dilatometric measurements after compressive deformation at 7 kN and 60 °C for five thermomechanical cycles and b) photo-series, showing actuation in torsional mode during a full thermal cycle.

Motivated by the observations after tensile training, the geometric versatility of the two-way shape changes was tested in further thermomechanical experiments. In course of compressive training, a circular sample of 6.4 mm thickness and 30 mm diameter was compressed with a force of 7000 N at 60 °C, before the compressive force was completely released. Thereafter, the relaxed sample with a thickness of 5.92 mm became flatter on cooling and thicker on heating, as quantitatively determined in dilatometric measurements (Figure 8.10a).

Substantial actuation was also realized after application of extensive shear stress in torsional training (Figure 8.10b). Five complete revolutions ($\sim$ 1800°) were manually applied and unloaded at 60 °C. Subsequently, the specimen twisted on cooling to -10 °C (top row, right and bottom row) and straightened on heating to 60 °C (middle row).

8.6. Conclusion

Trained PEU specimens conducted significant shape changes between a low- and a high-temperature shape for three different thermomechanical training scenarios. The shape changes were opposed to or in line with the direction of thermal expansion and exceeded the degree of thermal expansion by more than one order of magnitude. The high-temperature shape was predetermined by plastic deformation of the rubbery PEU specimen. In turn, the low-temperature shape was characterized by the specimen's tendency to extend in direction of the applied training.

The macroscopic shape change on cooling was ascribed to globally oriented PBA crystallization, as observed in WAXS. As a possible explanation, orientation arose from epitaxial crystal growth of PBA lamellae on deformation-induced α crystallites, which memorized the direction of training and thereby directed crystallization-induced elongation. Inversely, entropy-elastic chain recoiling of PBA soft segment chains reversed that orientation on heating. Presumably, similar mechanisms are also responsible for actuation under isotonic conditions.

The novel semicrystalline actuator was able to realize geometrically complex reversible shape changes, including increase and decrease of length and thickness as well as twisting and untwisting and is expected to have tremendous application potential.

9. Conclusions and Outlook

The aim of this thesis was to obtain improved control and enhance the shape memory properties on the one hand and to further develop the actuation behavior in semicrystalline polymer networks on the other hand. Therefore, the responses of thermomechanically pretreated SMPs to thermal stimuli were studied under various thermomechanical conditions; among them shape changes on heating in one, two or multiple steps, triggered stress recoveries as well as fully thermoreversible actuation, both under constant stress and stress-free conditions.

An initial task was to compare the shape memory properties of two SMPUs with the focus on the investigated polymer network architecture. As a main result, the shape memory properties of nanostructured, chemically cross-linked SPOSS-PU networks were superior compared to those observed in physically cross-linked PEU block copolymers. In SPOSS-PUs, most pronounced shape fixity as well as strain and stress recovery were observed at a high cross-link density. At lower cross-link density, shape recoverability slightly diminished due to stress relaxation, either resulting from viscous flow of PCL chains, from Si—O bond interchanges or from a mixture thereof. In contrast, the highest shape fixity, strain and stress recoverability of the PEUs were found at the highest PBA soft segment content / chain length. As a main cause, the shorter PBA chains were expected to transfer the greater amount of stress to the hard segment domains and thereby irreversibly deformed these, what might have reduced shape recoverability.

Moreover, the studies have shown that the programmed SPOSS-PUs can successfully fix a second deformation by cooling below the PCL glass transition temperature. The associated deformation process (cold drawing) was connected to microstructural reorganization, as apparent by necking at increased PCL chain length. Subsequently, the SPOSS-PUs exhibited triple- and multi-shape properties. Initial heating of the two-fold programmed SPOSS-PUs triggered gradual shape recovery, which could be virtually interrupted and resumed at any temperature below the PCL melting transition. Melting finally released the remaining deformation.

Regarding the ability to thermomechanically influence the shape memory behavior of PEUs, promising results were obtained by a systematic manipulation of the crystallization and storage conditions. These determined the polymorphic PBA state, composed of a kinetically preferential, metastable PBA β and a thermodynamically stable PBA α crystal form. The actual polymorphic mixture effectively defined the thermal stability of the temporary shape and influenced the strain and stress recovery profiles.

As a key finding, PEUs were able to supply reversible shape changes under isotonic conditions, when cooled below the PBA crystallization and heated above the PBA melting transition temperature. Under tensile load, the specimens repeatedly expanded and contracted without the necessity of a shape programming step, as it is obligatory for the realization of the 1W-SME. It was shown that higher PBA soft segment content in PEU and small amount of deformation-induced PBA crystallites supported pronounced crystallization in the PBA α crystal form and thereby enhanced CIE on cooling. PBA melting on heating reversed that elongation.

Considerable progress has been made with regard to bidirectional actuation under stress-free conditions. To stimulate a shape change on cooling, a ‘training’ procedure was designed, which mainly introduced deformation-induced PBA α crystallites as pre-oriented nuclei into the PEU matrix. On cooling, these nuclei stimulated oriented, epitaxial crystal growth. Temperature-resolved *in situ* WAXS measurements witnessed that oriented PBA crystallization occurred simultaneously to specimen expansion. Melting and entropy-elastic PBA chain recoiling reversed the orientation and thereby induced an opposed shape change on heating. Observed shape changes included increase and decrease of length and thickness as well as twisting and untwisting of accordingly trained PEU specimens.

Such actuation of a semicrystalline bulk polymer is a break-through in actuator technology. It supplies pronounced and geometrically complex shape changes. In future, stress-free actuation of SMPs may allow to design completely new products. Nowadays, the application of SMPs with 1W-SME gains momentum and more and more applications are designed and tested. For instance, gloves from SMPs were proposed as a potential application and a patent granted. The presentation of SPOSS-PUs with highly reliable dual- and triple-shape behavior as well as the ability to acquire thermomechanical control over a PEU with polymorphic soft segment are further steps on the way to improve the available SMP technology and gain fine-tuned control of the thermomechanical specimen responses. Until bidirectional semicrystalline actuators are employed in an equivalent extent, further challenges have to be met. For example, investigations of the nucleating process on the one hand and of the relevant mesoscopic crystalline structure on the other hand would allow to develop a better understanding of CIE. For application purposes, the highly elastic, yet soft high-temperature state may not be stiff enough for future applications. Also, new questions arise: What is the long-time stability of the individual shapes? Can the magnitude of the observed shape changes be further increased in SMPs with a higher degree of crystallinity? Can nucleating agents be introduced synthetically to achieve a well-defined high-temperature shape and tailor-made shape changes? How can the actuation cycle be thermodynamically described and what is the energy balance of expansion and contraction?

For convenience, the employment and triggering of freely actuating SMPs should be simplified. For example, Joule heating triggers electro-active SMPs. For actuation too, it is a highly desirable feature, which would allow to initiate shape changes simply by touching a switch. These aspects could account for a reliable, favorable actuator technology, suppling pronounced, geometrically complex shape changes.

A. Settings of CTMs

Table A.1.: Experimental settings of shape memory measurements. The thermomechanical procedures are given in Chapter 3, the results described in Chapter 4.

Described in chapter	4		5		6	
Testing procedure	Dual-shape		Triple-shape		Dual-shape	
Material series	SPOSS-PU		SPOSS-PU		PEU-h(ssc), -m(ssc), -l(ssc)	
Recovery mode	free strain	fixed strain	free strain	fixed strain	free strain	fixed strain
Specimen type	5B [a]	5B[a]	5B[a]	5B[a]	5B[a]	5B[a]
Clamping pressure P_c (bar)	3	3	6	6	3	3
High temperature T_{high}(°C)	70	70	70	70	60	60
Intermediate temperature T_{mid}(°C)	-	-	10/30[b]	10/30[b]	23	23
Low temperature T_{low}(°C)	10	10	−40	−40	−20	−20
Cooling rate $\dot{T}_c$ (K min^{-1})	−16.6	−16.6	−39/−62[c]	−39/−62[c]	−3.8/−4.3[d]	−3.8/−4.3[d]
Heating rate $\dot{T}_h$ (K min^{-1})	18.2	18.2	18/8.4[c]	18/8.4[c]	19.5/17.4[e]	19.5/17.4[e]
Holding time t_h (min)	5	5	5[f]	5[f]	5	5
Room temperature holding	No	No	No	No	Yes	Yes
Deformation strain ε_m, (ε_{m1}, ε_{m2}) (%)	100	100	100/200	100/200	100	100
Strain rate $\dot{\varepsilon}$ (mm min^{-1})	30	30	30	30	3	3
Unloading rate $\dot{F}_u$ (N min^{-1})	5	5	10	10	variable[g]	variable[g]

---

[a] According to EN ISO 527-2: 1996.

[b] Intermediate temperature during cooling and heating, respectively.

[c] During first or second cooling/heating, respectively.

[d] Cooling rates from 60 to −20 °C and from 60 to 23 °C, respectively.

[e] Heating rates from −20 to 23 °C and from 23 to 60 °C, respectively.

[f] Holding times of 10 min were attached after each cooling, heating or deformation step in the strain recovery process.

[g] Unloaded within exactly 1 min, using a dynamically adapted, linear stress release rate.

Table A.2.: Experimental settings of actuation measurements. The thermomechanical procedures are given in Chapter 3, the results described in Chapter 4.

Described in chapter	6	7		8		
Cycling mode	isotonic	isotonic		stress-free		
Material series	PEU-h(ssc), -m(ssc), -l(ssc)	PEU		PEU		
Deformation mode	tensile strain-controlled	tensile dual-shape	tensile triple-shape	tensile	compressive stressfree	torsional
Specimen type	5B[a]	5B[a]	5B[a]	S3A[a]	cyclindrical	S3A[a]
Clamping pressure P_c (bar)	3	3	3	6	-	-
Pretreatment						
Stress rate $\dot{\sigma}$ (MPa min^{-1})	-	+/– 0.2	+/– 0.2	-	+/– 0.7	-
Initial stress σ_i (MPa)	-	0.75 - 3.0	0.75 - 3.0	-	10	-
Initial strain ε_i (%)	100	-	-	1000	-	-
Strain rate $\dot{\varepsilon}$ (mm min^{-1})	+/– 3	-	-	+/– 12	-	-
Cyclic Testing Conditions						
Constant stress σ_c (MPa)	-	0.5 - 2.0	0.5 - 2.0	0.025	10	-
Precyclic strain ε_{pre} (%)	80	-	-	-	-	-
Deformation temperature T_D (°C)	60	60	60	60	60	60
High temperature T_{high} (°C)	60	60	70	60	60	60
Intermediate temperature T_{mid} (°C)	-	-	55 [b]	-	-	-
Low temperature T_{low} (°C)	−20	−20	−20	−10	−10	−10
Cooling rate $\dot{T}_c$ (K min^{-1})	−3.8	−36	−19/−49[c]	−3.8	−3.8	−3.8
Heating rate $\dot{T}_h$ (K min^{-1})	19.5	20	21/13[d]	19.5	19.5	19.5
Holding time t_h (min)	2[e]	2[e]	2	2[e]	2	2

---

[a] According to EN ISO 527-2: 1996 (5B) or DIN 53504 (S3A).

[b] In additional measurements, T_{mid} was set to 35 or 45 °C on cooling, while T_{mid} on heating was maintained at 55 °C.

[c] For cooling from 70 to 55 °C and 55 to −20 °C, respectively.

[d] For heating from −20 to 55 °C and 55 to 70 °C, respectively.

[e] The deformation was preceded by a temperature holding time of 5 min.

Bibliography

1. Chang, L. C. & Read, T. A. *Transactions of the American Institute of Mining and Metallurgical Engineers* **191**, 47–52 (1951).
2. Buehler, W. J., Gilfrich, J. V. & Wiley, R. C. *Journal of Applied Physics* **34**, 1475–1477 (1963).
3. de Lange, R. G. & Zijderveld, J. A. *Journal of Applied Physics* **39**, 2195–2200 (1968).
4. Otsuka, K. & Wayman, C. M. *Shape memory materials*, vol. 1 (Cambridge University Press, 1998), 1 edn.
5. Schurch, K. E. & Ashbee, K. H. G. *Nature* **266**, 706–707 (1977).
6. Lai, A., Du, Z., Gan, C. L. & Schuh, C. A. *Science (New York, N.Y.)* **341**, 1505–8 (2013).
7. Lendlein, A. & Kelch, S. *Angewandte Chemie International Edition* **41**, 2034–2057 (2002).
8. Mather, P. T., Luo, X. & Rousseau, I. A. *Annual Review of Materials Research* **39**, 445–471 (2009).
9. Huang, W. *et al. Materials Today* **13**, 54–61 (2010).
10. Pretsch, T. *Polymers* **2**, 120–158 (2010).
11. Wei, Z. G., Sandström, R. & Miyazaki, S. *Journal of Materials Science* **3**, 3743–3762 (1998).
12. Gandhi, M. & Thompson, B. *Smart materials and structures* (Springer-Verlag GmbH, 1992).
13. Huang, H. L., Suk-Ho, P. & Jong-Oh, P. In *39th International Symposium on Robotics*, 888–893 (Seoul, 2008).
14. Ruiz-del Solar, J., Chown, E. & Plöger, P. G. (eds.) *RoboCup 2010: Robot Soccer World Cup XIV*, vol. 6556 of *Lecture Notes in Computer Science* (Springer, Berlin, Heidelberg, 2011).
15. El Feninat, F., Laroche, G., Fiset, M. & Mantovani, D. *Advanced Engineering Materials* **4**, 91–104 (2002).
16. Mano, J. F. *Advanced Engineering Materials* **10**, 515–527 (2008).
17. Yakacki, C. M. & Gall, K. *Advanced Polymer Science* **226** (2010).
18. Huang, W. M. *The Open Medical Devices Journal* **2**, 11–19 (2010).
19. Katzenberg, F., Heuwers, B. & Tiller, J. C. *Advanced materials (Deerfield Beach, Fla.)* **23**, 1909–11 (2011).

20. Santo, L. *et al.* *Microgravity Science and Technology* **24**, 287–296 (2012).
21. Ji, F. L., Hu, J. L., Li, T. C. & Wong, Y. W. *Polymer* **48**, 5133–5145 (2007).
22. Kim, B. K., Lee, S. Y. & Xu, M. *Polymer* **37**, 5781–5793 (1996).
23. Tobushi, H., Hara, H., Yamada, E. & Hayashi, S. *Smart Materials and Structures* **5**, 483–491 (1996).
24. Lee, B. S., Chun, B. C., Chung, Y.-c., Sul, K. I. & Cho, J. W. *Macromolecules* **34**, 6431–6437 (2001).
25. Yang, J. H., Chun, B. C., Chung, Y.-C. & Cho, J. H. *Polymer* **44**, 3251–3258 (2003).
26. Pereira, I. M. & Oréfice, R. L. *Journal of Materials Science* **45**, 511–522 (2010).
27. Pretsch, T. *Smart Materials and Structures* **19**, art. no. 015006+ (2010).
28. Pretsch, T. *Polymer Degradation and Stability* **95**, 2515–2524 (2010).
29. Hong, S. J., Yu, W.-R. & Youk, J. H. *Smart Materials and Structures* **19**, 035022 (2010).
30. Mya, K. Y. *et al.* *Journal of Polymer Science Part A: Polymer Chemistry* **47**, 4602–4616 (2009).
31. Neumann, D., Fisher, M., Tran, L. & Matisons, J. G. *Journal of the American Chemical Society* **124**, 13998–13999 (2002).
32. Chae Jung, Y., Hwa So, H. & Whan Cho, J. *Journal of Macromolecular Science, Part B* **45**, 453–461 (2006).
33. Lee, K. M., Knight, P. T., Chung, T. & Mather, P. T. *Macromolecules* **41**, 4730–4738 (2008).
34. Knight, P. T., Lee, K. M., Chung, T. & Mather, P. T. *Macromolecules* **42**, 6596–6605 (2009).
35. Hadjichristidis, N. *Journal of Polymer Science Part A: Polymer Chemistry* **37**, 857–871 (1999).
36. Xu, J. & Song, J. *Proceedings of the National Academy of Sciences* **107**, 7652–7657 (2010).
37. Huang, Y., Xu, X., Luo, X. & Ma, D. *Chinese Journal of Polymer Science* **20**, 45–51 (2002).
38. Chung, T., Romo-Uribe, A. & Mather, P. T. *Macromolecules* **41**, 184–192 (2008).
39. Zotzmann, J., Behl, M., Hofmann, D. & Lendlein, A. *Advanced Materials* **22**, 3424–3429 (2010).
40. Behl, M., Zotzmann, J. & Lendlein, A. *International Journal of Artificial Organs* **34**, 231–237 (2011).
41. Anthony, R. L., Caston, R. H. & Guth, E. *Journal of Physical Chemistry* **46**, 826–840 (1942).
42. Treloar, L. R. G. *The Physics of Rubber Elasticity* (Oxford University Press, Oxford, 1975), 3rd edn.
43. Chen, S., Hu, J., Zhuo, H. & Zhu, Y. *Materials Letters* **62**, 4088–4090 (2008).

44. Chen, S., Hu, J. & Zhuo, H. *Composites Science and Technology* **70**, 1437–1443 (2010).
45. Westbrook, K. K. *et al. Smart Materials and Structures* **20**, 065010 (2011).
46. Gough, J. *Memoirs of the Literary and Philosophical Society of Manchester* **1**, 288–295 (1805).
47. Hosler, D., Burkett, S. L. & Tarkanian, M. J. *Science* **284**, 1988–1991 (1999).
48. Goodyear, C. (1844). *Improvement in India-Rubber Fabrics*, US3633.
49. Joule, J. P. *Philosophical Transactions of the Royal Society of London* **149**, 91–131 (1859).
50. Guth, E. & Mark, H. *Monatshefte für Chemie* **65**, 93–121 (1934).
51. Kuhn, W. *Kolloid-Zeitschrift* **68**, 2–15 (1934).
52. Flory, P. J. *The Journal of Chemical Physics* **17**, 223 (1949).
53. Flory, P. J. *Principles of Polymer Chemistry* (Cornell University Press, New York, 1953).
54. Clark, J. F. & Preston, J. M. *Journal of the Textile Institute Transactions* **44**, T596–T608 (1953).
55. Vernon, L. B. & Vernon, H. M. (1941).
56. Liu, C., Qin, H. & Mather, P. T. *Journal of Materials Chemistry* **17**, 1543 (2007).
57. Dole, M. *Journal of Macromolecular Science: Part A - Chemistry* **15**, 1403–1409 (1981).
58. Kauffman, G. & Mayo, I. *The Chemical Educator* **2**, 1–21 (1996).
59. Fukuhara, M., Inoue, A. & Nishiyama, N. *Applied Physics Letters* **89**, 101903+ (2006).
60. Rousseau, I. A. *Polymer Engineering and Science* **48**, 2075–2089 (2008).
61. Chen, S., Hu, J., Liu, Y., Liem, H. & Zhu, Y. *Journal of Polymer Science: Part B: Polymer Physics* **45**, 444–454 (2007).
62. Messori, M. *et al. Journal of Materials Science* **48**, 424–440 (2012).
63. Pandini, S. *et al. Polymer* **53**, 1915–1924 (2012).
64. Yakacki, C., Satarkar, N., Gall, K., Likos, R. & Hilt, Z. *J. Appl. Polym. Sci.* **112**, 3166–3176 (2009).
65. Lu, H., Liu, Y., Gou, J., Leng, J. & Du, S. *Applied Physics Letters* **96**, 084102 (2010).
66. Xu, B. *et al. Journal of Materials Chemistry* **20**, 3442 (2010).
67. Kontou, E., Spathis, G., Niaounakis, M. & Kefalas, V. *Colloid & Polymer Science* **268**, 636–644 (1990).
68. Sperling, L. H. *Introduction to Physical Polymer Science* (John Wiley & Sons, Inc., Hoboken, New Jersey, 2006), 4th edn.
69. Alteheld, A., Feng, Y., Kelch, S. & Lendlein, A. *Angewandte Chemie (International ed. in English)* **44**, 1188–92 (2005).
70. Du, H. & Zhang, J. *Colloid and Polymer Science* **288**, 15–24 (2009).
71. Liu, C. *et al. Macromolecules* **35**, 9868–9874 (2002).
72. Petrovic, Z. S. & Ferguson, J. *Progress in polymer science* **16**, 695–836 (1991).

73. Meckel, W., Goyert, W. & Wieder, W. In Holden, G., Legge, N. R., Quirk, R. & Schroeder, H. E. (eds.) *Thermoplastic Elastomers*, chap. 1, 1–619 (Hanser Publishers, 1996), 2nd edn.
74. Lange, R. F. M., Van Gurp, M. & Meijer, E. W. *Journal of Polymer Science Part A: Polymer Chemistry* **37**, 3657–3670 (1999).
75. Hyer, M. W. *Stress Analysis of Fiber-reinforced Composite Materials* (DEStech Publications, Inc, 2009).
76. Aithal, U. S., Aminabhavi, T. M., Shukla, S. S. & Balundgi, R. H. *Journal of Macromolecular Science, Part C: Polymer Reviews* **30**, 43–105 (1990).
77. van der Mee, M. *Thermoreversible Cross-linking of Elastomers.* Ph.D. thesis, Eindhoven University of Technology (2007).
78. Stokes, K., McVenes, R. & Anderson, J. M. *J Biomater Appl* **9**, 321–354 (1995).
79. Chen, S. *et al.* *Journal of Applied Polymer Science* **102**, 5224–5231 (2006).
80. Qi, H. & Boyce, M. *Mechanics of Materials* **37**, 817–839 (2005).
81. Lee, B. S., Chun, B. C., Chung, Y.-C., Sul, K. I. & Cho, J. W. *Macromolecules* **34**, 6431–6437 (2001).
82. Ni, X. & Sun, X. *Journal of Applied Polymer Science* **100**, 879–885 (2006).
83. Pretsch, T. & Müller, W. *Polymer Degradation and Stability* **95**, 880–888 (2010).
84. Mishra, M. & Kobayashi, S. *Star and Hyperbranched Polymers* (CRC Press, 1999).
85. Laine, R. M. *Journal of Materials Chemistry* **15**, 3725 (2005).
86. Waddon, A. J. & Coughlin, E. B. *Chemistry of Materials* **15**, 4555–4561 (2003).
87. Lim, S.-K., Hong, E.-P., Choi, H. J. & Chin, I.-J. *Journal of Industrial and Engineering Chemistry* **16**, 189–192 (2010).
88. Zheng, L., Waddon, A. J., Farris, R. J. & Coughlin, E. B. *Macromolecules* **35**, 2375–2379 (2002).
89. Fu, B. X. *et al.* *Polymer* **42**, 599–611 (2001).
90. Jang, M. K., Hartwig, A. & Kim, B. K. *Journal of Materials Chemistry* **19**, 1166 (2009).
91. Knight, P., Lee, K., Qin, H. & Mather, P. *Biomacromolecules* **9**, 2458–2467 (2008).
92. Huang, W. M. *et al.* *Journal of Polymer Research* **19**, 9952 (2012).
93. Mandelkern, L. *Crystallization of polymers, Volume 1: Equilibrium Concepts*, vol. 1 (Cambridge University Press, Cambridge, 2002), 2nd edn.
94. Becker, G. W., Braun, D. & Carlowitz, B. *Die Kunststoffe: Chemie, Physik, Technologie* (Hanser, 1990).
95. Fox, T. G. & Flory, P. J. *Journal of Applied Physics* **21**, 581–591 (1950).
96. Pan, P. & Inoue, Y. *Progress in Polymer Science* **34**, 605–640 (2009).
97. Strobl, G. *The European Physical Journal E* **183**, 165–183 (2000).
98. Zhao, L., Wang, X., Li, L. & Gan, Z. *Polymer* **48**, 6152–6161 (2007).

99. Dukovski, I. & Muthukumar, M. *The Journal of Chemical Physics* **118**, 6648 (2003).
100. Ward, I. M. *Mechanical properties of solid polymers* (Wiley-Interscience, London, 1971), 1 edn.
101. Puett, D., Smith Jr., K. J. & Ciferri, A. *The Journal of Physical Chemistry* **69**, 141–150 (1965).
102. Grellmann, W. & Seidler, S. *Polymer Testing* (Carl Hanser Verlag, München, 2007).
103. Schreuer, E. *Kolloid-Zeitschrift* **124**, 176–181 (1951).
104. Meyer, K. H. & Ferri, C. *Helvetica Chimica Acta* **18**, 570–589 (1935).
105. Wagermaier, W., Kratz, K., Heuchel, M. & Lendlein, A. In *Shape-Memory Polymers*, 97–146 (Springer-Verlag, 2009).
106. Ehrenstein, G. W., Riedel, G. & Trawiel, P. *Praxis der thermischen Analyse von Kunststoffen* (Hanser Fachbuch, 2003).
107. Elsabee, M. & Prankerd, R. *International Journal of Pharmaceutics* **86**, 211–219 (1992).
108. Menard, K. P. *Dynamic Mechanical Analysis: A Practical Introduction* (CRC Press, 1999).
109. Leng, J., Lan, X., Liu, Y. & Du, S. *Progress in Materials Science* **56**, 1077–1135 (2011).
110. Gall, K. *et al.* *Journal of Biomedical Materials Research Part A* **73**, 339–348 (2005).
111. Sauter, T., Heuchel, M., Kratz, K. & Lendlein, A. *Polymer Reviews* **53**, 6–40 (2013).
112. Ratna, D. & Karger-Kocsis, J. *Journal of Materials Science* **43**, 254–269 (2008).
113. Pretsch, T., Jakob, I. & Müller, W. *Polymer Degradation and Stability* **94**, 61–73 (2009).
114. Massa, W. *Kristallstrukturbestimmung* (Teubner, 2002).
115. Wilchinsky, Z. W. *Journal of Polymer Science Part A-2: Polymer Physics* **6**, 281–288 (1968).
116. Xie, T. *Nature* **464**, 267–270 (2010).
117. Lendlein, A., Jiang, H., Jünger, O. & Langer, R. *Nature* **434**, 879–882 (2005).
118. Ware, T., Hearon, K. & Lonnecker, A. *Macromolecules* **45**, 1062–1069 (2012).
119. Zotzmann, J., Behl, M., Feng, Y. & Lendlein, A. *Advanced Functional Materials* **20**, 3583–3594 (2010).
120. Mohr, R. *et al.* *Proceedings of the National Academy of Sciences of the United States of America* **103**, 3540–3545 (2006).
121. Müller, W. W. & Pretsch, T. *European Polymer Journal* **46**, 1745–1758 (2010).
122. Miaudet, P. *et al.* *Science* **318**, 1294–6 (2007).
123. Leng, J.-s. & Yoon, S.-h. *International Journal of Modern Physics* **23**, 1248–1253 (2009).
124. Meng, Q., Hu, J. & Yeung, L. *Smart Materials and Structures* **16**, 830–836 (2007).
125. Schmidt, A. M. *Macromolecular Rapid Communications* **27**, 1168–1172 (2006).
126. Kumar, U. N., Kratz, K., Wagermaier, W., Behl, M. & Lendlein, a. *Journal of Materials Chemistry* **20**, 3404 (2010).

127. Leng, J., Zhang, D., Liu, Y., Yu, K. & Lan, X. *Applied Physics Letters* **96**, 111905 (2010).
128. Zhang, D., Liu, Y. & Leng, J. In Tomizuka, M. (ed.) *The 15th International Symposium on: Smart Structures and Materials & Nondestructive Evaluation and Health Monitoring*, 693213–693213–8 (2008).
129. Li, G., Fei, G., Xia, H., Han, J. & Zhao, Y. *Journal of Materials Chemistry* **22**, 7692 (2012).
130. Lv, H., Liu, Y., Leng, J. & Du, S. *Advanced Materials Research* **47-50**, 258–261 (2008).
131. Feil, H., Bae, Y., Feijen, J. & Kim, S. *Macromolecules* **25**, 5528–5530 (1992).
132. Han, X.-J. *et al.* *Macromolecular Rapid Communications* **33**, 1055–1060 (2012).
133. Kalita, H., Mandal, M. & Karak, N. *Journal of Polymer Research* **19**, 9982 (2012).
134. Kumpfer, J. R. & Rowan, S. J. *Journal of the American Chemical Society* **133**, 12866–12874 (2011).
135. Jiang, H. Y., Kelch, S. & Lendlein, A. *Advanced Materials* **18**, 1471–1475 (2006).
136. Kolesov, I. S. & Radusch, H.-J. *Express Polymer Letters* **2**, 461–473 (2008).
137. Li, J. *et al.* *Journal of Materials Chemistry* **21**, 12213 (2011).
138. Bellin, I., Kelch, S., Langer, R. & Lendlein, A. *Proceedings of the National Academy of Sciences of the United States of America* **103**, 18043–18047 (2006).
139. Behl, M., Bellin, I., Kelch, S., Wagermaier, W. & Lendlein, A. *Advanced Functional Materials* **19**, 102–108 (2009).
140. Xie, T., Xiao, X. & Cheng, Y.-T. *Macromolecular Rapid Communications* **30**, 1823–1827 (2009).
141. Bae, C. Y., Park, J. H., Kim, E. Y., Kang, Y. S. & Kim, B. K. *Journal of Materials Chemistry* **21**, 11288 (2011).
142. Li, J., Rodgers, W. & Xie, T. *Polymer* **52**, 5320–5325 (2011).
143. Tobushi, H., Hayashi, S., Sugimoto, Y. & Date, K. *Materials* **2**, 1180–1192 (2009).
144. Sun, L. *et al.* *Materials and Design* **33**, 577–640 (2012).
145. Atkins, J. H. & Owensby, J. E. (1984).
146. Yakacki, C. M. *et al.* *Biomaterials* **28**, 2255–2263 (2007).
147. Metzger, M. F., Wilson, T. S., Schumann, D., Matthews, D. L. & Maitland, D. J. *Biomedical Microdevices* **4**, 89–96 (2002).
148. Small, W., Singhal, P., Wilson, S. & Maitland, D. J. *Journal of Materials Chemistry* **20**, 3356–3366 (2010).
149. Tseng, L.-F., Mather, P. T. & Henderson, J. H. In *Bioengineering Conference (NEBEC), 2012 38th Annual Northeast*, 227–228 (Philadelphia, 2012).
150. Pretsch, T., Ecker, M., Schildhauer, M. & Maskos, M. *Journal of Materials Chemistry* **22**, 7757 (2012).
151. Ecker, M. & Pretsch, T. *Smart Materials and Structures* **22**, 094005 (2013).

152. Ecker, M. & Pretsch, T. *RSC Advances* **4**, 286 (2014).
153. Sokolowski, W. M. & Tan, S. C. *Journal of Spacecraft and Rockets* **44**, 750–754 (2007).
154. Ishizawa, J. In *Proceeding of the 7th International Symposium on Artificial Intelligence, Robotics and Automation in Space*, 1–4 (2003).
155. Yang, P., Liu, L., Liu, Y. & Leng, J. In *The 9th International Conference on Fracture & Strengh of Solids (FEOFS)*, 2, 1–9 (2013).
156. Florance, J. P. *et al.* In *AIAA Structures, Structural Dynamics, and Materials Conference*, art. no. 1961 (2003).
157. Thill, C., Etches, J., Bond, I., Potter, K. & Weaver, P. *Royal Aeronautical Society* **112**, art. no 3216 (2008).
158. Chu, W.-S. *et al.* *International Journal of Precision Engineering and Manufacturing* **13**, 1281–1292 (2012).
159. Hamilton, B. K., Ahmed, H., Birchette, T. S. & Murrill, R. R. US7798443 B2, (2010).
160. Xi, F., Finistauri, A. D. & Moosavian, A. WO2013192483 A1, (2013).
161. Kota, S., Hetrick, J. & Osborn, R. *Proc. SPIE* **5054**, 24–33 (2003).
162. Sanderson, T. & Gall, K. *Raytheon Technology Today* **1**, 10 (2007).
163. Finkbeiner, J., Ahmad, J., Santosa, W., Xu, G. Y. & (Jizhong) Xiao, J. In *2011 6th IEEE Conference on Industrial Electronics and Applications*, 2139–2144 (IEEE, 2011).
164. Villanueva, A., Smith, C. & Priya, S. *Bioinspiration & biomimetics* **6**, 036004 (2011).
165. Tadesse, Y., Hong, D. & Priya, S. *Journal of Mechanisms and Robotics* **3**, 011008+ (2011).
166. Yang, K. & Gu, C. L. *Proceedings of the Institution of Mechanical Engineers, Part C: Journal of Mechanical Engineering Science* **221**, 1131–1140 (2007).
167. Ho, T. & Lee, S. *International Journal of Control, Automation and Systems* **11**, 991–1000 (2013).
168. Zhang, C. & Laine, R. M. *Journal of the American Chemical Society* **122**, 6979–6988 (2000).
169. Müller, F., Bräuer, W., Ott, K.-H. & Hoppe, H.-G., EP 0 571 830 81 (1993).
170. Hättig, J. & Winkler, J. *PU magazin* **4**, 1–16 (2008).
171. Pintos, M., Bravo, R., Baluja, M. C., Inmaculada Paz Andrade, Maria Roux-Desgranges, G. & Grolier, J.-P. E. *Canadian journal of Chemistry* **66**, 1179–1186 (1988).
172. Orwoll, R. A. & Arnold, P. A. In *Physical Properties of Polymers Handbook*, 233–257 (AIP Press, New York, 1996).
173. Paris, O. *et al.* *Journal of Applied Crystallography* **40**, 466–470 (2006).
174. Hammersley, A. P., Svensson, S. O., Hanfland, M., Fitch, A. N. & Häusermann, D. *High Pressure Research* **14**, 235–248 (1996).
175. Liu, Y., Yang, X., Zhang, W. & Zheng, S. *Polymer* **47**, 6814–6825 (2006).
176. Núñez, E. *et al.* *Polymer* **45**, 5251–5263 (2004).

177. Mya, K. Y., Gose, H. B., Pretsch, T., Bothe, M. & He, C. *Journal of Materials Chemistry* **21**, 48274836 (2011).
178. Day, M., Cooney, J., Shaw, K. & Watts, J. *Journal of Thermal Analysis and Calorimetry* **52**, 261–274 (1998).
179. Wang, Y., Rodriguez-Perez, M. A., Reis, R. L. & Mano, J. a. F. *Macromolecular Materials and Engineering* **290**, 792–801 (2005).
180. Lendlein, A. *Shape-Memory Polymers* (Springer-Verlag Berlin and Heidelberg GmbH & Co. K, 2012), 2010 edn.
181. Vouros, P. & Harvey, D. J. *Biological Mass Spectrometry* **7**, 217–225 (1980).
182. Sperling, L. H., Cooper, S. L. & Tobolsky, A. V. *Journal of Applied Polymer Science* **10**, 1725–1735 (1966).
183. Yang, J. H., Chun, B. C., Chung, Y.-C. & Cho, J. H. *Polymer* **44**, 3251–3258 (2003).
184. Gent, A. & Madan, S. *Journal of Polymer Science Part B: Polymer Physics* **27**, 1529–1542 (1989).
185. Liang, J.-Z., Duan, D.-R., Tang, C.-Y., Tsui, C.-P. & Chen, D.-Z. *Polymer Testing* (2013).
186. Jäckel, K. *Kolloid-Zeitschrift* **137**, 130–162 (1954).
187. Haraguchi, K., Ebato, M. & Takehisa, T. *Advanced Materials* **18**, 2250–2254 (2006).
188. Fujita, K., Kyu, T. & St. John Manley, R. *Macromolecules* **29**, 91–96 (1996).
189. Hojabri, L., Jose, J., Leao, A., Bouzidi, L. & Narine, S. *Polymer* **53**, 3762–3771 (2012).
190. O'Driscoll, K. & Sanayei, A. *Macromolecules* **24**, 4479–4480 (1991).
191. Gan, Z., Kuwabara, K., Abe, H., Iwata, T. & Doi, Y. *Biomacromolecules* **5**, 371–378 (2004).
192. Gan, Z. & Abe, H. *Macromolecular Chemistry and Physics* **202**, 2369–2374 (2002).
193. Kai, W., Zhu, B., He, Y. & Inoue, Y. *Journal of Polymer Science Part B: Polymer Physics* **43**, 2340–2351 (2005).
194. Wu, M. C. & Woo, E. M. *Polymer International* **54**, 1681–1688 (2005).
195. Minke, R. & Blackwell, J. *Journal of Macromolecular Science, Part B* **16**, 407–417 (1979).
196. Noguchi, K., Kondo, H., Ichikawa, Y., Okuyama, K. & Washiyama, J. *Polymer* **46**, 10823–10830 (2005).
197. Hwang, K., Wu, G., Lin, S. B. & Cooper, S. L. *Journal of Polymer Science* **22**, 1677–1697 (1984).
198. Koerner, H., Kelley, J. J. & Vaia, R. A. *Macromolecules* **41**, 4709–4716 (2008).
199. Estes, G., Seymour, R. & Cooper, S. *Macromolecules* **4**, 452–457 (1971).
200. Reynolds, N., Spiess, H. W., Hayen, H., Nefzger, H. & Eisenbach, C. D. *Macromolecular Chemistry and Physics* **195**, 2855–2873 (1994).
201. Prisacariu, C. & Scortanu, E. *High Performance Polymers* **20**, 117–125 (2008).
202. Flory, P. J. *The Journal of Chemical Physics* **15**, 397–408 (1947).

203. Woo, E. M. & Wu, M. C. *Journal of Polymer Science Part B: Polymer Physics* **43**, 1662–1672 (2005).
204. Jiang, X. *et al.* *Journal of Polymer Science Part B: Polymer Physics* **51**, 907–914 (2013).
205. Liu, T., Lieberwirth, I. & Petermann, J. *Macromolecular Chemistry and Physics* **202**, 2921–2925 (2001).
206. Behl, M., Kratz, K., Zotzmann, J., Nöchel, U. & Lendlein, A. *Advanced Materials* **25**, 4466–4469 (2013).
207. Behl, M., Kratz, K., Noechel, U., Sauter, T. & Lendlein, A. *Proceedings of the National Academy of Sciences of the United States of America* **110**, 12555–12559 (2013).
208. Zhou, J. *et al.* *Macromolecules* 140225110618006 (2014).
209. Warner, M. & Terentjev, E. M. *Liquid Crystal Elastomers.* March (Oxford University Press, 2003).
210. Judge, J. T. & Stein, R. S. *Journal of Applied Physics* **32**, 2357 (1961).
211. Zhao, Y., Keroack, D. & Prud'homme, R. *Macromolecules* **32**, 1218–1225 (1999).
212. Einstein, A. *Annalen der Physik* **324**, 289–306 (1906).
213. Hornbogen, E. *Progress in Colloid and Polymer Science* **64**, 125–131 (1977).

List of Publications

1. **Martin Bothe** and Thorsten Pretsch. Adaptive Handschuhe aus Formgedächtnispolymer und Verfahren der Programmierung, Patent DE 10 2011 000 679. 2011.
2. Khine Yi Mya, Halima Binte Gose, Thorsten Pretsch, **Martin Bothe**, and Chaobin He. Star-shaped POSS-polycaprolactone polyurethanes and their shape memory performance. *Journal of Materials Chemistry*, 21(13):48274836, 2011.
3. **Martin Bothe**, Khine Yi Mya, Esther Marie Jie Lin, Chee Chuan Yeo, Xuehong Lu, Chaobin He, and Thorsten Pretsch. Triple-shape properties of star-shaped POSS-polycaprolactone polyurethane networks. *Soft Matter*, 8(4):965–972, 2012.
4. **Martin Bothe**, Franziska Emmerling, and Thorsten Pretsch. Poly(ester urethane) with varying polyester chain length: Polymorphism and shape memory behavior. *Macromolecular Chemistry and Physics*, 214(23):2683-2693, September 2013.
5. **Martin Bothe** and Thorsten Pretsch. Two-Way Shape Changes of a Shape-Memory Poly(ester urethane). *Macromolecular Chemistry and Physics*, 213(22):2378–2385, November 2012.
6. **Martin Bothe** and Thorsten Pretsch. Bidirectional actuation of a thermoplastic polyurethane elastomer. *Journal of Materials Chemistry A*, 1(46):14491–14497, October 2013.

Manuscript in Preparation

Martin Bothe and Thorsten Pretsch. Poly(ester urethane) with Varying Polyester Chain Length: Polymorphism and Actuation Behavior.